Guide to Notes:

<u>Abbreviations for References:</u>

IntroGG : Introduction to GAMIT/GLOBK
GAMIT : GAMIT Reference Manual
GLOBK : GLOBK Reference Manual
  All available at http://www-gpsg.mit.edu/~simon/gtgk/docs.htm

Overview: Multi-step and distributed processing using quasi-observations

GAMIT (each network each day)
Primary observations = phase
Estimated parameters = station coordinates; zenith delays, gradients,
    ambiguities, EOP, orbital parameters
Output = h-file of parameter estimates and covariances—loosely constrained

GLOBK (combination of networks and days)
Quasi-observations = multiple h-files of coordinates, EOP
orbital parameters (or SINEX without orbital parameters)
Estimated parameters = coordinates and velocities, daily or multiday orbits
Constraints = finite or generalized
Output = time series   *or*
    combined h-file; tables of positions and/or velocities for plotting

References: *IntroGG*, Chapter 1; *GLOBK*, Chapter 1
            Dong et al. [*J. Geod. 72*. 200–214, 1998]

Automatic processing with sh_gamit and sh_glred

    Setup

        Make experiment directory; sh_setup; copy RINEX files

    Commands

        sh_gamit –s 1998 151 154 –expt emed –orbit IGSF -pres

        sh_glred –s 1998 151 1998 154 –expt emed –ncomb 1 –opt H G E

    Data files to be accessible

        raw and/or RINEX

        local or ftp access to orbits (sp3 or g-files), nav message, and EOP

        reasonable starting coordinates (apr, l-file, or sh_rx2apr from RINEX)

        rcvr/antenna info (station.info or RINEX header)

    Control files to be edited

        process.defaults: computer environment, source of files, session definition

        sites.defaults   : global RINEX to get

        sestbl.   : how to process (e.g. iterations, weighting, tropo)

        sittbl.   : coordinate constraints, antenna phase-center model, etc.

        station.info   : rcvr/ant/firmware, HI (optional if RINEX header correct)

    Processing outputs

        tabular summary of station statistics (autcln.post.sum)

        sky plots of phase residuals for each station (Figure 1)

        loosely constrained solution for each day (h-file)

        time series of station coordinates

    Reference: *IntroGG*

Directory Structure

gg → /my_gamit-globk

      /gamit   /kf   /bin   /tables /templates

/emed98 (e.g.)

    /tables   (create from gg/tables using sh_setup)

    /rinex   (observation files)

    /brdc   (navigation files)

    /igs   (sp3 orbit files)

    /gfiles

    /151   (day directories)

    /152

    …

    /gifs   (gif format of sky plots)

    /gsoln   (sh_glred or GLOBK runs)

Evaluating results

E-mail summary from sh_gamit
> Number of stations
> Worst/best rms of phase residuals
> SOLVE postfit normalized RMS ~0.2
> Large adjustments to station coordinates
> Any FATAL messages

```
Input options -expt pcnw -d 1998 243 245 246 -orbit IGSF -pres Y -copt o q mkx -dopt D ao b c g
i j k m p ps t x y -sessinfo 30 720 18 00

Processing 1998 245 GPS week 0973 3 Raw 8

/data53/rwk/oregon/pnw98/245
Disk Usage:  73094.6  Free  33857.8 Mbyte. Used 69%

Number of stations used 41 Total xfiles 41
Postfit RMS rms, to and by satellite
RMS  IT Site   All  01  02  03  04  05  06  07  08  09  10  13  14  15 . . .
RMS  26 ALL    6.8   6   0   6  11   0   0   7   8  10   0   0   7   6 . . .
 Best and Worst two sites:
RMS  26 NEWP   0.0   0   0   0   0   0   0   0   0   0   0   0   0   0 . . .
RMS  26 BROT   4.5   4   0   5   0   0   0   0   4   6   0   0   5   4 . . .
RMS  26 WHD1   9.9   8   0   8  17   0   0   0  11  13   0   0   9  10 . . .
RMS  26 CMBB  10.5  10   0   9   0   0   0   0  13  14   0   0  10   8 . . .

Double difference statistics
 Prefit nrms:  0.12403E+03    Postfit nrms: 0.17807E+00
 Prefit nrms:  0.12341E+03    Postfit nrms: 0.19016E+00
 Prefit nrms:  0.12380E+03    Postfit nrms: 0.17585E+00
 Prefit nrms:  0.12341E+03    Postfit nrms: 0.18155E+00
 Number of double differences:  36659

List of sites updated in the tables lfile from adjustments in the Prefit Solution
SKYO RADIUS     -0.4635

List of sites without Prefit coordinate solutions:
NEWP

List of sites without Postfit coordinate solutions:
NEWP
```

Detailed evaluation
> WARNING messages
> AUTCLN summary file: RMS, data amounts, bias flags [*GAMIT 4.2*]
> Adjustments to station coordinates, atmospheric parameters
> Ambiguity resolution [*GAMIT 3.4*]
> Repeatability plots: scatter, uncertainties

Process.defaults

```
#  Do not remove any of these entries.
#To by-pass a function, set the value to null: ""

## LOCAL DIRECTORIES
# Directory for translation of raw data
 set rawpth = "$procdir/raw"
# Directory path for raw archives (search all levels); e.g. /data18/simon
 set rawfnd = ""
# Input files for RINEX translators
 set mpth = "$procdir/mkrinex"
# RINEX files directory
 set rpth = "$procdir/rinex"
# Dir path for RINEX archives (search all levels); e.g. /data18/simon
 set rnxfnd = ""
# Broadcast orbit directory
 set bpth = "$procdir/brdc"
# IGS files directory
 set ipth = "$procdir/igs"
# G-files directory
 set gpth = "$procdir/gfiles"
# GAMIT and GLOBK tables directory
 set tpth = "$procdir/tables"
# Output gifs directory
 set gifpth = "$procdir/gifs"
# Globk solution directory
 set glbpth = "$procdir/gsoln"
# Globk binary h-file directory
 set glfpth = "$procdir/glbf"
# Dir path for other h-files (search all levels); e.g. /raid1/tah/SIO_GLL
 set hfnd = ""
# Template files
 set templatepth = "$procdir/templates"
# Place to store temporary control files
 set cpth = "$procdir/control"
# Archive root directory (cannot be null)
 set archivepth = "$procdir/archive"

## FTP INFO FOR REMOTE FILES
# Raw data archive
# set rawarchive = 'chandler.mit.edu'
# set rawdir = 'pub/continuous/mitnet'
# set rawlogin = "anonymous simon@chandler.mit.edu"
# Addresses for CDDSI, SOPAC, IGSCB, UNAVCO, BKG, IGN, USNO are
#    given in template/ftp_info

##GAMIT
# Set sampling interval, number of epochs, and start time for processing
 set sint = '30'
 set nepc = '2880'
 set stime = '0 0'
# Variables for updating tables
 set stinf_unique = "-u"
 set stinf_nosort = "-nosort"
 set stinf_slthgt = "2.00"
# Set "Y" to use RINEX header coordinates not in lfile or apr file
 set use_rxc      = "N"
# Broadcast orbits
 set brdc = 'brdc'
# Minimum x-file size to be used (Default 300 blocks)
 set minxf = '300'
# Set search window for RINEX files which might contain data for day
#    --default checkthe previous day
 set rx_doy_plus = 0
 set rx_doy_minus = 1
# Default globk .apr file
 set aprf = itrf00.apr
# Set compress (copts), delete (dopts) and archive (aopts) options.
# Possible d-, c-, and a- opts:
```

```
# all D, H, ao, ac, as, b, c, d, e, g, h, i, j, k, l, m, o, p, q, t, x, ps
 set dopts = ( c )
 set copts = ( x k ao )
 set aopts = ''
# Set the ftp archives (defined in ftp_info) to search for data.
# (Default archives searched are: sopac, cddis and unavco).
set rinex_ftpsites = (sopac cddis unavco)


## RESOURCES
# Minimum raw disk space in Kbytes
 set minraw = '30000'
# Minimum rinex disk space in Kbytes
 set minrinex = '30000'
# Minimum archive disk space in Kbytes
 set minarchive = '20000'
# Minimum working disk space in Kbytes
 set minwork = '200000'

## SYSTEM-DEPENDENT SETTINGS
# UNIX df command must be set to return the correct form
# Most machines
 set udf = 'df -k'
# HP
# set udf = 'bdf'
# UNIX mail command
#  Most machines
 set umail = 'mail -s'
#  HP
# set umail = 'mailx -s'
# Ghostscript path
set gspath = '/usr/bin'
# ImageMagick path fir gif conversion
# set impath = '/usr/bin/X11'
set impath = '/usr/bin'
## Web interface .html file.
 set htmlinfo = 'mitnet.html'

## USER ADDRESSES
# Mail address for report (if '' will default to `whoami` in sh_gamit)
 set mailto = 'rwk'
# Host name for email and anonymous ftp password use
#   (if '' will default to `hostname` in sh_gamit)
 set machine = ''
```

Sites.defaults

```
# File to control the use of stations in the processing
#
# Format: site expt keyword1 keyword2 ....
#
#  where the first token is site name (GAMIT uses only 4 characters,
#    GLOBK 4 or 8),
#  the second token is the 4-char experiment name, and the remaining
#  tokens, read free-format, indicate how the site is to be used
#  All sites for which there are RINEX files in the local directory will
#  be used automatically and do not need to be listed.
#
# GAMIT:
#  ftprnx = sites to ftp from rinex data archives.
#  ftpraw = sites to ftp from raw data archives.
#  localrx = site names used to search for rinex files on local system.
#            (required in conjunction with rnxfnd path variable set in
#                process.defaults).
#  xstinfo = sites to exclude from automatic station.info updating.
#  xsite  = sites to exclude from processing, all or specified days
# GLOBK:
#  glrepu = sites used in the GLRED repeatabilities (default is use all)
#  glreps = sites used for reference frame definition (stabilization) in
#           GLORG for GLRED repeatability solution (default is IGS list)
#  glts   = sites to plot as time series (default is all)
#
# may use the following
# all_sites tubi xstinfo
# individual station commands will override all_sites if they follow it
  mate_gps  tubi ftprnx xstinfo glrepu glreps
  ankr_gps  tubi ftprnx xstinfo glrepu glreps glts
  kit3_gps  tubi ftprnx xstinfo glrepu glreps
  nssp_gps  tubi ftprnx xstinfo glrepu glreps
  graz_gps  tubi ftprnx xstinfo glrepu glreps
  noto_gps  tubi ftprnx xstinfo glrepu glreps
  nico_gps  tubi ftprnx xstinfo glrepu
  sofi_gps  tubi ftprnx xstinfo glrepu
  zeck_gps  tubi ftprnx xstinfo glrepu
  zwen_gps  tubi ftprnx xstinfo glrepu glreps
  bahr_gps  tubi ftprnx xstinfo glrepu
  tela_gps  tubi ftprnx xstinfo glrepu
  tubi_gps  tubi ftpraw xstinfo glrepu        glts
  mert_gps  tubi ftpraw         glrepu        glts
  kant_gps  tubi ftpraw         glrepu        glts
  ttth_gps  tubi xstinfo xsite:1999_256-1999_278
  thht_gps  tubi xstinfo xsite glreps
```

Sestbl.

Processing Agency = MIT

Satellite Constraint = Y   ; Y/N (next 2 lines free-format but 'all' must be present)
    all   a   e   i   n   w   M rad1 rad2 rad3 rad4 rad5 rad6 rad7 rad8 rad9;
         .01 .01 .01 .01 .01 .01 .001 .001 .001 .001 .001 .001 .001 .001 .001

Choice of Experiment = RELAX.   ; BASELINE/RELAX./ORBIT
Type of Analysis = 1-ITER   ; 1-ITER/0-ITER (no postfit autcln)/PREFIT
  This now redundant AUTCLN Postfit = R ; Postfit autcln (Y or R for repeat)
Choice of Observable = LC_AUTCLN ; L1_SINGLE/L1&L2/L1_ONLY/L2_ONLY/LC_ONLY/
                                 ; L1,L2_INDEPEND./LC_HELP/LC_AUTCLN
Quick-pre observable = LC_ONLY   ; For 1st solution (default same as final

Station Error = ELEVATION 10 5   ; 1-way L1, a**2 + (b**2)(L**2) in mm, ppm
Use N-file = Y   ; Y/N (default No): automatic reweight by station rms

Met obs source = STP 50   ; hierarchical list: RNX ufile GPT/STP [humid value]
                                 ' to match 10.2, use STP 50; new default is GTP 50
Output met = N   ; write the a priori met values to a z-file (Y/N)
Use met.list = N
Use met.grid = N
DMap = VMF1   ; GMF(default)/NMFH/VMF1
WMap = VMF1   ; GMF(default)/NMFW/VMF1
Use map.list = N
Use map.grid = N
Zenith Delay Estimation = Y   ; Y/N (default No)
Atmospheric gradients = Y   ; Y/N (default No)
Gradient Constraints = 0.01   ; gradient at 10 deg elevation in meters; default 0.03 m
Interval Zen = 2   ; 2 hrs = 13 knots per day
Zenith Constraints = 0.5   ; zenith-delay a priori constraint in meters (default 0.5)
Zenith Variation = 0.02 100. ; zenith-delay variation, tau in meters/sqrt(hr), hrs
Ambiguity resolution WL = 0.15 0.15 1000. 10. 500. ; for LC_HELP only
Ionospheric Constraints = 0.0 mm + 8.00 ppm ; for LC_HELP, ok for mid-solar-cycle
Ambiguity resolution NL = 0.15 0.15 1000. 10. 500. ; narrow-lane deviation, sigma (cyc)
Elevation Cutoff = 0   ; default 0 to use value in autcln.cmd
Wobble Constraint = 0.003 0.0001 ; 3 mas .1 mas/day for small networks
UT1 Constraint = 0.00002 0.0001 ; .02 ms .1 ms/day for small networks
Tides applied = 31   ; Binary coded: 1 earth 2 freq-dep 4 pole 8 ocean
                               16 remove mean for pole tide 32 atmosphere
Use otl.list = N
Use otl.grid = Y
Use atl.list = N
Use atl.grid = N
Etide model = IERS03   ; IERS96/IERS03
Apply atm loading = N   ; Y/N for atmospheric loading
Use atml.list = N
Use atml.grid = N
Antenna Model = ELEV   ; NONE/ELEV/AZEL default = ELEV
SV antenna model = ELEV   ; NONE/ELEV   default = NONE
Update tolerance = 0.3   ; minimum adj. for updating L-file coords (def 0.3)
SOLVE print = Y   ; Turn on SOLVE output to screen (default N)
Scratch directory = /tmp

File: **sittbl.**

    SITE   FIX   --COORD.CONSTR.--
        << default for regional stations >>
    ALL   NNN   100. 100.   100.
        << IGS core stations >>
    VILL VILL_GPS   NNN   0.005 0.005 0.01
    MAS1 MAS1_GPS   NNN   0.005 0.005 0.01
    FORT FORT_GPS   NNN   0.005 0.005 0.01

File: autcln.cmd

* Command file for AUTCLN version 3.125 to be used for global and regional data
* Default values are listed with comment flag (non-blank first character)
* Last edited by tah/rwk/scm 030415

* Don't use any GAMIT edits
  use_gamit   no

* Remove more bias flags by allowing a base satellite if multiple slips
   allow_one_bg   yes

* Allow extra missing epochs before flagging a data point if there are frequent
* dropouts in telemetry
* gap_size all 3

* Set minimum elevation for editing and output: 15 10 better for older receivers
* also sets minimum SNR
   site_param all 10 10 0 0

* Set the ionospheric tolerances so you don't throw out too much data.
* These are the current defaults and will work under both low and high
* ionospheric conditions with well-behaved receivers. For poorly tracking
* receivers and low ionosphere, you can improve the editing using
* 240 4 0.3 0.8.
* ion_jump all   30   6 2 5

* Criteria for detecting slips (initial bias flags). Defaults shown.
* First three are for WL, irrelevant for codeless L2 receivers
* Second three (LC) might be set tighter (e.g. 4 0.2 0.5) to catch
* partial-cycle jumps with poorly performing receivers.
* With poor prefit coordinates, set the last two numbers to 2 5 (or 5 10)
* but use the defaults for POST or, with noisy data, skip the postfit
* edit until a second pass with good coordinates allows tight detection of jumps.
* dd_fit_tol 5 2 10   3 0.35 0.8

* The following three commands control the repair of cycle slips and subsequent
* removed of bias flags. The default values are conservative in the sense
* that they retain the most data. They are optimal for global networks but
* will work ok also for regional networks. However, for better ambiguity
* resolution in regional networks, different values are optimal.
*
* Set the tolerances used in trimming the one-way data to remove small
* segments between bias flags. The following are defaults:
* trim_oneway   120 8 0.1 24
* For regional networks use
   trim_oneway   1000 10 0.2 50
* The first two parameters are the minimum times in seconds and minimum
* epochs for attempting to remove a bias flag; the last two are the minimum
* fraction of total span and minimum number of epochs allowed after last bias
* flag. To strengthen ambiguity resolution for regional data, increase the
* last two parameters. For fewer bias flags in 24-hr data increase the first
* two parameters.
*
* Number of data used to repair cycle slips. Defaults are ok for all data but
* all values could be reduced for data sampled less often than 30s.
* dd_return_size 100 50 10 10
*
* DD criteria for removing bias flags: chi-sq ratio chi-sq min max gap gap scale
* For global networks use
* remove_bias 10 3 1800 5
* For regional networks use
   remove_bias 10 3 3600 5
* For fewer flags but more risk over small gaps, decrease the first value (see
* autcln.out). For fewer flags and more risk over large gaps, increase the
* third and decrease the fourth,

* Maximum number of bias flags per SV before deleting all the data.
* Default infinite (not checked).

```
   max_scan_edit   30

* To enhance numerical stability in SOLVE (but be careful in interpreting
* one-way residuals)
    apply_phs_clk 1

* Set the summary filename to agree with the command file produced by FIXDRV
   summary autcln.prefit.sum

* Commands to be used if post-fit editing invoked in the sestbl.
POST   summary   autcln.post.sum
POST   apply_phs_clk 30
POST   use_postfit
POST   postfit_edit 10 4.0
* Remove biases in one-ways after postfit edit
POST pf_remove_bf
* Possibly allow patching over larger gaps
* POST   remove_bias 10   3   3600 2
* Output phase residuals for sky plots
POST   phs_res_root DPH
* Resolve widelane ambiguities in autcln
 POST lc_autcln

* Explicit edits added by sh_autedit or the analyst
x edit_site_sv algo 0 1 2800
x edit_site_sv all 23 1 400
x edit_site_sv trom 15 451 460
         ...
```

File: rcvant.dat

```
# Non-blank first column indicates a comment.
# An asterisk in column 14 indicates that a receiver or antenna is currently supported
# The (new) flags in column 37 for receivers indicate how differential code biases are to
# be treated:
#  'P' : receiver is cross-correlating and requires correction of P2' and C1
#          Rogue SNR, Trimble 4000, etc.
#  'C' : receiver is non-cross-correlating but reports C1 instead of P1
#          Trimble 4700, 5700, Leica RS500, CRS1000, SR9600, etc. unless AS is off
#  'N' : receiver is non-cross-correlating and reports true P1, P2
# Blank indicates that we have not determined the correct flag and GAMIT will stop until
# this file is modified to reflect the correct description of the receiver.
#
RECEIVERS
#
#RECCOD        IGS 20-char code       | Description (comment field)
#format(1x,a6,8x,a20)                 |
#
# Trimble receivers
 TRMSST     * TRIMBLE 4000SST     P |  Dual freq. L1 C/A; L2 squaring; L2 P-code optional
 TR5700     * TRIMBLE 5700        C |  L1/L2 receiver with Maxwell-4 ASIC
 TRNTRS     * TRIMBLE NETRS       N |  L1/L2+L2C with Maxwell-5 ASIC, ethernet, ext freq.
# Ashtech receivers
 ATMCRZ       ASHTECH MICROZ      N |  12  channel, L1/L2 P1/P2 (MicroZ)
 ATZ12T     * ASHTECH Z-XII3T     N |  12  channel, L1/L2 P1/P2 with Metronome option (note
firmware reports "Z-XII3")
 ATZ12G       ASHTECH Z-XII3GETT  N |  12  channel, L1/L2 P1/P2 modified for time transfer
(note: firmware reports "Z-XII3")
 END
#
#
 ANTENNAS
##ANTCOD         _____FULL_NAME_____ |
#format(1x,a6,8x,a15,1x,A4)            |
# Trimble antennas
 TRMSSE     * TRM22020.00+GP       | Geod. L1/L2 compact, with groundplane, Model 22020-00
 TRMZEP     * TRM39105.00          | Zephyr 4-point feed antenna - No Ground Plane
 TRMZGP     * TRM41249.00          | Zephyr 4-point feed antenna - Stealth Ground Plane
 END
```

File: hi.dat

```
# File: hi.dat  Format version 1.0  (keep the version number in columns 32-24 of line 1)
# Table of mechanical offsets between measured height-of-instrument (HI) and the antenna #
reference point (ARP)
# Entries last changed by rwk 060727
#
# Non-blank first column is a comment
# Comments can follow within the line (unread)
#
# Some antennas have equivalences in gamit/lib/hisub2.f and are given here only once.
# If the antenna you want is not in the equivalence list, you can add it to the table.
# A warning will be issued for entries missing from the table, and offsets set = 0.
# station.info entries of L1PHC or UNKNWN DHARP are both given 0. offsets with no warning.
#
# Format (1x,a20,1x,a6,1x,f6.4,1x,f6.4)
# 20-char RINEX code  6-char GAMIT code   5-char HI code  vert offset (m)    horiz offset (m)
 JPLD/M_R             ROGSNR DHARP 0.      0.      ! ARP is bottom of choke ring / base of antenna
 JPLD/M_R             ROGSNR DHBCR 0.      0.      ! direct ht to bottom of choke ring
 JPLD/M_R             ROGSNR DHTCR 0.0699 0.      ! direct ht to top of choke ring (JPL)
 JPLD/M_R             ROGSNR SLBCR 0.0699 0.1905 ! slant height to bottom edge of choke ring
```

Antenna Effects

Antenna-specific effects

    Ground-antenna phase-center variations (PCVs)

        IntroGG 1.2;   file antmod.dat

        Mader, G.L., NGS: http://www.ngs.noaa.gov/ANTCAL/Files/summary.html

Site-specific effects

        Elosequi et al., *J. Geophys. Res., 100*, 9921, 1995.

Satellite antenna effects

        Schmid and Rothacher, "Estimation of elevation-dependent satellite antenna phase center variations of GPS satellites, *J. Geod.*, *77*, 440, 2003.

Tropospheric Effects

Errors in geodetic measurements
>mapping functions in hydrostatic ("dry") delay

>[http://gauss.gge.unb.ca/papers.pdf/igs97tropo.pdf]

>gradients [Chen and Herring, *J.Geophys. Res., 102*, 20489, 1997; *GAMIT* Chap. 7]

>parameterizing the zenith delay for estimation

Tutorial on all aspects: http://bowie.mit.edu/~tah/12.540/12.540.Lec15.html

Extracting precipitable water from GPS measurements
>model correctly the "dry" delay (pressure measurements, mapping function)
>zenith wet delay
>z-files, sh_metutil
>tomography

Tutorial and research results: http://www.gpsmet.noaa.gov
>(click on 2000 and 2002 Techincal Reviews_)

File: sh_metutils

sh_metutil calls gamit/utils/metutil to read estimated zenith delays from a GAMIT o-file or
a SINEX zpd file and compute zenith wet delay (ZWD) and precipitable water (PW) using
the zenith hydrostatic delay (ZHD) computed using pressure values from a RINEX met file
or a GAMIT z-file.

```
  Usage: sh_metutil -f [ZTD file] -m [RINEX met files] -z [z-file] -i [interval

    where  [ZTD file] is the name of the SOLVE -file ( o[expt]a.ddd )
           [RINEX met files ] gives the list of RINEX met files to be used (wildcards ok)  )
           [z-file] gives the list of z-files to be read (wildcards ok)
           [interval] is the epoch interval of the output file
               E  : use the interval of the ZTD file values (default)
               O  : use the interval of the z-file (GAMIT observations0
              nn  : value in seconds of the interval

     Notes: (1) ZTD file is required
            (2) Either a RINEX met file or a GAMIT z-file is required
                (for now, you cannot have both)
            (3) The start time will always be set by the ZTD file

     Examples: sh_metutil  -f oeuraa.223  -z zkosg4.223
               sh_metutil  -f oeuraa.223  -m *2230.04m  -s 1.6
               sh_metutil  -f oeuraa.223  -z z*4.223 -i O

    Output files are named met_ssss.yyddd where ssss is the site name from the
    z-files or RINEX met files, yy is the 2-digit year, and ddd is the day-of-year
```

```
File: otesta.220  (GAMIT o-file from SOLVE; machine readable version of q-file)
                                (Adj m      Sigma     Estimate)
ATM_ZEN X KAZA  2 2000  8  7  0  0  0.0363 +-  0.0126    2.1079
ATM_ZEN X KAZA  2 2000  8  7  2  0  0.0294 +-  0.0084    2.1010
ATM_ZEN X KAZA  2 2000  8  7  4  0  0.0170 +-  0.0078    2.0886
...
ATM_ZEN X KIT3  3 2000  8  7  0  0 -0.0082 +-  0.0154    2.2540
ATM_ZEN X KIT3  3 2000  8  7  2  0 -0.0054 +-  0.0106    2.2568
ATM_ZEN X KIT3  3 2000  8  7  4  0 -0.0118 +-  0.0099    2.2504
...
```

```
File:  zkaza0.220  (GAMIT z-file from MODEL)

* A priori atmospheric values for KAZA
* Models:  Dry Zen SAAS  Wet Zen SAAS  Dry Map NMFH  Wet Map NMFW
* Yr  Doy Hr Mn Sec  PRN  Azimuth  Elevation  Pres    Temp    WV Pres
2000 220  0  0 30.    4   47.2360  52.2177    858.5   293.2   11.7
2000 220  0  0 30.   24    4.8970  85.9935    858.5   293.2   11.7
2000 220  0  0 30.   30  310.4261  32.4934    858.5   293.2   11.7
2000 220  0  1  0.    4   47.2447  51.9959    858.5   293.2   11.7

 Dry Zen Wet Zen  Total Zen  Dry Map   Wet Map  Dry Slant  Wet Slant Total Slant
 1.9562  0.1154     2.0716   1.2643    1.2648    2.4733     0.1460     2.6193
 1.9562  0.1154     2.0716   1.0024    1.0024    1.9610     0.1157     2.0767
 1.9562  0.1154     2.0716   1.8559    1.8589    3.6305     0.2145     3.8451
 1.9562  0.1154     2.0716   1.2681    1.2686    2.4808     0.1464     2.6272
```

Using GAMIT effectively (pitfalls and refinements)

Setup
    `process.defaults` [*IntroGG* 2.3]
    `sites.defaults` [IntrodGG 2.3]
    `station.info` [*IntroGG* 2.1; *GAMIT* 2.3
    a priori coordinates [*IntroGG* 2.1; *GAMIT* 2.2]
    network splits [*GAMIT* 2.3]
    session splits
    makexp messages (missing or misnamed files)
    makex messages (`DATA REJECTED`; *GAMIT* 2.8]
    fixdrv messages (clock behavior; *GAMIT* 2.10, 3.2]
    model messages (`RCLOCK`)

Problems with *autcln*
    # 1 : poor a priori coordinates
    interpreting `autcln.post.sum`

Modeling and recovering the troposphere
    elevation-dependent weighting (n-files)
    piecewise-linear model for zenith delay and gradients
    recovering precipitable water vapor

Ambiguity resolution
    widelanes with pseudorange in *autcln*
    ionospheric constraint [Dong and Bock, *J. Geophys. Res., 94*, 3949, 1989; *GAMIT* 3.4
    tolerances for deviation from an integer
    constraints for the "tight" solution

Using GLOBK effectively (subtleties and pitfalls)

What *globk* does

    Initialization (*glinit*)

        decode the command file (`com_file`, `srt_file`, `lst_file`, `eq_file`, `make_svs` *first*)

        read headers of all h-files and sort by time

        report any (GAMIT) model differences among h-files (EOP, tides)

        make a file of a priori satellite parameters (`svs_file`)

        read the `eq_file` and generate names of stations

        initialize apriori values of parameters from the h-file estimates

        based on `use_site`/`use_pos`/`use_num` commands, make a list of stations to be used

        read apr_file and replace apriori coordinates for any stations on the apr_file

        based on `apr_` and `mar_` commands, make a list of parameters to be estimated

        initialize the covariance matrix based on the values in the `apr_` commands

    Forward Kalman filter (*glfor*) — for each step (h-file),

        update the state vector and covariance by applying the process noise

          (first epoch may do a direct copy of the h-file covariance if all aprior sigmas > 10 m

           and no additional parameters—message printed)

        read parameter estimates and covariance from h-file

        apply corrections to a priori coordinates, orbital parameters, or EOP for any

          differences between h-file and apriori (`apr_file`, `svs_file`, `in_pmu` file)

        generate appropriate station names based on `eq_file` explicit renames and earthquakes

          (h-file must start after and end before the time span of the rename)

        generate new a priori values of coordinates using `EXTENDED` option for non-secular motion

        check differences between the h-file estimates and the current state vector;

          estimate a rotation between the networks implied by the two sets of coordinates, and

           if too large, apply the rotation to the h-file estimates

          if one or more coordinates differ by too much after rotation, remove the station

        remove from the solution (by setting to zero their partial derivatives in the Jacobian) any

           parameter not included by an `apr_` command or excluded by the previous step

        perform a trial solution by computing the chi-square increment, skipping the h-file if too large

        perform the full solution, incrementing the parameter values and covariance matrix

    At the end, write the solution vector and covariance matrix into the `sol_file` (for *glorg*) and print

        file and optionally to an output h-file (`out_glb`) for another *globk* run (*glout*)

    If a Kalman back solution has been requested (`bak_file`), repeat the stepping through the h-files

        but in reversed order ("forward" solution can be forward or backward in <time>); same as

        forward solution except that the forward and backward estimates are averaged and the solution

        is output (`sol_file` and print) at each step

    Mathematical references: Herring et al. [*J. Geophys. Res., 95*, 12561, 1990]

                             Dong et al. [*J. Geod.*, 72, 200, 1998]

Using GLOBK, cont.

What *glorg* does

Reads the GLOBK com file for controls to read the sol file and loads the loosely constrained solution

Applies constraints to link the adjustments of parameters and/or force them to zero (equate and force commands)

Applies frame constraints in position and/or velocity (separately), estimating translation and/or rotation and/or scale parameters to minimize the adjustment of position or velocity for the stations in the stab_site list (iterates to determine weights)

Estimates rotation vectors between stations defining plates (plate and assign_p)

Writes out full Cartesian estimates and, optionally, position and/or velocity in a local frame

```
++++++++++++++++++++++++++++++++++++
 + GLORG              Version 5.08I +
 +++++++++++++++++++++++++++++++++++

FIXA option set: Updating Velocity  of NYA1_GPS from NYAL_GPS
FIXA option set: Updating Velocity  of HARB_GPS from HART_GPS

Stabilization with  50.0% constant,  50.0% site dependent weighting.
 Delete sites with  10.0-sigma condition.
 Height variance factor    1000.00 Position,   1000.00 Velocity
 Min dH sigma Position 0.0050 m;    Min Position RMS 0.0030 m
 Min dH sigma Velocity 0.0050 m/yr; Min Velocity RMS 0.0030 m/yr

 Velocity system stabilization results
 -------------------------------------
 X Rotate (mas/yr)      0.10514 +-     0.00603 Iter  4 sum_mgk95_01_021215rs.gdl
 Y Rotate (mas/yr)      0.34850 +-     0.00640 Iter  4 sum_mgk95_01_021215rs.gdl
 Z Rotate (mas/yr)      0.89303 +-     0.00435 Iter  4 sum_mgk95_01_021215rs.gdl
 X Trans   (m/yr)       0.00067 +-     0.00020 Iter  4 sum_mgk95_01_021215rs.gdl
 Y Trans   (m/yr)      -0.00386 +-     0.00019 Iter  4 sum_mgk95_01_021215rs.gdl
 Z Trans   (m/yr)      -0.00172 +-     0.00013 Iter  4 sum_mgk95_01_021215rs.gdl
 Condition Sigmas used    0.0000    0.0000    0.0000    0.0000    0.0000    0.0000
Sites and relative sigmas used in stabilization
VILL_GPS 0.93  KELY_GPS 0.95  STJO_GPS 0.93  BRMU_GPS 0.93  SCH2_GPS 0.98  THU1_GPS 0.95
ALGO_GPS 0.93  RCM5_GPS 2.07  NLIB_GPS 0.93  CHUR_GPS 0.94  DUBO_GPS 0.96  FLIN_GPS 0.94
MDO1_GPS 0.93  PIE1_GPS 0.93  YELL_GPS 0.93  THTI_GPS 1.06  KOKB_GPS 0.93  CHAT_GPS 0.95
KWJ1_GPS 0.95  MARC_GPS 1.08  TRUK_GPS 1.03  VLAD_GPS 0.98  YAKT_GPS 0.96  IRKT_GPS 0.93
KSTU_GPS 0.96  NRIL_GPS 1.00  ARTU_GPS 0.98  ZWEN_GPS 0.93  METS_GPS 0.94  KIRU_GPS 0.94
BOR1_GPS 0.94  GRAZ_GPS 0.94  POTS_GPS 0.93  WTZR_GPS 0.94  ONSA_GPS 0.93  NYAL_GPS 0.97
KOSG_GPS 0.93  BRUS_GPS 0.94
 For  114 Velocity Iter  4 Pre RMS     0.0104 m/yr; Post RMS     0.0004 m/yr

 Equating parameters:   39 Equates to be applied
  #    Sigma    dChi**2    List of parameters
  1:  0.00000      1.03 YUZN_GPS ND YSSK_GPS ND
  2:  0.00000     13.50 YUZN_GPS ED YSSK_GPS ED
  3:  0.00000      5.73 YUZN_GPS UD YSSK_GPS UD

 39:  0.00000      0.16 HART_GPS UD HARB_GPS UD
 Total change in Chi**2/f is     1.69 for   39 equates, and   39 conditions
 Solution chi**2/f now     0.68 with   41169 degrees of freedom




 PLATE ROTATION VECTOR RESULTS
 ----------------------------
```

```
SITES USED TO ESTIMATE POLE POSITIONS
-----------------------------------
 PLATE       SITES
 EURA_GPS : VILL_GPS VLAD_GPS YAKT_GPS IRKT_GPS KSTU_GPS NRIL_GPS
            ARTU_GPS ZWEN_GPS METS_GPS KIRU_GPS BOR1_GPS GRAZ_GPS
            POTS_GPS WTZR_GPS ONSA_GPS NYAL_GPS KOSG_GPS BRUS_GPS
 NAFD_GPS : KELY_GPS STJO_GPS BRMU_GPS SCH2_GPS THU1_GPS ALGO_GPS
            RCM5_GPS NLIB_GPS CHUR_GPS DUBO_GPS FLIN_GPS MDO1_GPS
            PIE1_GPS YELL_GPS
 PCFC_GPS : THTI_GPS KOKB_GPS CHAT_GPS KWJ1_GPS MARC_GPS TRUK_GPS
SITES ASSIGNED TO PLATE BUT NOT USED IN ESTIMATE
------------------------------------------------
 PLATE       SITES
 EURA_GPS : FAIR_GPS BILI_GPS _KMS_GPS OSSO_GKA _TIG_GKA UHAZ_GKA
            OMS1_GPS TAL1_GPS SEY2_GPS MAG0_GPS SUS1_GPS KUL1_GPS
            TOM1_GPS UNR1_GPS OKHA_GPS YSSK_GPS TSKB_GPS TKL1_GPS
            KHAJ_GPS VLAD_GPS YAKT_GPS TIXI_GPS DAEJ_GPS SUWN_GPS
            XIAN_GPS


TRANSLATION  X (mm/yr) +-    Y  (mm/yr) +-       Z  (mm/yr) +-     RhoXY    RhoXZ    RhoYZ
              -0.30    0.36    0.32    0.40  -0.38    0.25  -0.134 -0.293  0.086   TRAN


PLATE      Wx (deg/My)  +-      Wy (deg/My)  +-     Wz (deg/My)    +-    RhoXY  RhoXZ  RhoYZ
EURA_GPS 0.004364  0.003972  0.000491 0.003257 -0.002378 0.003525  0.117  0.096 -0.063
NAFD_GPS 0.064429  0.003552 -0.061248 0.004752 -0.214216 0.005111  0.044  0.046 -0.417   XYZ
PCFC_GPS -0.058197 0.005374  0.414789 0.002824 -0.816597 0.004482 -0.109  0.091 -0.047   XYZ


PLATE      Lat. (deg)  +-  Long (deg)  +-    Mag (deg/My)  +-     RhoLtLg RhoLtMg RhoLgMg
EURA_GPS  -28.430  43.377    6.419  41.939   0.004994  0.003766  -0.028  0.155  0.099  LLM
NAFD_GPS  -67.462   1.194  -43.550   2.779   0.231928  0.004399  -0.344 -0.410  0.230  LLM
PCFC_GPS  -62.846   0.202   97.987   0.724   0.917751  0.004297   0.177 -0.292  0.171  LLM


PLATE -  PLATE         Wx (deg/my)   +-   Wy (deg/my) +-      Wz (deg/My) +-    RhoXY  RhoXZ  RhoYZ
EURA_GPS-NAFD_GPS -0.060065  0.003725  0.061739  0.004725  0.211838  0.007041 -0.044  0.357 -0.435
EURA_GPS-PCFC_GPS  0.062562  0.007474 -0.414298  0.005692  0.814219  0.006691 -0.033 -0.128 -0.020
NAFD_GPS-PCFC_GPS  0.122626  0.007309 -0.476037  0.006470  0.602381  0.007174  0.039 -0.135 -0.270


PLATE -  PLATE       Lat (deg) +-  Long (deg) +-  Mag (deg/My) +-       RhoLaLg RhoLaMa RhoLgMa
EURA_GPS-NAFD_GPS 67.873  1.485   134.212  2.759   0.228681  0.005783   0.210  0.665  0.064  LLM
EURA_GPS-PCFC_GPS 62.770  0.375   -81.413  1.013   0.915702  0.006497  -0.163  0.122 -0.074  LLM
NAFD_GPS-PCFC_GPS 50.784  0.439   -75.555  0.853   0.777503  0.007597  -0.166  0.060 -0.125  LLM
 Checking covariance matrix after equate and force
 Global Multi-epochs for velocity


SUMMARY VELOCITY ESTIMATES FROM GLOBK Ver 5.07I
 Long.   Lat.    E & N Rate     E & N Adj.     E & N +-    RHO      H Rate  H adj.    +-  SITE
 (deg)   (deg)    (mm/yr)        (mm/yr)       (mm/yr)             (mm/yr)
356.048  40.444  0.08 -0.21    0.59  -0.13   0.75  0.74   0.000   -3.23  -3.23    0.90 VILL_GPS*
344.367  27.764 -3.62  0.66  -20.39 -14.73   0.83  0.82   0.002   -1.22  -0.70    0.90 MAS1_GPS
309.055  66.987 -18.72 -1.60   -0.37  -0.33   0.78  0.78   0.000   -4.08  -4.08    1.02 KELY_GPS*
  . . .
VEL STATISTICS: For 28 RefSites  WRMS ENU 0.58  0.65  2.15 mm/yr    NRMS ENU 3.40  3.96  4.49
```

globk/glorg: parameterization and controls

Treatment of SV orbital parameters [*GLOBK,* pp. 39-40, 46-48]
    tight, moderate, and loose apr_svs, mar_svs
    linking h-files on a day

Treatment of EOPs (apr and mar) [*GLOBK,* pp. 27-28, 40-41]

Error Models
    h-file reweighting / chi-square increments [*GLOBK*, pp. 50-51]
    white and randow walk noise reweights sig_neu mar_neu [*GLOBK*, pp. 46-47]

Frame, center of mass, and plates [*GLOBK*, pp. 37-39]
    time-variable center of mass *Dong et al.*, Appendix C, *GLOBK*, p. 28]
    3-D frame stabilization [GLOBK, pp. 33-39]
    plate and local frames
    global/regional w/o rotation
    repeatability vs velocity solutions

Using the log file
    bad coordinates
    large rotations
    global/regional conflict

Handling earthquakes [*GLOBK ,* pp. 29-32]
    EQ definition and radius of influence
    co-seismic constraints
    post-seismic constraints

Handling reference monument ties
    rename/equate (*globk+glorg*) [*GLOBK,* p. 31]
    supplementary h-files
    equates and force – importance of apr values (FIXA command)

Using *hfupd* and renames to correct height problems [*GLOBK*, p. 79-80]

File: globk_comb.cmd

```
* GLOBK command file for daily h-files (repeatability or combination)
*
* This group must be first
   eq_file ../tables/eq_renames
   make_svs ../tables/sat1.apr
   com_file comb.com
   srt_file comb.srt
   sol_file comb.sol

* Earth-rotation values  (not needed if pmu free in final combination)
   in_pmu  ../tables/pmu.bull_b

* File(s) for a priori coordinates
   apr_file ../tables/itrf00.apr

* Optionally use separate file for sites to be included and random or Markov noise
x  source ../tables/daily.uselist
x  source ../tables/daily.reweight

* (1) Max chi**2, (2) Max prefit diff, (3) Max rotation; defaults are 100 10000 10000
   max_chi 30 50 2000.0

 * Apply the pole tide whenever not applied in GAMIT
   app_ptid ALL


* Allow the network to be loose since using glorg for stabilization
   apr_neu  all  10 10 10  0 0 0

* Satellites are loose if using global data
   apr_svs all   100 100 100 10 10 10  1R
* but tight if not combining with global data
x   apr_svs all .05 .05 .05 .005 .005 .005 .01 .01 FR

* EOP loose if estimating rotation in glorg
   apr_wob  100 100 10 10
   apr_ut1  100  10
* if combining days, possibly add day-to-day noise to absorb rotation-like noise
x  mar_wob   1 1 0 0
x  mar_ut1    1 0

* Set minimal globk print options since using glorg output
   prt_opt NOPR

* Invoke glorg for stabilization
   org_cmd glorg_comb.cmd
   org_opt PSUM GDLF CMDS

* Write out an h-file if needed for future combinations
x  out_glb  H------.GLX
```

File: daily.uselist

```
# Start from zero
 use_site clear

# Includes sites within NAM and PAC
 use_pos +25. 180. 85. 310.
 use_site kely thu1

# Remove SCIGN site that existed for only part of 2001 (vandalism)
 use_site -SKYB_@
```

File: eq_renames

```
* Rename before EQ renames to avoid conflict with SoCal site LAE1
 rename LAE1_GPS  LAE1_IGS SIO 1997 1 1 0 0 2100 1 1 0 0


* Earthquake:
*   Izmit
  eq_def   IZ  40.702 29.987 300 17.0 1999 08 17 00 00
  eq_renam IZ
  eq_post  IZ 90   0.1  0.1   0.1     1.8  1.8  0.7   Post: 0.1 mm**2/day
  eq_renam IZ

# Temporary to fix problem of mistranslated RINEX files in the archive
 rename WTM2_GPS WETM_GPS 1989 5 23 0 0 1991 7 24 0 0
 rename WETM_GPS WETM_XCL 1991 7 24 0 0 1992 1  1 0 0

# Temporary to fix Hunter 1991 conflict with continuous site from 2001
 rename HUNT_GPS HNTR_GPS 1993 1 1 0 0 1997 12 31 24 0

# Bad continuous stations
 rename BILL_GPS BILL_XCL 1997 7  1  0  0
 rename HARV_GPS HARV_XCL 1992 1 1 0 0 2100 1 1 0 0

* Now apply special renames for antenna changes
*
 rename WUHN_GPS WUHN_1PS 2002  1 26  0  0
 rename kely_gps kely_1ps 2001  9 14  0  0
```

File: daily.reweight

```
#  Downweight verticals with unresolved HI problems
  sig_neu @_xhi  0. 0. 1.
  sig_neu @_xnr  0. 0. 1.

# High noise in continuous stations (more noise may be needed in velocity run)
 sig_neu cit1@ 0 0 .005 1994 1 1 0 0  2100 1 1 0 0
 sig_neu chil@ 0 0 .005 1995 1 1 0 0  2100 1 1 0 0

# Outliers in 2003 from Dec 2005 analysis
 sig_neu algo@     0.030  0.030  0.000  2003  1 30  0  0  2003  2  9 24  0
 sig_neu algo@     0.000  0.000  0.010  2003  9 25  0  0  2003 12 18 24
 sig_neu aoml@     0.005  0.005  0.020  2003  1 11  0  0  2003  6 30 24  0
# This one systematic
 sig_neu prds@     0.030  0.030  0.030  2003  1 11  0  0  2003  4 18 24  0
```

File: glorg_comb.cmd   GLORG command file for combination or repeatabilities

```
        * Stabilization using IGS stations
          apr_file ../tables/itrf00.apr
        * Regional stabilization using coordinates from a prior solution
        x  apr_file ../tables/globk_vel_990306.apr

        * Define the stabilization frame
          source ../tables/stab_site.global
        x  source ../tables/stab_site.regional

        * Set parameters to estimate in stabilization
          pos_org  xrot yrot zrot xtran ytran ztran

        * Default height ratio is 10; increase if heights questionable
          cnd_hgtv 1000 1000 2.0 10.0

        * Default iterations is 4, relative weight ratio 50%,  horizontal sigma cutff 4.0
        x  stab_ite 4 0.8 3.
```

File: stab_site.global

```
  stab_site clear
  stab_site vill fort kour brmu thu1 sant areq algo nlib pie1 yell drao
# omit FAIR after Denali EQ
 fair_gps
-fair_gps -fair_gdn R SIO 2002 11 2 0 0
 chat auck kwj1 mcm4 mac1 tidb hob2 guam tskb pert yar1 cas1
 irkt lhas kit3 bahr mali zwen mate onsa nyal
* added by rwk for 1992 and early 1993
 albh graz wett usud usu2 gold_gps -darw kosg stjo
 rcm2 ricm wsfm mcm0 well ds41 darw hart hob1 town
x for late 1993 ff
```

File: stab_site.regional

```
* Stabilization list for E Asia repeats from solution vel_031007.org, 1995-2003
*
 stab_site clear
 stab_site  BILI_GPS  !       0.54    0.52     2.67
 stab_site  PETP_GKA  !       0.50    0.47     1.12
 stab_site  MAG0_GPS  !       0.79    0.78     1.84
x stab_site  USUD_GPS !       0.23    0.19     0.46
x stab_site  DAEJ_GPS !       0.46    0.41     1.14
 stab_site  TAEJ_GPS  !       0.46    0.41     1.14
 stab_site  SUWN_GPS  !       0.41    0.33     0.86
stab_site  SHAO_GPS   !     0.40    0.31     0.89
   stab_site -shao_gps R CHINA_0109
 stab_site  BJFS_GPS  !       0.50    0.46     1.69
x stab_site  WUHN_1PS  !      0.71    0.57     3.18
stab_site  WUHN_GPS   !     0.71    0.57    3.18
 stab_site  XIAN_GPS  !       1.06    0.74     2.13
x stab_site  TYP1_GPS !       1.20    0.80     2.40
 stab_site  TYP2_GPS  !       1.20    0.80     2.40
stab_site  LSC1_GPS   !     0.50    0.39    1.28
x stab_site  RJJ2_GPS !       6.45    1.81     6.25
 stab_site  MZZ1_GPS  !       0.83    0.60     1.68
x stab_site  NRIL_GPS !       1.21    1.17     2.91
 stab_site  URUM_GPS  !       0.53    0.49     2.20
x stab_site  NVSK_GPS !       1.82    1.62     4.38
stab_site  POL2_GPS   !     0.24    0.20    0.49
stab_site  ARTU_GPS   !     0.46    0.44    2.32
```

File: globk_vel.cmd

```
     eq_file ../tables/eq_renames
     com_file vel.com
     srt_file vel.srt
     sol_file vel.sol
 * Run the solution backwards in time (default is forward)
 x  srt_dir -1

 # Earth-rotation values (use only if rot not free in globk and glorg, and daily h-files)
 x in_pmu  ../tables/pmu.bull_b

 * File(s) of a priori coordinates for combination (may be overrriden by glorg)
     apr_file china_040622b.apr
     apr_file ../tables/itrf00_noam.apr

 * Optionally use separate file for sites to be included and random or Markov noise
 x  source ../tables/vel.uselist
 x  source ../tables/vel.reweight

 * (1) Max chi**2, (2) Max prefit diff, (3) Max rotation; defaults are 100 10000 10000
     max_chi 5 2. 20000

 * Invoke GLORG and set print options
     crt_opt NOPR
     prt_opt NOPR
     org_cmd glorg_vel.cmd
     org_out globk_vel.org
     org_opt PSUM CMDS GDLF VSUM FIXA RNRP

 * Loose apr for glorg
     apr_neu  all 10 10 10  0.2 0.2 0.2
     apr_wob  10 10 10 10
     apr_ut1  10 10
     mar_wob   3650 3650  365 365
     mar_ut1   365 365

 * Allow translation and scale variations to account for global frame errors
 * and SV constellation shift
     apr_tran 1 1 1 0.1 0.1 0.1
     apr_scale 10 1.
     mar_tran  3.65  3.65  3.65     0  0  0
     mar_scale  365   0

 * Random (sig_neu) and Markov (mar_neu) reweights
     source ../tables/vel.reweight
```

File: vel.reweight

```
* Random and Markov reweights for velocity solution (on top of comb reweights)
# reweight all monthlies to avoid too-small uncertainties in repeats
 sig_neu @ .001 .001 .005
# also add Markov horizontal 1**2 mm/yr, vertical 3**2 mm/yr
 mar_neu all .000001 .000001 .000009 0 0 0

# High noise in continuous stations (noise also added in daily combinations)
 sig_neu cit1_gnr 0 0 .005 1994 1 1 0 0  2100 1 1 0 0

# Downweight all sites in ETS-affected area by 3 mm to account for
# elevated 'noise' from the slip
 sig_neu albh@ .003 .003 0
 sig_neu youb@ .003 .003 0
```

File: glorg_vel.cmd

```
* GLORG command file for velocities and positions

* Define the stabilization frame
  apr_file ../tables/itrf00.apr
  source ../tables/ .global
x source ../tables/ .regional


* Coordinate/velocity files for stabilization and matching apriori values
  apr_file 040622a.apr
  apr_file ../tables/itrf00.apr


* Set parameters to be estimated (include scale only if estimated in globk)
  pos_org xtran ytran ztran xrot yrot zrot scale
  rate_org xtran ytran ztran xrot yrot zrot scale


* Default height ratio is 10; increase if heights questionable
  cnd_hgtv 1000 1000 2.0 10.0

* Default iterations is 4, relative weight ratio 50%,  horizontal sigma cutff 4.0
x  stab_ite 4 0.8 3.


* Get velocities relative to defined plates (extract using sh_org2vel)
  plate NAFD_GPS KELY_GPS STJOS BRMU THU1_GPS ALGO NLIB MDO1 PIE1 YELL
  plate PCFC mkea kwj1 chat
* Keep the ITRF00-NNR translation rates when estimating plates
   (default is to estimate simultaneously)
x  NOPLATETRAN


* Apply equates

* link velocities of stations within 1 km  (a prioris should match, aided by FIXA)
  eq_dist 1000 ndot
  eq_dist 1000 edot
  eq_dist 1000 udot
* link some more separated by more than 1 km
  equate ftor_gps ndot ords_gps ndot for2_gps ndot
  equate ftor_gps edot ords_gps edot for2_gps edot
  equate ftor_gps udot ords_gps udot for2_gps udot
* unlink some that don't work
  unequate wsfd udot
  unequate enda_gla ndot
  unequate enda_gla edot
  unequate enda_gla udot
* link some horizontal positions when heights are uncertain
  equate soli_gps npos soli_xhi npos
  equate soli_gps epos soli_xhi epos
* link some positions across earthquakes when a model has been applied in the eq_file
  source LA_equates
```

```
File: glist.out   from running      glist china.gdl china.glist +1 eq_file ' ' china_050622b.apr

Summary of SITE occurences in china.gdl
 Use of sites for  488 sites
      soln/CHINA_9911.GLX
99 12  17   2  11  20  22  23  32  35  41  45  47  49  59  61  70  71  74  79  80  83
   89  92  96  97 100 103 117 124 125 129 132 140 143 144 152 153 155 160 167 168 169
  171 198 209 223 230 237 239 256 258 259 273 283 284 293 301 302 303 312 394 401 408
  482 486  -1  -1  -1  -1  -1  -1  -1  -1  -1  -1  -1  -1   1 /raid1/rwk/china99/g
      gsoln/CHINA_0306.GLX
103  7 31   1   2   4   7   8   9  10  11  13  14  16  17  18  19  21  22  24  26  28
   31  33  34  36  37  38  40  42  43  45  46  50  52  53  54  56  58  59  60  61  63
   66  67  68  69  70  71  72  74  75  76  79  80  86  87  89  90  92  93  94  95  96
   98  99 102 103 104 106 108 110 112 114 116 117 118 119 124 125 126 129 132 134 137
  139 140 142 143 144 147 148 149 151 152 155 160 161 162 163 164 166 167 168 170 173
  453 454 455 457 458 459 461 462 464 465 466 467 468 469 470 471 472 474 475 476 477
  478 480 481 486  -1  -1  -1  -1  -1  -1  -1  -1  -1 /Hfiles/H2003184_2

 SUMMARY of occurences
    1. VESL_GPS   4 2003.6-2005.5  1.93      2. VILL_GPS  25 1995.4-2005.5 10.12
    3. MADR_GPS   8 1993.4-2005.5 12.11      4. MADR_XCL   1 2003.6-2003.6  0.00
    5. MAD2_2PS   3 2005.3-2005.5  0.19      6. SFER_GPS   3 2005.3-2005.5  0.19
  ...
  483. TLSE_GPS   3 2005.3-2005.5  0.19    484. HERS_GPS   6 1995.4-1997.4  1.99
  485. HERS_1PS   2 1998.6-1998.6  0.06    486. HERS_XCL  12 1999.9-2005.5  5.60
  487. USU3_GPS   0    0.0-   0.0  0.00    488. MDX2_GPS   0    0.0-   0.0  0.00


. SUMMARY of site position and occurences P
.  Long      Lat        Ht     #  First    Last    Dur.  Name     Seq P
.  deg       deg        km                         yrs                P
  357.1582 -71.6738   0.8624    4 2003.579 2005.511  1.93 VESL_GPS    1 P
  356.0480  40.4436   0.6474   25 1995.396 2005.511 10.12 VILL_GPS    2 P
  355.7503  40.4292   0.8295    8 1993.404 2005.511 12.11 MADR_GPS    3 P
  355.7503  40.4292   0.8295    1 2003.579 2003.579  0.00 MADR_XCL    4 P
...
    0.3363  50.8673   0.0765    6 1995.396 1997.388  1.99 HERS_GPS  451 P
    0.3363  50.8673   0.0765    2 1998.563 1998.623  0.06 HERS_1PS  452 P
    0.3363  50.8673   0.0765   12 1999.914 2005.511  5.60 HERS_XCL  453 P

 There were  323 site renames listed.  Renames used are:
  # Orig   New     Specific Period from   -----> To   Position change (m)
  1 MDX2_GPS->MDX1_GPS   2003/ 3/ 1  0: 0  2003/ 9/ 1  0: 0   0.0000  0.0000  0.0000
 10 AREQ_GPS->AREQ_XCL   2001/ 6/22  0: 0  2003/ 4/20  0: 0   0.0000  0.0000  0.0000

 There were   14 earthquakes listed.  Earthquakes used are:
  #  CODE   Lat (deg)  Long (deg) Radius (km) Depth (km)    Date       Rename?
  5   HT    34.5900   243.7300    200.0000    5.0000 1999/10/16 11:46   YES
  7   KA    54.3100   161.9100    600.0000   33.6000 1997/12/ 5 11:26   YES
 10   AR   -17.2800   287.2900    700.0000   29.6000 2001/ 6/23 20:34   YES
 11   KU    35.5400    92.7500   1000.0000   15.0000 2001/11/14  9:26   YES
 12   DN    63.7400   212.3100    600.0000   10.0000 2002/11/ 5  0: 3   YES
 13   MI   -50.1500   160.3700   2500.0000   20.0000 2004/12/24  1:59   YES
 14   SU     4.5000    95.0000   2500.0000   20.0000 2004/12/26  0:57   YES
```

Use to check:
 - correct path/filename in gdl file
 - estimate/apr errors from misidentified sites or bad solutions
 - correct application of renames
Can provide input to program *gen_uselist* to generate use_site list based on span

Defining the reference frame

Mathematical methodology [*Dong et al.*, 1998]
   finite constraints – GLOBK apr_neu
   generalized constraints – GLORG , plate

Implementation and geometric considerations [*GLOBK* pp. 41-43]
   global frame
     ITRF
     NUVEL [Shen et al., *J. Geophys. Res.*, 5721, 2000]
     ITRF rotation poles [Altamimi et al., *J. Geophys. Res.*, 2214, 2002]
   frames defined by plates or crustal blocks.
     [Chen et al., *J. Geophys. Res., 105*, 16215, 2000]
   impact of frame translation on estimated plate rotations
     [Steblov et al., *Geophys. Res. Lett., 30*, 1924, 2003GL017805, 2003]

Analysis of a complex multi-year data set – Southern California 1992-1999

Run sh_gamit for to get daily h-files for each survey; e.g. for 1994:

    sh_gamit -expt scec -s 1994 129 138 -pres Y -copt o q mkx -dopt D ao c ps x >&! sh_gamit.log

        `--> hsceca.94130, hsceca.94131, ....`

Combine the daily h-files from the GAMIT solution with California and global daily h-files generated by SOPAC, and generate time series of daily residuals for inspection (`globk_comb.cmd`):

  sh_glred -s 1994 129 1994 2001 146 -expt scec -local -net igs1 net1 -opt H G E >! sh_glred.log

Using the time series, remove or downweight outliers:

  -add _XCL renames to `scec_eq` (also has the Landers EQ defined)

  -add sig_neu downweights to `scec_comb.reweight`

Aggregate (combine) all of the daily files into 'monthly' or 'survey' H-files spanning 15-30 days (fewer immediately after the EQ):

  sh_glred -s 1994 129 1994 2001 146 -expt scec -ncomb 18 -local -net igs1 net1 -opt H G >! sh_glred.log

    `--> (e.g.) H940509_SCEC.GLX`

Generate a list of H-files for the final GLOBK runs:

  – from /gsoln,   ls ../glbf/*.GLX > scec.gdl

The following steps are useful to understand the data content, detect bad aprioris or estimates, and to select the stations to be included in the solution:

 Run glist to get a list of all stations and their spans

   glist scec.gdl scec.glist +1 scec.eq scec.apr

 The file `scec.glist` shows that there are 660 stations in the solution to be generated by the H-files in `scec.gdl`. To reduce the solution to only those stations that are useful, run the program *gen_uselist* with different criteria:

 For co-seismic displacements, use all stations with at least 2 epochs and a 0.1-yr span

   → `coseis.uselist` (285 stations)

For reliable velocities, use all stations with at least 3 epochs and a 3.0-yr span

→`vel.uselist` (69 stations)

Generate time series of long-term behavior, using a plate-scale stabilization

   rm globk_rep.org globk_rep.log

   glred 6 globk_rep.prt globk_rep.log scec.gdl globk_rep.cmd >! glred.out

   mv globk_rep.org globk_rep_noam.org

Check for good stabilization on each day:

   Grep 'Post RMS' globk_rep_noam.org | grep 'Iter 4' > rep_rms.noam

Each solution (aggregated h-file) should have least 5 stations in stabilization and rms < 5 mm.

Plot the time series:

   sh_plotcrd -f ../globk_rep_noam.org -s long -x 1992.0 2000.0 -order 1 -res -cols 1

Add downweights (sig_neu) to `scec_vel.reweight` for any outliers.

Perform a velocity solution:
   rm globk_vel.org globk_vel.log
   globk 6 globk_vel.prt globk_vel.log scec.gdl globk_vel.cmd >! globk.out
   mv globk_vel.org globk_vel_051028a.org

Check `globk_vel.org` (or `.log`) to make sure all chi2 increments are reasonable are in the range of 0.2-1.5. If some are higher, look for outliers in the time series and downweight individual stations (sig_neu) or the entire h-file (variance factor in scec.gdl). Check in `globk_vel.org` for a good total chi2 (1.25) and a good fit to the reference-frame-defining stations (velocity rms < 2 mm/yr).

Plot the velocities:

 sh_plotvel -ps 051028a -f globk_vel_051028a.org -maxsigma 2   -arrow_value 5 -maprange cal_landers

      See sh_map_elements for defining 'maprange'; or use
    sh_plotvel -ps 051028a -f globk_vel_051028a.org -maxsigma 5 -R-122/-114/31/37.5

Generate a new apr file with a self-consistent set of coordinates and velocities for all stations:

   grep 'Unc. ' globk_vel_051028a.org > ../tables/scec_noam.apr   (edit out the 'Unc.' in columns 1-4)

Repeat the generation of time series, this time using a regional stabilization. In `glorg_rep.cmd`, replace `itrf00_noam.apr` with `scec_noam.apr`, and `stab_site.noam` with `stab_site.calif`, where `stab_site.calif` includes all stations with well-determined positions and velocities. (this might be 3 mm in position for pre-Landers, < 8 mm for post-Landers; < 2 mm/yr in velocity).

   rm globk_rep.org globk_rep.log
   glred 6 globk_rep.prt globk_rep.log scec.gdl globk_rep.cmd >! glred.out
   mv globk_rep.org globk_rep_calif.org

Check for good stabilization on each day:

 grep 'Post RMS' globk_rep_calif.org | grep 'Iter 4' > rep_rms.calif

When we first ran these repeatabilities with regional stabilization, the surveys had 8-30 stations in stabilization and rms values 1-9 mm. Most of these were better than for the N-Amer stabilization, but the first 6 surveys after Landers (920708-931005) were significantly worse (3.4-8.2 mm). Examing the glorg print file revealed two obvious problems:

   1) We included in the stabilization stations that were affected by (non-linear) post-seismic motion. We anticipated this problem but included some stations in the hope that the 3-sigma cutoff criterion for the stabilization would force them to be removed in the stabilization iteration (it just barely failed to the outliers).

2) The (many) additional stations in the Landers region reduced the height-sigma mean enough that all but one of the distant (North American) stations were removed by the relative-height-sigma criterion (cnd_hgtv) for the iteration of the stabilization.

We fixed these two problems by removing (commenting out) more Landers-region stations from the stabilization and increasing the height ratio from 2.0 to 4.0. With these changes, the stabilization rms for the regional frame is only slightly worse than for the N-Amer frame (rep_rms.noam) in 1992.5-1993.8 and better everywhere else. It is useful at this point to generate time series with the regional stabilization and compare these with the N-American stabilization. It is also useful to perform the regional stabilization with and without rotation estimated in glorg. Including rotation provides more parameters to absorb orbital and EOP errors, but reduces the redundancy, possibly masking errors associated with stations that have a high weight ("lever arm") in the stabilization. The sensitivity of the time series to the spatial extent of the reference frame (stabilization network) and number of parameters estimated increases as the number of stations available for stabilization decreases.

Get the final velocities:

```
rm globk_vel.org globk_vel.log
globk 6 globk_vel.prt globk_vel.log scec.gdl globk_vel.cmd >! globk.out
mv globk_vel.log globk_vel_051028b.log
mv globk_vel.org globk_vel_051028b.org
```

(Use sh_plotvel again to get velocity field displayed.)

Repeat the glorg run (only) to get velocities in other frames. Do this by editing the glorg command file to change stab_site, apr_file, and/or plate. Add BLEN to the print options to get baselines for co-seismic displacements.

```
rm globk_vel.org
glorg globk_vel.org CMDS:PSUM:VSUM:GDLF glorg_vel.cmd  scec_vel.com
mv globk_vel.org globk_vel_051028c.org
```

Extract the co-seismic displacements:

```
sh_eq  -f globk_vel_051028c.org  -eq GLA
```

There are two files of co-seismic displacements, in different formats:

```
        eq_disp.globk_vel_021102c.org.out
        eq_disp.globk_vel_021102c.org.vel   (prt/org format, for input to sh_plotvel)
```

Error analysis and data weighting

From theoretical considerations and empirical evidence
- phase noise is elevation dependent and has temporal correlations of seconds to hours
- daily position estimates have temporal correlations of days to months
- position and velocity estimates have spatial correlations up to ~ 1000 km

therefore using random-noise statistics is almost never reasonable

Approaches to getting reliable statistics

Ideal: use a full and theoretically complete covariance matrix for the phase analysis and/or
quasi-observation analysis — not possible

Reasonable and often adequate approximation

- Use a post-processing analysis of the position repeatabilities and external
knowledge of the noise spectrum to assign the uncertainties on a station-by-
station and component-by-component basis.   Works only for long, continuous
time series.
  Utilities: sh_plotcrd / sh_tshist; ensum / enfit / sh_marcmd
  References: Langbein and Johnson [*J. Geophys. Res., 102*, 591, 1997]
  Zhang et al. [*J. Geophys. Res., 102*, 18035, 1997]
  Mao et al. [*J. Geophys. Res., 104*, 2797, 1999]
  Dixon et al. [*Tectonics , 19,* 1, 2000]
  Herring [*GPS Solutions, 7*, 194, 2003]
  Williams [*J. Geodesy, 76*, 483, 2003]
  Williams et al. [*J. Geophys. Res. 109*, B03412, 2004]

- Decimate and reweight the phase data and/or aggregate and reweight the position
estimates so that the assumed a priori error for (nearly) random samples gives a chi-square
of 0.5-1.0 ; include Markov noise (random walk) in the analysis.   Often only practical
approach for survey-mode observations.
   [McClusky et al., *J. Geophys. Res.*, 105, 5695, 2000; McCaffrey et al., 2006]

- Use an a posteriori analysis of velocity scatter with respect to an assumed model to assess the
reasonableness of the estimated uncertainties.
  Utility: sh_velhist
  References: McClusky et al., [*J. Geophys. Res.*, 105, 5695, 2000]
  Langbein and Johnson [*J. Geophys. Res., 102*, 591, 1997]
  McClusky et al. [*Geophys. Res. Lett. 28*, 3369, 2001]
  McCaffrey et al., [submitted to *Geophys. J. Int*., 2006].

Noise in GPS coordinate time series

Ailin Mao,[1] Christopher G. A. Harrison, and Timothy H. Dixon

Division of Marine Geology and Geophysics, Rosenstiel School of Marine and Atmospheric Sciences
University of Miami, Miami, Florida

Abstract. We assess the noise characteristics in time series of daily position estimates for 23 globally distributed Global Positioning System (GPS) stations with 3 years of data, using spectral analysis and Maximum Likelihood Estimation. A combination of white noise and flicker noise appears to be the best model for the noise characteristics of all three position components. Both white and flicker noise amplitudes are smallest in the north component and largest in the vertical component. The white noise part of the vertical component is higher for tropical stations (±23° latitude) compared to midlatitude stations. Velocity error in a GPS coordinate time series may be underestimated by factors of 5-11 if a pure white noise model is assumed.

1. Introduction

Geophysical studies using geodetic measurements of surface displacement or strain require not only accurate estimates of these parameters but also accurate error estimates. Geodetic measurements of displacement differ in two important ways from other types of geophysical data, and these differences complicate error estimation.

First, we generally require a long time series of measurements, often several years or more, in order to obtain accurate site velocity estimates. This means that a variety of errors with different timescales can corrupt the data. An individual error source may also change with time; for example, the instrument may improve. It is convenient to characterize errors as white (no time dependence) and colored (time-correlated). While the effect of white noise can be greatly reduced through frequent measurement and averaging, this is less useful for time-correlated noise and, in fact, provides no benefit at all for one type of time-correlated noise, the random walk.

Second, while we generally seek to infer the motion of large crustal units, what we actually measure is the motion of a mark or monument on or just below the ground surface. Spurious motion of the mark (monument noise) unrelated to motion of the larger crustal units of interest has been identified as an important noise source for many geodetic measurements [*Johnson and Agnew*, 1995; *Langbein et al.*, 1995]. Analysis of long (decade or more) time series of high-precision two-color electronic distance measurement (EDM) data from sites in California suggests that monument noise can be modeled as a random walk [*Langbein and Johnson*, 1997].

For geodetic data acquired with the Global Positioning System (GPS), a variety of time-correlated processes in addition to monument noise corrupt velocity estimates and, in fact, likely dominate the error budget at the present time. In other words, GPS velocity estimates may not yet be accurate enough to observe monument noise except in extreme cases. Other sources of time-correlated noise include mismodeled satellite orbits, other reference frame effects (e.g., Earth orientation), mismodeled atmospheric effects, and mismodeled antenna phase center effects, which may vary with satellite elevation, azimuth, and local environmental factors.

Studies of time-correlated noise in GPS time series have been hampered by the relatively short time that high-quality time series have been available. Rigorous analysis of time-correlated noise in GPS data may well require decade or longer time series, but high-precision results from continuously operating stations have been available only since about 1992 or 1993. The present study reports the noise characteristics of 23 globally distributed GPS sites that have operated more or less continuously for about 3 years.

2. Previous Work

Zhang et al. [1997] analyzed 1.6 years of essentially continuous daily measurements from 10 sites in southern California, and the reader is referred to that work for additional background on some of the issues discussed here. *Zhang et al.* [1997] were able to reduce regionally correlated noise (probably dominated by orbit errors) by use of a filtering algorithm that subtracted common mode, nontectonic signals from the GPS time series [*Wdowinski et al.*, 1997]. This method is applicable whenever data from a relatively dense network are available but is not yet possible for a globally distributed set of sites, because of their isolation. Noise in the residual time series studied by *Zhang et al.* [1997] was characterized as "fractal white" (spectral index 0.4, defined below) or a combination of white noise and flicker noise (spectral indices of 0 and 1, respectively). Given the shortness of the time series available to them, *Zhang et al.* [1997] could not distinguish between these models.

This study differs in three ways from that of *Zhang et al.* [1997]. First, we study a global distribution of sites (Figure 1), which allows us to assess regional differences in noise. This is important for the GPS, where orbit, reference frame, and atmospheric errors are likely to be important and may exhibit regional differences. Second, we have studied "raw" GPS coordinate time series, as opposed to data with orbit and reference frame errors reduced or eliminated through common mode techniques. Thus our results should be applicable to GPS coordinate time series from any site, no matter how isolated. Filtered data or relative position (baseline) data can be expected to be less noisy than results presented here, provided the baselines are short enough.

---

[1]Now at Magellan Systems Corporation, San Dimas, California.
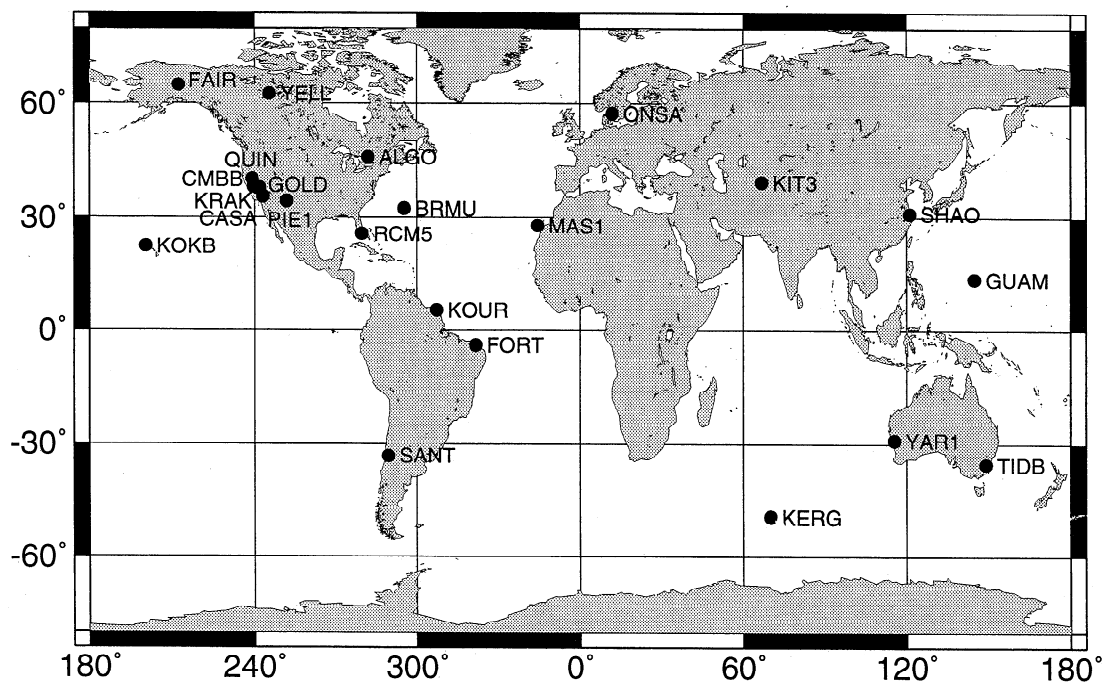
Figure 1. Distribution of Global Positioning System stations used in this study.

Third, longer time series (3.0 years, nearly a factor of 2 longer) are now available, enabling a more accurate assessment of long-period time-correlated noise.

3. Data Analysis

Since early 1994, GPS data from a number of continuously operating stations (currently 120) have been analyzed in the Geodesy Laboratory of the University of Miami to study various geophysical phenomena. We selected 23 stations with time spans longer than 2.5 years for noise analysis (Table 1, Figure 1). Seventeen stations have 3.0 years of data or more. The 1994 and later period used here is a convenient one. Many stations experienced frequent equipment changes prior to 1994. Also, these later data tend to be less noisy compared to earlier data, especially in the Southern Hemisphere, perhaps reflecting improvement in satellite ephemerides as the number of global tracking stations increased rapidly between 1991 and 1994.

To speed analysis, for most applications (and this analysis) we use satellite orbit and clock files provided by the Jet Propulsion Laboratory (JPL) [Zumberge et al., 1997]. The resulting daily station coordinates are transformed into global reference frame ITRF-94 [Boucher et al., 1996]. Analysis procedures are described by Dixon et al. [1997].

We use two methods, spectral analysis and Maximum Likelihood Estimation (MLE), to assess time-correlated noise in these time series. We use spectral analysis to estimate the spectral index of noise, while MLE is used to characterize the amplitudes of the stochastic processes with integer spectral indices.

3.1. Spectral Analysis

The power spectra, P, of many geophysical phenomena are well approximated by a power-law dependence on frequency f of the form [Agnew, 1992]

$$P(f) = P_0 f^{-\alpha} \qquad (1)$$

where α is the spectral index and P_0 is a constant. Larger α implies a more correlated process and more relative power at lower

frequencies. White noise has a spectral index of 0, flicker noise has a spectral index of 1, and a random walk has a spectral index of 2.

Spectral indices need not be limited to integer values. Geophysical phenomena and noise with fractional spectral indices in the range $1<\alpha<3$ are termed "fractal random walk," while indices in the range $-1<\alpha<1$ are termed "fractal white noise" [Agnew, 1992]. Noise processes with $-1<\alpha<1$ are stationary, while processes with spectral index larger than 1 are nonstationary. A stationary random process is one whose statistical properties (e.g., mean and variance) are invariant in time.

Following Langbein and Johnson [1997], the spectrum of a set of measurements can be modeled as the sum of white noise and colored noise:

$$P(f) = P_0 \left(f^{-\alpha} + f_0^{-\alpha} \right) \qquad (2)$$

where f_0 is the crossover frequency of the power spectrum defined as the point at which the two processes have the same power levels. The constants α, P_0, and f_0 can be estimated by fitting a curve to the power spectrum of a time series. The uncertainties are determined by seeing how well the model fits the spectrum using standard least squares. We have used an iterative nonlinear least squares method to estimate these parameters. In order to speed convergence, we apply the natural logarithm to both sides of (2):

$$\ln P(f) = \ln P_0 + \ln(f^{-\alpha} + f_0^{-\alpha}) \qquad (3)$$

The differential form of this equation can be written

$$d\{\ln[P(f)]\} = d\ln(P_0) - \frac{\alpha f_0^{-\alpha-1}}{f^{-\alpha} + f_0^{-\alpha}} df_0$$

$$+ \frac{f^{-\alpha} \ln f + f_0^{-\alpha} \ln f_0}{f^{-\alpha} - f_0^{-\alpha}} d\alpha \qquad (4)$$

Using the relationship between parameters and measurements given in (4), we can form a set of observation equations, $\mathbf{AX} = \mathbf{V}$,

Table 1. Station Description (Post-1994)

ID	Station Name	Lat, deg	Long, deg	H,[a] m	Receiver[b]	Antenna[c]
ALGO	Algonquin	45.96	-78.07	202	TR	TR
BRMU	Bermuda	32.37	-64.70	-8	TR	TR
CASA	Mammoth Lakes	37.64	-118.10	2390	TR	TR; add antenna skirt (1)
CMBB	Columbia	38.03	-120.39	695	Ashtech Z-12	Ashtech; TR (2)
FAIR	Gilmore Creek	64.98	-147.50	319	ROGUE; TR(3)	ROGUE; TR(3)
FORT	Fortaleza	-3.88	-38.42	20	TR	TR
GOLD	Goldstone	35.42	-116.89	987	ROGUE	ROGUE; TR (4)
GUAM	Guam	13.59	144.87	202	TR	TR
KERG	Kerguelen Island	-49.35	70.26	74	ROGUE	TR
KIT3	Kitab	39.14	66.88	643	TR	TR
KOKB	Kokee Park	22.13	-159.66	1167	ROGUE; TR(5)	ROGUE; TR(5)
KOUR	Kourou	5.25	-52.81	-25	ROGUE	ROGUE
KRAK	Krakatua	37.71	-118.88	2359	TR	TR
MAS1	Maspalomas	27.76	-15.63	197	TR	TR
ONSA	Onsala	57.40	11.92	46	TR	ROGUE
PIE1	Pietown	34.30	-108.12	2347	TR	TR
QUIN	Quincy	39.97	-120.94	1106	TR	TR
RCM5	Richmond	25.61	-80.38	-25	TR	TR
SANT	Santiago	-33.15	-70.67	723	ROGUE; TR(6)	ROGUE; TR(6)
SHAO	Shanghai	31.10	121.20	22	TR	TR
TIDB	Tidbinbilla	-35.40	148.98	665	ROGUE	ROGUE; TR(7)
YAR1	Yaragadee	-29.05	115.35	241	ROGUE	ROGUE
YELL	Yellowknife	62.48	-114.48	181	TR	TR

[a]Height above ellipsoid.

[b]Receiver: ROGUE, ROGUE SNR-8; TR, ROGUE SNR-8000 or SNR-8100. Numbers in parentheses are equipment change dates: (1) June 3, 1995; (2) Aug. 20, 1997; (3) April 16, 1996; (4) Oct. 31, 1995; (5) Jan. 10, 1996; (6) July 17, 1996; (7) June 26, 1996.

[c]Antenna: ROGUE, DORNE MARGOLIN R; TR, DORNE MARGOLIN T; Ashtech, Ashtech GEODETIC L1/L2 P. Numbers in parentheses are equipment change dates (see previous note).

where A is a function of P_0, f_0 and α, $\mathbf{X} = [d\ln(P_0), df_0, d\alpha]^T$ is the update vector for parameters, and $\mathbf{V}$ is the difference between the observed and the computed power spectra. A normal equation can be created based on least-squares in the form

$$\mathbf{N}\mathbf{X} = \mathbf{L} \qquad (5)$$

where the normal matrix $\mathbf{N} = \mathbf{A}^T\mathbf{A} = [n_{ij}]$ and vector $\mathbf{L} = \mathbf{A}^T\mathbf{V} = [l_i]$. The Levenberg-Marquardt method [*Press et al.*, 1992] is used to solve the nonlinear parameter estimation. The normal matrix here gives only the trend at a particular point, but not how far that slope extends. We can replace the normal matrix $\mathbf{N}$ in (5) with a new matrix $\mathbf{N}' = [n'_{ij}]$ defined by the following rules:

$$n'_{ij} = \begin{cases} n_{ij}(1 + \lambda) & i = j \\ n_{ij} & i \neq j \end{cases} \qquad (6)$$

When λ is very large, the matrix $\mathbf{N}'$ is forced to be nearly diagonal, and the step size by which the solution is approached is reduced because the diagonal elements of the normal matrix are

enlarged. On the other hand, as λ approaches zero, $\mathbf{N}'$ will be close to the real normal matrix $\mathbf{N}$.

Given an initial guess for the set of fitted parameters $\mathbf{X}$, we use the following iterative steps modified from the Levenberg-Marquardt method:

1. Pick a modest value for λ, say $\lambda = 0.001$.
2. Compute normal matrix $\mathbf{N}$, $\mathbf{L}$ and misfit $\chi^2(X)$.
3. Modify the normal matrix as in (6) and solve the modified normal equation (5) for δX and evaluate $\chi^2(X + \delta X)$.
4. If $\chi^2(X + \delta X) \geq \chi^2 X$, increase λ by a factor of 10 and go back to step 3.
5. If $\chi^2(X + \delta X) < \chi^2 X$, update the trial solution with $X + \delta X$, decrease λ by a factor of 10, and go back to step 2.
6. The iteration can be stopped when $\chi^2(X + \delta X)$ decreases by a negligible amount for $\lambda \leq 0.01$.

For example, when $\alpha = 1$, (2) approaches P_0/f at low frequencies, which corresponds to flicker noise, and approaches a constant P_0/f_0 at high frequencies, which corresponds to white noise. The amplitudes of white noise and flicker noise components can be calculated from estimated values of P_0 and f_0, and similarly

for the case of random walk noise ($\alpha=2$) or arbitrary α. Noise components derived in this way are less precise than those derived with the MLE techniques described later, although they can provide an independent estimate for comparison purposes.

In our case, α and P_0 vary by less than 10, while f_0 is much more variable and may cause convergence problems, especially if it is close to zero (white noise dominates over time-correlated noise). In case of divergence, a straight line can be fitted to the spectrum to estimate the spectral index, although this may underestimate the spectral index at low frequency for time series composed of white noise plus time-correlated noise. Again, reference to MLE allows an independent estimate.

Time series are windowed prior to spectral analysis. The simplest window is a boxcar window, in which the finite data set is left alone. Specialized windows can be used to reduce spectral leakage and sidelobe effects [*Press et al.*, 1992], but can sometimes artificially enhance the power at low frequencies, which is undesirable for our application. Boxcar windows were used for most of the results presented here. To verify the stability of our spectral estimates, we also analyzed the time series using several other common windowing techniques. In general, these gave similar results to the boxcar window results, as described below (section 4.1.).

Two techniques (Fourier spectrum and least squares) can be used to estimate the periodogram of a time series, depending on whether the data are evenly spaced or not. For a series of N discrete observations x_j, ($j = 1, N$) at equal spacing, the power spectrum by means of a periodogram is defined from the discrete Fourier transform as [*Scargle*, 1982]

$$P(f_n) = \frac{1}{N}\left[\left(\sum_{j=1}^{N} x_j \cos 2\pi j f_n\right)^2 + \left(\sum_{j=1}^{N} x_j \sin 2\pi j f_n\right)^2\right] \quad (7)$$

where $f_n = n/T$, T is the fundamental period, and $n = 1, ..., N/2$. If x_j is pure white noise, $P(f_n)$ is an exponentially distributed random variable with an expectation value equal to the variance of the white noise. The amplitude estimates of the spectrum at the frequencies f_n are independent.

In many situations (including many of our GPS time series), evenly spaced data cannot be obtained. There are ways to modify unevenly spaced time series to simulate evenly spaced ones. Interpolation is one approach, but most interpolation techniques perform poorly for large gaps [*Press et al.*, 1992], a problem at some of the GPS sites. We follow the approach of *Lomb* [1976], who used a nonlinear least squares technique to estimate spectra by fitting sine waves directly to the data. Given a set of N observations x_j with zero mean at t_j ($j = 1$ to N), we can set up the following model at a given frequency f:

$$x_j + \varepsilon_j = a \cos 2\pi(t_j - \tau)f + b \sin 2\pi(t_j - \tau)f \quad (8)$$

where the errors ε_j are independent and have zero mean and common variance, a and b are unknowns, and τ is introduced for simplification, defined by

$$\tan(4\pi f \tau) = \sum_{j=1}^{N} \sin 4\pi t_j f \bigg/ \sum_{j=1}^{N} \cos 4\pi t_j f \quad (9)$$

Then the periodogram can be derived as follows:

$$P(f) = \frac{1}{2}\left\{\frac{\left[\sum_{j=1}^{N} x_j \cos 2\pi(t_j - r)f\right]^2}{\sum_{j=1}^{N} \cos^2 2\pi(t_j - \tau)f} + \frac{\left[\sum_{j=1}^{N} x_j \cos 2\pi(t_j - r)f\right]^2}{\sum_{j=1}^{N} \sin^2 2\pi(t_j - \tau)f}\right\} \quad (10)$$

Scargle [1982] proved that the resulting periodogram has exactly the same exponential probability distribution as for evenly spaced data. Windowing techniques can also be applied. While this expression can be evaluated at any frequency, it is typically evaluated only at a set of evenly spaced frequencies similar to the Fourier spectrum, defined by

$$f_n = n/T \qquad n = 1, 2, ... \quad (11)$$

where T is the fundamental period. However, the orthogonality of the periodogram at these frequencies is lost for unevenly spaced data. It can be shown by numerical test or derivation that the Fourier spectrum and least squares method are equivalent when both are applied on the same evenly spaced data [*Scargle*, 1982].

To verify the performance of the least squares algorithm in the presence of data gaps, we tested it with two kinds of missing data: small amounts of missing data randomly distributed through the time series, and a single large gap. For the first test we randomly removed 30% of the data from an evenly spaced time series and found that there is essentially no bias in the resulting spectral profile, compared with the spectrum estimated from the original time series (Figure 2).

To test the effect of large gaps in the data, we generated 20 synthetic time series of 1000 points each, with noise characteristics similar to our GPS time series (spectral indices 0.80-1.60), removing 10, 20, and 30% of the data from each time series near the beginning (100 points in) to simulate a large gap. Effects on the estimated spectral indices for individual time series were always less than 0.4: +0.24 to -0.20 for 10% data removal; and +0.27 to -0.39 for 20% data removal; +0.37 to -0.34 for 30% data removal. Effects on the mean spectral index were negligible: +0.002 for 10% data removal; -0.06 for 20% data removal; and +0.01 for 30% data removal. We conclude that our technique for estimation of the spectral indices of time series is robust in the presence of data gaps.

For relatively short time series the spectral index can be underestimated. We have investigated our sensitivity to this effect in two ways. First, the nonlinear least squares estimation method was tested on theoretical power-law spectra with different lowest frequency. Spectral indices of 2 and 1 were tested. Nonlinear least squares can estimate the spectral index reliably when the length of the time series is 1.8 times the crossover period for both index values.

We further tested both the Fourier method and least squares method on mixed noise synthetic time series, mixing white noise
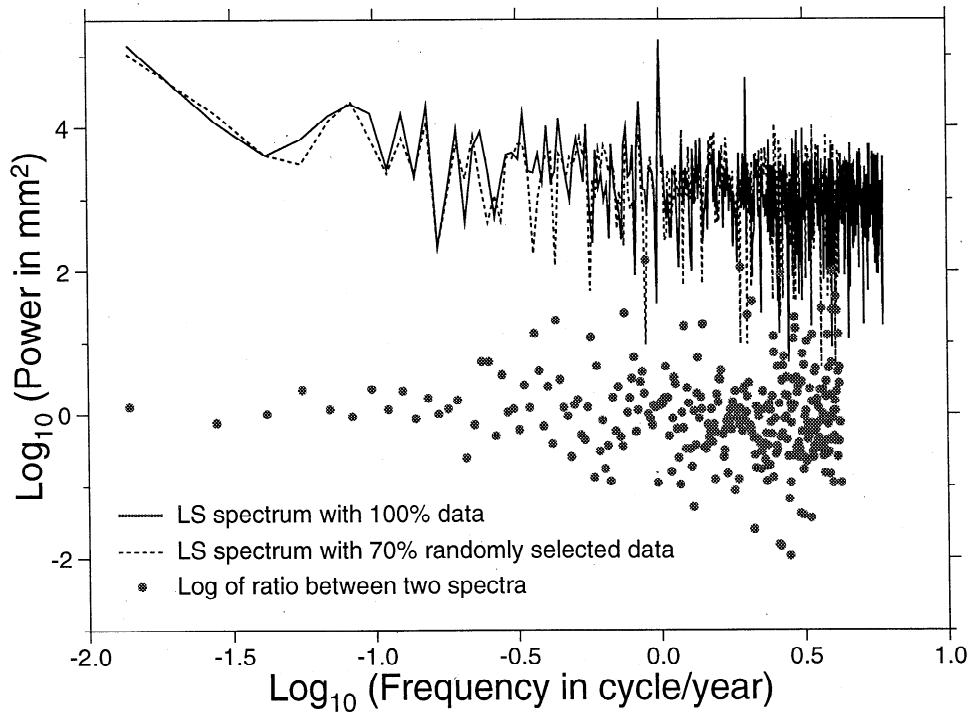
Figure 2. Power spectrum computed from complete time series (solid line) compared with spectrum computed with 30% of data randomly removed. Data are 73 years of monthly mean tide gauge data from Boston. An annual and semiannual term stand out above the noise. Frequency is in cycles per year.

with either flicker noise or random walk noise, with similar amplitudes to current GPS time series (Table 2). In test case one, time series were simulated with 4.0 mm of white noise and 5.0 mm of flicker noise, and 30% of the points randomly removed. The crossover period of these time series is about 20 days. We found that the spectral indices can be estimated reliably for time series longer than 2 years, a criterion we meet for all our time series. Although the mean estimation is not biased for time series equal to 1 year, many solutions failed to converge. We also found that it is more difficult to estimate the spectral index when we removed the annual term. In test case two we simulated GPS time series with 4.5 mm of white noise and 1.5 mm/√yr of random walk noise, whose crossover period is about 1 year. The length of data required to characterize accurately the random walk component is usually taken to be 5 times the crossover period ($5/f_0$), in this case 5 years. However, in this simulation, even 5 years was inadequate. Periodic signals and other noise make it more difficult to detect random walk noise, implying that it will be some time before GPS time series can be analyzed for accurate estimates of random walk noise, at least for data similar to the coordinate time series discussed here. For more precise baseline (relative position) data, random walk noise may be characterized in less time, depending on its amplitude (e.g., Dixon et al., 1997). Spectral index results are summarized in Table 3.

3.2. Maximum Likelihood Estimation

Assuming the observed time series $\mathbf{X} = \{ x_j, t_j \ (j=1, N) \}$ is composed of only white noise with variance σ_w^2, flicker noise with variance σ_f^2 (its scale will be defined later), and random-walk noise σ_{rw}^2 (variance over specific time, e.g., 1 year), the covariance matrix of observations can be written as

$$\mathbf{Q_{xx}} = \sigma_w^2 \mathbf{I} + \sigma_{rw}^2 \mathbf{R_{rw}} + \sigma_f^2 \mathbf{R_f} \qquad (12)$$

where $\mathbf{I}$ is the $N \times N$ identity matrix, and $\mathbf{R_{rw}}$ and $\mathbf{R_f}$ are the matrices representing the covariance of random walk noise and flicker noise, respectively.

A random walk process is derived by integrating white noise. As we do not have any information about the random walk process before the observations start, we assume that random walk noise at time t_0 is equal to zero. With this assumption the observed time series over a fixed time T is stationary (even though the process itself is not) and easily characterized statistically [Brockwell and Davis, 1996]. The matrix $\mathbf{R_{rw}}$ can be expressed as the following equation [Johnson and Wyatt, 1994]:

$$\mathbf{R_{rw}} = \begin{pmatrix} \Delta t_1 & \Delta t_1 & \cdots & \Delta t_1 \\ \Delta t_1 & \Delta t_2 & \cdots & \Delta t_2 \\ \vdots & \vdots & \ddots & \vdots \\ \Delta t_1 & \Delta t_2 & \cdots & \Delta t_n \end{pmatrix} \qquad (13)$$

where $\Delta t_j = t_j - t_0$.

For flicker noise ($\alpha = 1$) the elements of matrix $\mathbf{R_f}$ can be approximated by [Zhang et al., 1997]

$$r_{ij} = \begin{cases} \left(\dfrac{3}{4}\right)^2 \times 2 & t_i = t_j \\[2ex] \left(\dfrac{3}{4}\right)^2 \times \left(2 - \dfrac{\log|t_i - t_j|/\log 2 + 2}{12}\right) & t_i \neq t_j \end{cases} \qquad (14)$$

for most space geodetic time series ($|t_i - t_j| \ll 2^{22}$). The first several elements look like

Table 2. Test Results of Spectral Analysis on Synthetic Time Series

	Length of Time Series					
	1 year	2 years	3 years	5 years	8 years	15 years
Test Case One: White Plus Flicker Noise						
Mean ± standard deviation	1.22±0.50	1.12±0.40	1.15±0.32	1.08±0.25	1.07±0.15	1.10±0.11
Converged solutions	29	40	40	40	40	40
Test Case One With Annual Term Removed						
Mean ± standard deviation	0.77±0.27	0.67±0.25	0.82±0.31	0.83±0.17	0.92±0.17	1.02±0.00
Converged solutions	15	31	36	40	40	40
Test Case Two: White Noise Plus Random Walk Noise						
Mean ± standard deviation	0.91±0.63	1.42±1.23	1.81±1.41	1.48±0.63	1.68±0.62	1.99±0.42
Converged solutions	9	16	30	34	40	40
Test Case Two With Annual Term Removed						
Mean ± standard deviation	-	0.13±0.11	1.55±2.09	1.52±1.22	2.20±1.02	2.30±0.52
Converged solutions	0	3	6	13	29	39

A total of 40 simulations are tested for each solution. In test case one, time series are simulated with 4.0 mm of white noise and 5.0 mm of flicker noise; 30% of the points are randomly taken away. The crossover period of such a time series is about 19 days. In test case two we simulate GPS time series with 4.5 mm of white noise and 1.5mm/√yr of random walk noise, whose crossover period is about 1 year.

$$
\mathbf{R_f} = \begin{pmatrix} 1.125 & 1.031 & 0.984 & \cdots \\ 1.031 & 1.125 & 1.031 & \cdots \\ 0.984 & 1.031 & 1.125 & \cdots \\ \vdots & \vdots & \vdots & \ddots \end{pmatrix} \quad (15)
$$

The constants in (14) are chosen such that flicker noise and random walk noise, with equal variance and a sampling interval of 1 day, have equivalent power levels over a period of 1 year. The scale of flicker noise is also defined by (14).

The σ_w, σ_{rw}, and σ_f can be estimated by finding those values that maximize the following likelihood function, which is the joint probability of the data set [*Langbein and Johnson*, 1997]:

$$
L(\mathbf{X}, \sigma_w, \sigma_{rw}, \sigma_f) = (2\pi)^{-N/2} |\mathbf{Q_{XX}}|^{-1/2} \exp\left(-\frac{1}{2} \mathbf{X} \mathbf{Q_{XX}^{-1}} \mathbf{X}\right) \quad (16)
$$

Applying natural logarithms to both sides, we obtain

$$
\ln L(\mathbf{X}, \sigma_w, \sigma_{rw}, \sigma_f) = -\frac{N}{2} \ln(2\pi) - \frac{1}{2} \ln|\mathbf{Q_{XX}}| - \frac{1}{2} \mathbf{X} \mathbf{Q_{XX}^{-1}} \mathbf{X} \quad (17)
$$

For most available time series, only one of σ_{rw} and σ_f can be estimated along with σ_w. We can use the preceding spectral analysis as a guide to an appropriate noise model. Alternately, we can use MLE to test several noise models (e.g., white plus flicker, white plus random walk), and choose the optimum model on the basis of the maximum likelihood value [*Langbein and Johnson*, 1997; *Zhang et al.*, 1997]. We used both approaches. The maximum likelihood problem can be solved in several ways [e.g., *Koch*, 1986; *Press et al.*, 1992]. We selected the downhill simplex method developed by Nelder and Mead [*Press et al.*, 1992]. The method requires only function evaluations, not derivatives, although it is not very efficient in terms of the number of function evaluations required. The algorithm starts with an

initial guess of an N vector of independent parameters, then moves down through the complexity of an N-dimensional topography until reaching a minimum. Each step, called a reflection, moves the point of the simplex, where the function is largest or highest, through the opposite face of the simplex to a lower point.

Langbein and Johnson [1997] tested the MLE technique described here with synthetic time series with known amounts of white and random walk noise and showed that MLE recovers reasonable estimates of the magnitude of white and random walk noise and uncertainties. With slight modification their algorithm can also recover flicker noise magnitude and uncertainty. Table 4 shows the results of simulations for 10 time series, each with 5 mm of white noise and 5 mm of flicker noise. It is clear that the algorithm is able to recover reasonable estimates of white and flicker noise as well as reasonable uncertainty estimates.

4. Results and Discussion

4.1. Spectral Index and Noise Amplitude

The GPS position time series for all three components of the 23 stations are illustrated in Figure 3. Time series were detrended before spectral analysis and Maximum Likelihood Estimation. Data points with residuals larger than 3 times the standard error are treated as outliers and removed in the linear regression. Figure 4 shows the power spectra of the same time series. Most of the spectra can be described as white (constant power) at short periods (high frequency), and red (more power) at longer periods (low frequency) (e.g., ALGO east). Most of the spectra are white for periods shorter than about 15-30 days (Figure 4). However, a few of the spectra can equally well be described as "fractal white" with power rising uniformly on these log-log plots toward higher values at longer periods (e.g., CMBB east). The best fitting white plus colored noise spectrum is shown on each plot if convergence was achieved. The value of

Table 3. Station Time Series: Length and Spectral Index Estimates

ID	Span, years	Points	North,[1] α	East,[1] α	Vertical,[1] α
ALGO	3.4	864	1.38±0.56	1.63±0.70	0.69±0.21
BRMU	3.6	803	-	1.66±0.50	2.17±0.80
CASA	3.4	801	1.22±0.56	0.70±0.19	0.87±0.48
CMBB	3.3	498	0.71±0.55	-	1.17±0.43
FAIR	3.4	381	0.54±0.38	-	1.10±0.81
FORT	3.8	589	0.93±0.45	0.95±0.62	0.61±0.55
GOLD	3.6	487	-	1.06±0.45	1.06±0.54
GUAM	2.8	681	-	-	-
KERG	2.6	762	0.91±0.18	1.04±0.57	1.91±1.50
KIT3	2.7	620	0.86±0.20	0.79±0.47	1.03±0.46
KOKB	3.4	824	1.30±0.56	0.53±0.22	1.39±0.41
KOUR	3.6	627	-	0.75±0.42	0.74±0.32
KRAK	2.9	627	1.13±0.23	0.51±0.34	0.83±0.28
MAS1	3.0	581	1.47±0.62	0.55±0.31	1.04±0.25
ONSA	3.2	524	1.14±0.40	0.91±0.32	1.13±0.45
PIE1	3.6	606	-	0.75±0.40	1.24±0.59
QUIN	3.4	818	1.47±0.66	1.23±0.44	0.83±0.42
RCM5	2.7	554	-	0.52±0.59	1.34±0.64
SANT	3.6	568	0.56±0.48	0.61±0.42	1.56±0.73
SHAO	2.8	764	0.81±0.44	-	1.49±0.63
TIDB	3.4	853	1.41±0.50	0.74±0.43	1.15±0.47
YAR1	3.4	833	-	0.64±0.35	0.63±0.67
YELL	3.4	538	-	0.68±0.28	0.93±0.64
Weighted mean[2]			0.97±0.24	0.74±0.26	0.97±0.29

[1]No entry indicates failure to converge.

[2] Uncertainty is weighted rms scatter about weighted mean.

Table 4. Results of Tests of MLE Algorithm on Synthetic Time Series Containing 5 mm of White Noise and 5 mm of Flicker Noise

Run	White Noise, mm	Flicker Noise, mm
1	5.03±.22	5.69±.69
2	5.10±.20	4.47±.52
3	4.97±.21	5.27±.76
4	5.32±.22	4.37±.85
5	5.05±.20	3.68±.47
6	4.99±.20	4.32±.76
7	5.05±.22	5.72±.79
8	5.21±.21	3.98±.66
9	5.26±.22	4.97±.64
10	4.85±.22	6.17±.63

Uncertainties are 1 standard error. MLE, Maximum Likelihood Estimation.

the spectral index, α, and its standard error are also shown. Table 3 shows the spectral index estimates for the north, east, and vertical components. The spectral indices range from 0.51 to 2.17. By individual components, the weighted means are 0.97±0.24 (north), 0.74±0.26 (east), and 0.97±0.29 (vertical). Thus there is no significant difference in the spectral character of noise for north, east and vertical components. The weighted mean for all three components is 0.89±0.28, and the unweighted mean of all components is 1.02±0.37. The most reliable estimates for spectral index (uncertainty less than or equal to 0.50) lie in the range of 0.51 - 1.66. Since the mean spectral index is close to 1.0 regardless of component or weighting, we suggest that flicker noise is an adequate model for time-correlated noise in these time series. However, we cannot preclude the possibility that $\alpha < 1.0$ or $\alpha > 1.0$ (fractal white noise or fractal random walk noise), given the uncertainties.

To check the reliability of our spectral index estimates, we calculated the indices in several different ways. The mean values quoted above are based on nonwindowed data, with no value
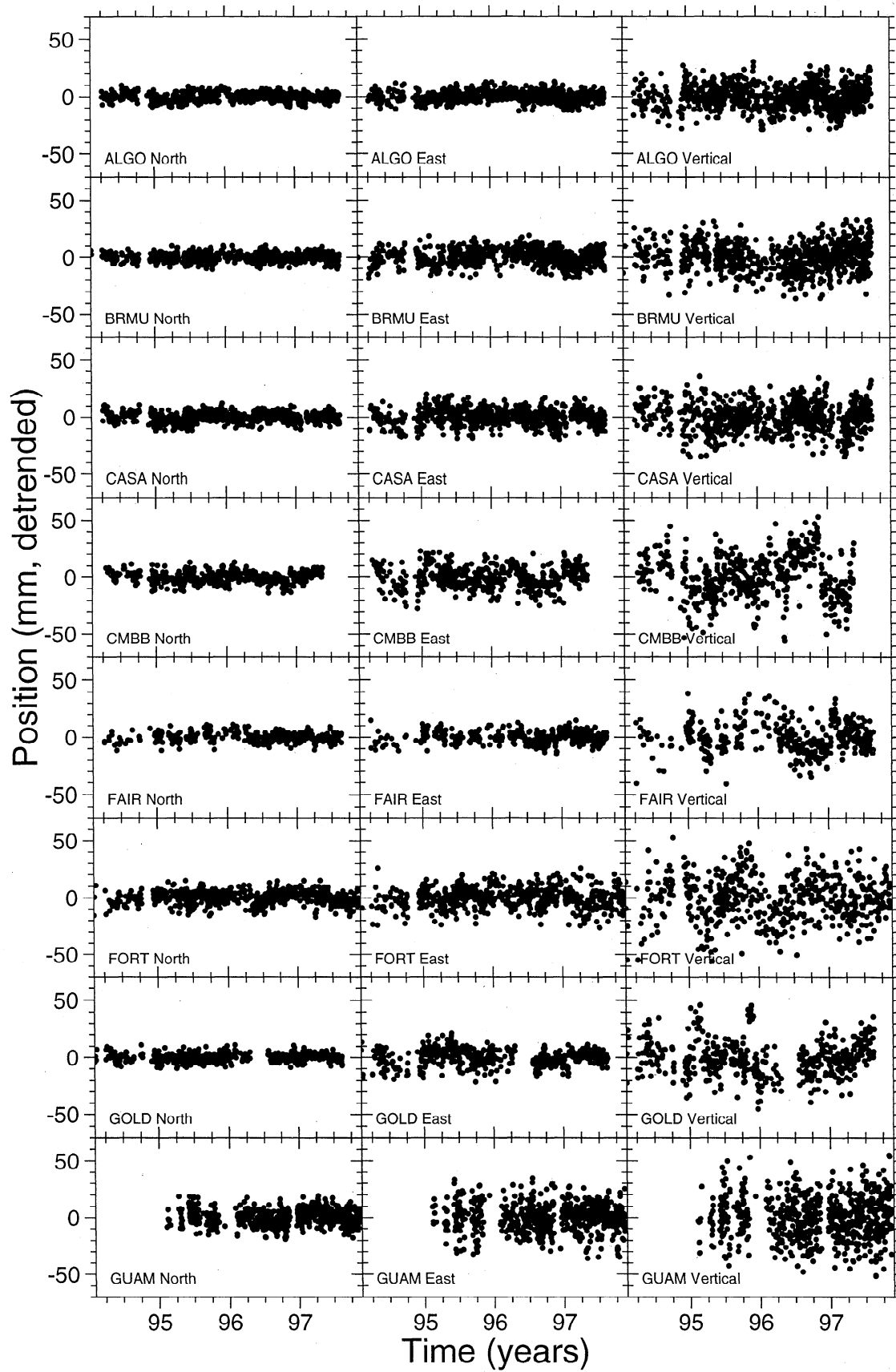
Figure 3. PS coordinate time series used in this study. Horizontal axes are for the years of about 1994-1998. Vertical axes are north, east, and vertical components in mm, offset by a nominal value.
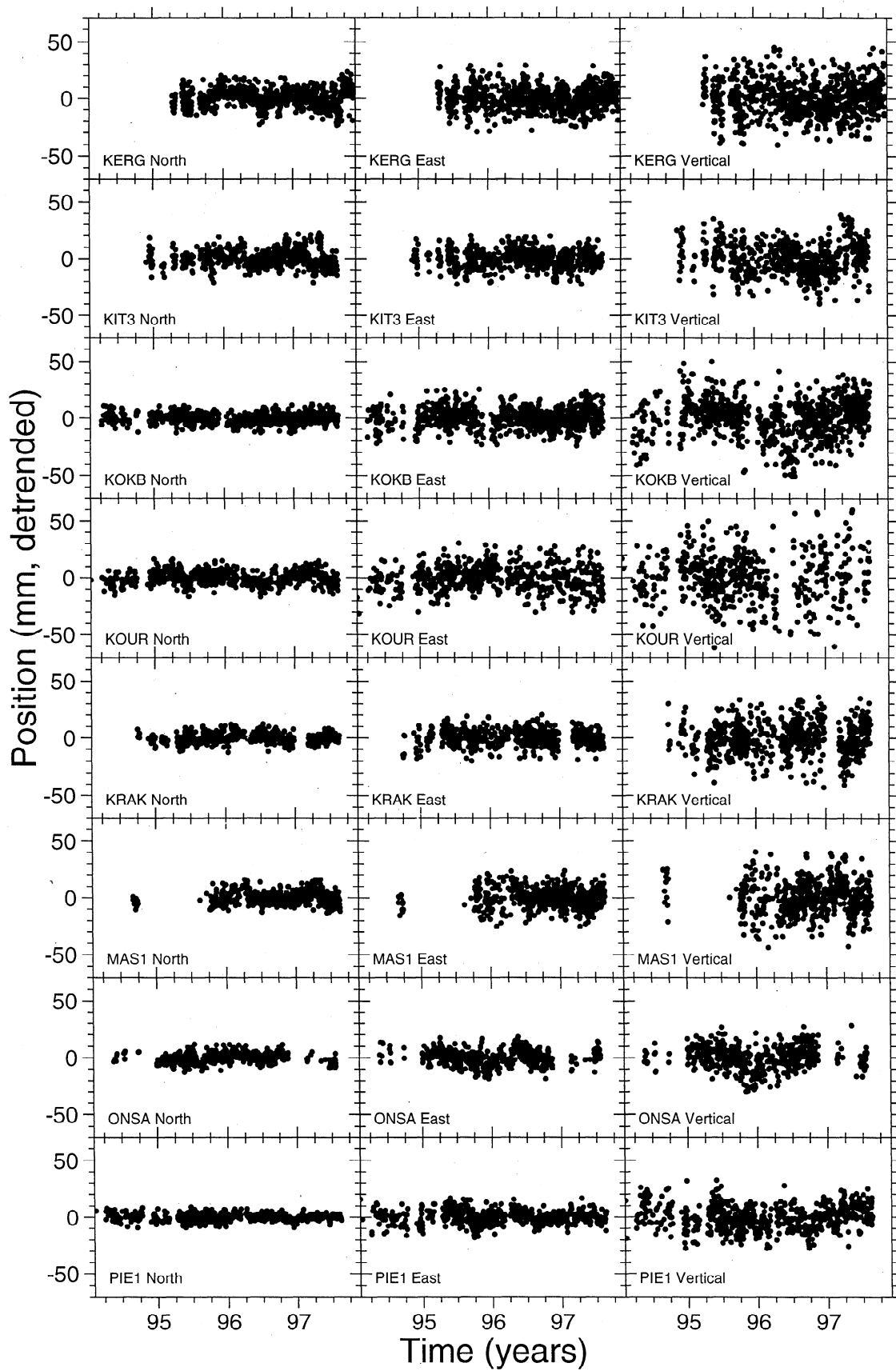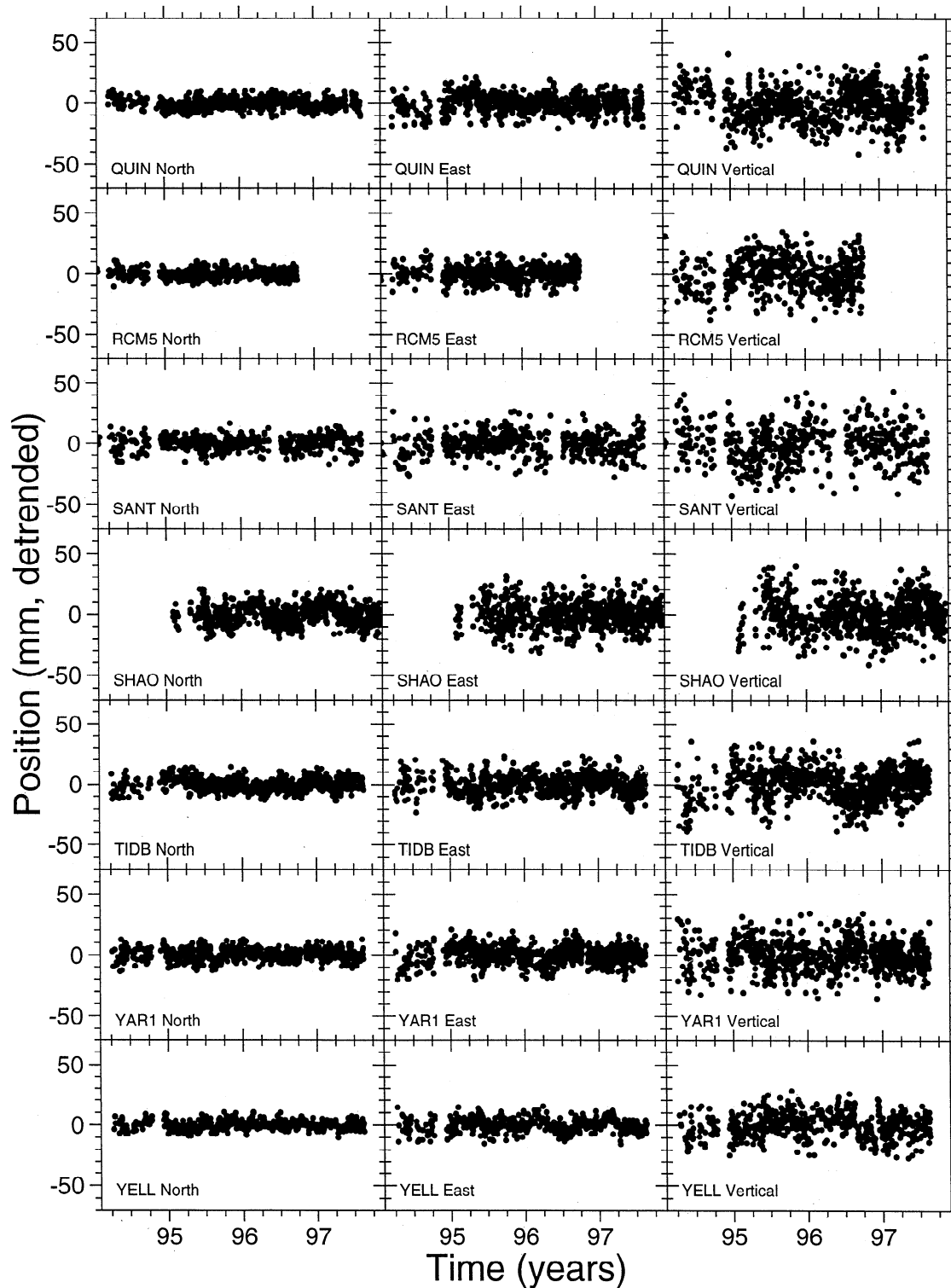
Figure 3. (continued)

Position (mm, detrended)

Time (years)

KERG North KERG East KERG Vertical
KIT3 North KIT3 East KIT3 Vertical
KOKB North KOKB East KOKB Vertical
KOUR North KOUR East KOUR Vertical
KRAK North KRAK East KRAK Vertical
MAS1 North MAS1 East MAS1 Vertical
ONSA North ONSA East ONSA Vertical
PIE1 North PIE1 East PIE1 Vertical

Figure 3. (continued)

computed for time series that failed to converge (13 out of 69 estimates; Table 3). It is possible to approximate the spectra for these divergent series by fitting a straight line. Employing this approach, again with non-windowed data, yields a mean spectral index of 0.98±0.42. We also computed spectra using several windowing techniques [*Press et al.*, 1992]. Use of the Hanning

window gives a mean spectral index of 0.95±0.46, while use of the Welch window gives 0.90±0.41.

We tested solutions with and without an annual term removed. For most solutions the results are equivalent within errors. However, when the annual term is removed, a larger number of solutions failed to converge. For the spectral index results discussed
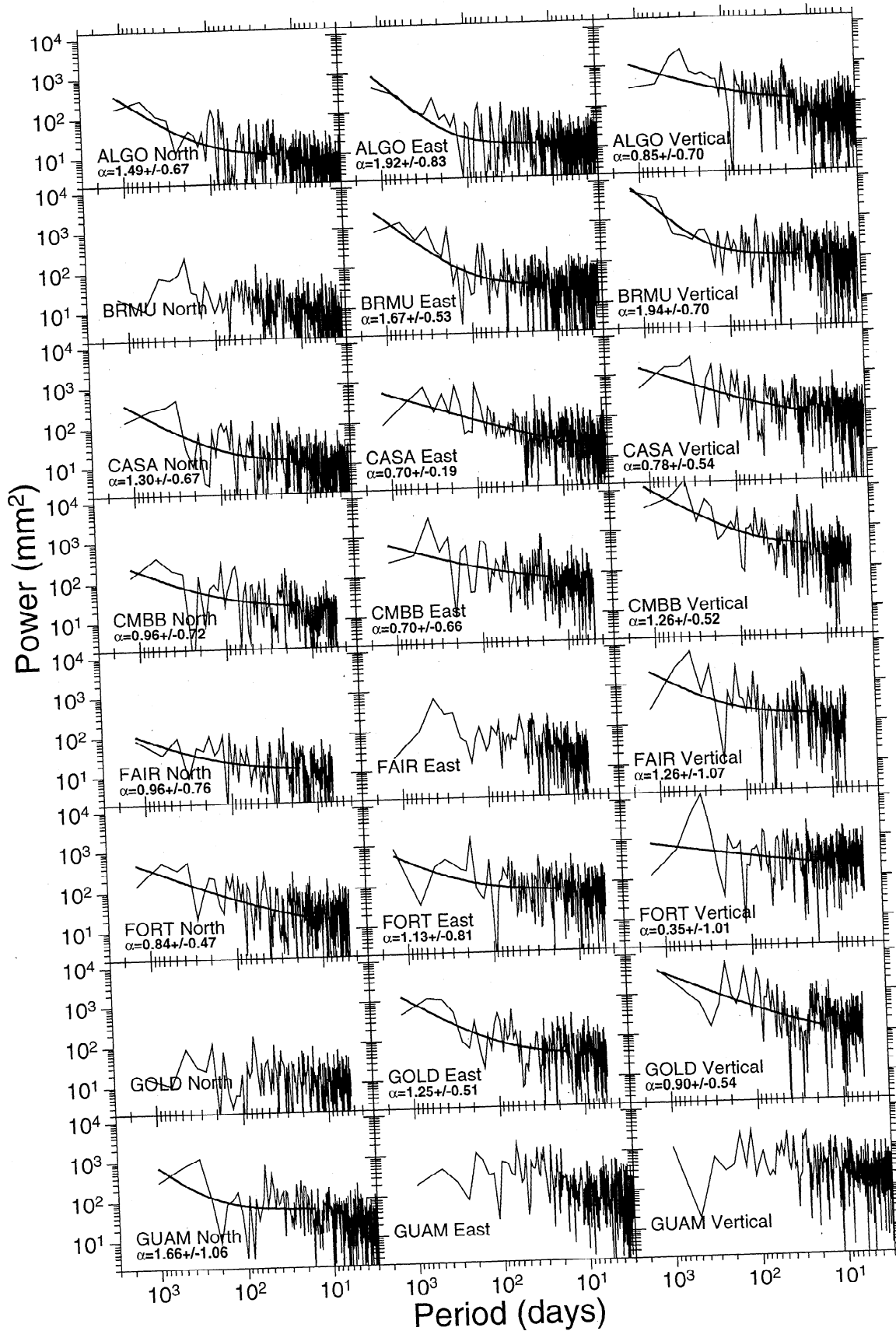
Figure 4. Power spectra of GPS time series shown in Figure 3. Here α is estimated spectral index. Horizontal axes are period in days. Vertical axes are power in mm². Missing values indicate failure to converge.
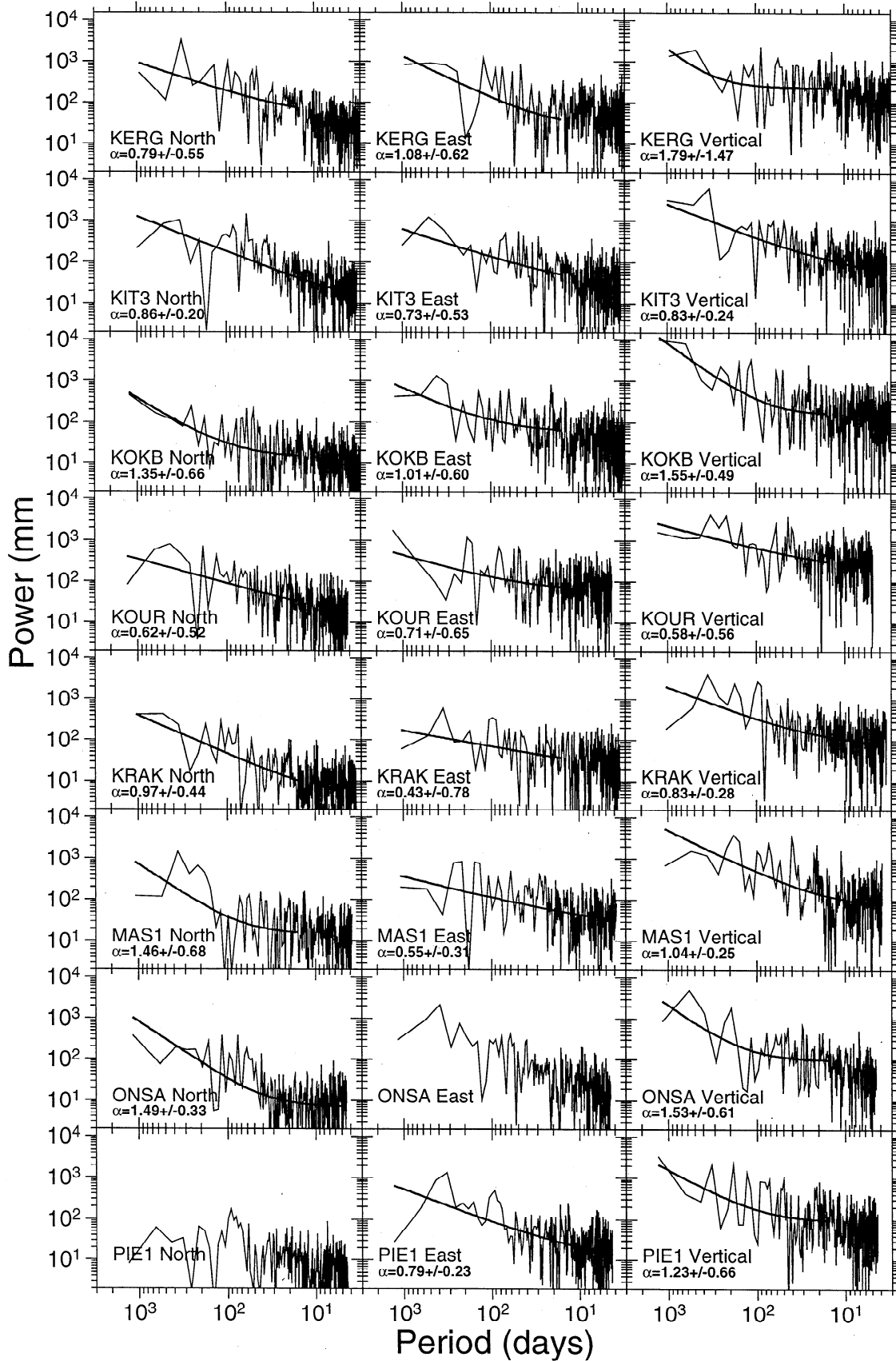
Figure 4. (continued)
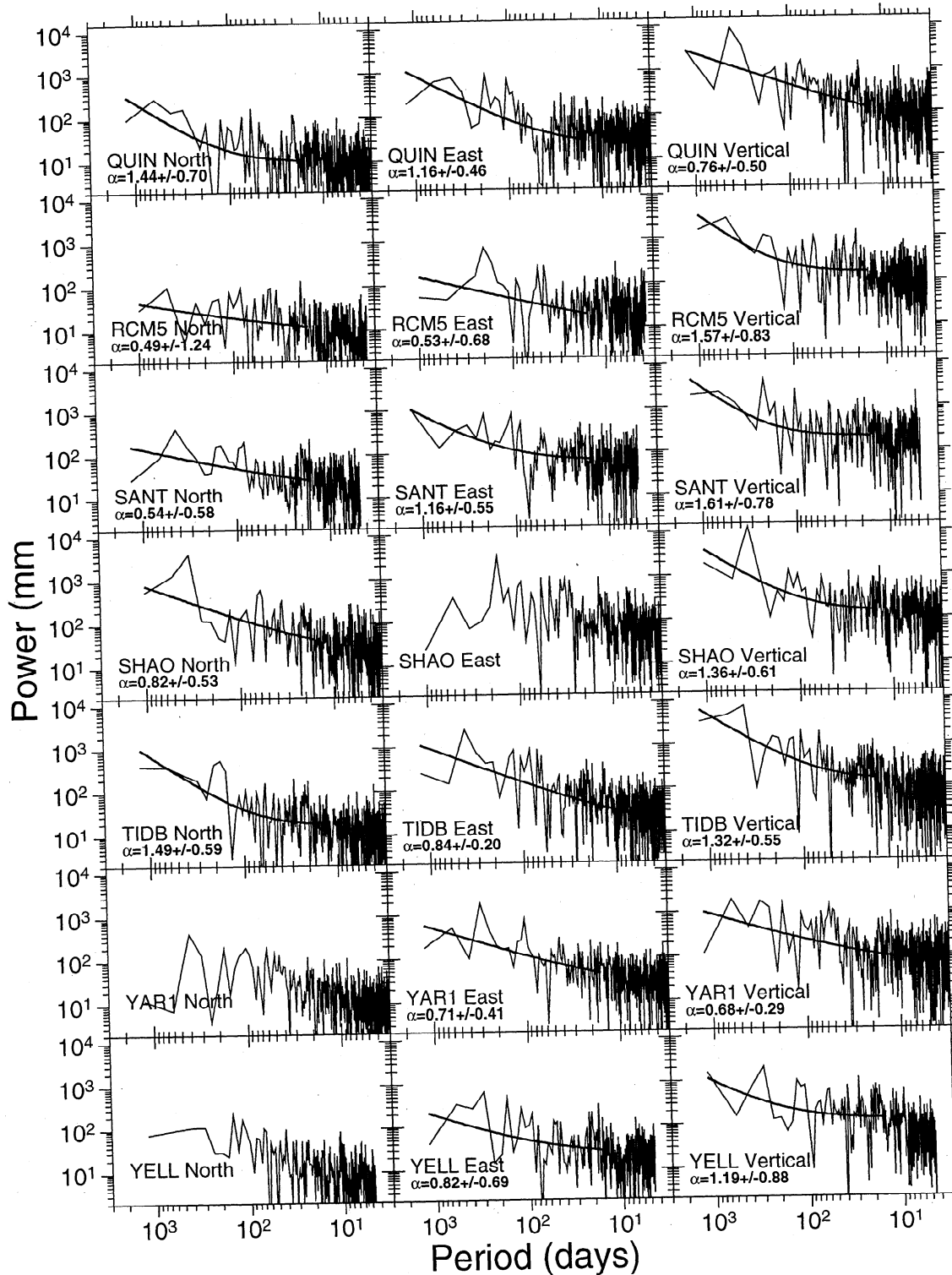
Figure 4. (continued)

here, we therefore retained the annual signature. However, for all other results (e.g., MLE) the annual term has been removed to avoid contaminating the low-frequency part of the power spectrum with a known signal, as the main focus of this study is to characterize random noise correlated over a long time span. Note that power at the annual period is clearly present in some of the spectra (e.g., vertical component of FORT and KRAK) but not in others (e.g., vertical component of BRMU, north compo-

nent of ONSA). A few spectra (e.g., vertical component of MAS1) have peaks at the semiannual period.

Our mean spectral indices range from 0.74 to 1.02, depending on component, windowing technique, and whether the mean is weighted or unweighted. These values are bigger than the mean value 0.4±0.1 (one standard error) estimated by Zhang et al. [1997]. This difference may reflect one or more differences between the two analyses. First, Zhang et al. removed a common-

Table 5. Log Maximum Likelihood for Three Noise Models

	North		East		Vertical	
ID	W+F	W+RW	W+F	W+RW	W+F	W+RW
ALGO	121	92	45	32	73	48
BRMU	36	12	46	38	41	35
CASA	74	51	49	37	38	24
CMBB	56	47	27	16	78	58
FAIR	23	18	23	7	52	46
FORT	36	25	23	16	14	10
GOLD	13	3	34	27	73	65
GUAM	49	26	32	15	7	-1
KERG	100	83	22	18	27	12
KIT3	96	84	38	26	54	39
KOKB	59	39	37	21	97	89
KOUR	64	51	20	15	21	14
KRAK	79	70	15	7	21	12
MAS1	32	23	30	21	54	41
ONSA	76	74	59	47	67	54
PIE1	50	37	37	22	62	48
QUIN	53	38	51	42	63	45
RCM5	20	8	16	14	28	22
SANT	8	2	15	9	33	-12
SHAO	64	49	58	39	16	7
TIDB	113	97	88	67	125	107
YAR1	69	52	72	60	50	37
YELL	72	60	38	31	57	28

W+F, white noise plus flicker noise; W+RW, white noise plus random walk noise. Largest value gives preferred model. Values are normalized such that pure white noise model has likelihood=0.

mode error (due to orbits?) present in our data. Second, Zhang et al. were limited to 1.6 years of data; our longer time series may be more sensitive to long-term time-correlated noise. In the future, longer time series will undoubtedly enable more accurate estimates of time-correlated noise than those presented here. Third, Zhang et al. fit a straight line through the spectrum, while we fit a curve (equation (2)), allowing a better approximation to the low-frequency part of the noise spectrum. Zhang et al. also noted that a white plus flicker noise model fit their data.

Table 5 lists the difference of the log maximum likelihood among three models: white noise, white noise plus flicker noise, and white noise plus random walk noise. Larger values of the maximum likelihood indicate the preferred model [*Langbein and Johnson*, 1997; *Zhang et al.*, 1997], in this case, the white noise plus flicker noise model. We have not attempted to establish the statistical significance of a given numerical score returned by the MLE algorithm, as it requires a large number of computer-intensive simulations. Nevertheless, the fact that in every case tested (total 69) the white plus flicker noise model scored higher than the pure white noise or white plus random walk noise models argues strongly for the first model. Moreover, the same result is obtained from the spectral analysis. This is not to say random

walk noise is not present in our time series. Rather, with the current data time span (3 years), current levels of white and flicker noise, and likely levels of random walk noise (1-3 mm/√yr assuming monument noise of the type described by *Langbein and Johnson* [1997]), we are not able to detect it. Below, we discuss the time required to detect this level of random walk noise in time series of the quality currently available. In summary, both the spectral analysis and Maximum Likelihood Estimation are consistent with a white plus flicker noise model, and we adopt this noise model in the remaining discussion.

Table 6 lists the noise magnitude and standard deviation of white noise and flicker noise for the various time series. The annual signal is removed before estimating the noise components. Overall, noise in the east component is slightly higher than the north component, except ALGO and KIT3. The vertical component always has the largest white noise and flicker noise magnitude. The vertical component of CMBB has the largest flicker noise, which may be related to its older antenna and non-spherical radome (used at this site until August, 1997; Table 1) and/or possibly higher sensitivity to multipath due to antenna environment. Independent analyses have also indicated higher noise at this site [*Bar-Sever et al.*, 1998]. For individual components, there is no significant correlation between the magnitudes of white and flicker noise, but when all three components are plotted together, there is a good overall correlation (Figure 5). The mean white noise amplitudes are 3.3, 5.9, and 10.3 mm for the north, east, and vertical components. The corresponding flicker noise values are 5.7, 7.8, and 14.7 mm.

In order to test the possibility that our results are biased because our time series are too short, we applied our analysis to some GPS time series that are over 6.0 years in length analyzed in a similar way [M.Heflin, personal communication, 1997]. We found that the two results are very close for most of the sites (Figure 6), which suggests that our 3 year results adequately characterize the noise. However, higher (5-10%) amplitude flicker noise is observed in some of the longer (6.0 years) time series, perhaps indicating that longer time series are more sensitive to long period time-correlated errors. An alternate explanation is that the longer time series necessarily includes 1992 and 1993 data, which tend to be noisier than later data.

4.2. Regional Correlations

Figure 7 plots the white and flicker noise amplitudes as a function of station latitude. In general, latitudinal effects are small. While there is a slight tendency for southern hemisphere stations to have larger noise amplitudes, the difference is small and not statistically significant. On the other hand, tropical stations (between -23° and +23° latitude) clearly have higher levels of white noise in the vertical component compared to other stations (Figure 7). The difference is statistically significant at 95% confidence. Four stations (FORT, GUAM, KOUR, and KOKB) are in this latitude band. Two of these (FORT and GUAM) are equipped with newer Turbo Rogue receivers, one (KOUR) is equipped with the older Rogue receiver and one (KOKB) experienced a receiver upgrade (Rogue to Turbo Rogue) midway through the time series studied here with no obvious effects (Table 1, Figure 3). Thus the difference is unlikely to be due to hardware differences.

Inspection of time series from other stations in our database not analyzed for this report suggests the effect is real and not an artifact of small sample size. The weighted rms scatter (WRMS) in the vertical component is a reasonable proxy for white noise.

Table 6. Noise Amplitude

ID	North			East			Vertical		
	WRMS	σ_w	σ_f	WRMS	σ_w	σ_f	WRMS	σ_w	σ_f
ALGO	3.4	1.8±0.1	4.9±0.2	4.4	3.6±0.1	4.1±0.3	10.3	6.6±0.3	13.9±0.7
BRMU	3.6	2.6±0.1	4.2±0.3	6.6	5.1±0.2	5.6±0.5	12.5	10.0±0.3	10.8±1.1
CASA	4.2	2.5±0.1	5.3±0.3	6.9	5.1±0.2	6.8±0.5	12.5	9.4±0.3	12.4±0.9
CMBB	4.9	3.1±0.1	5.6±0.4	9.6	6.4±0.3	9.6±0.8	19.8	9.6±0.6	24.0±1.4
FAIR	4.0	3.0±0.1	3.9±0.4	5.3	3.5±0.2	5.8±0.5	13.7	8.2±0.5	15.2±1.3
FORT	5.9	4.2±0.2	5.9±0.5	9.2	7.5±0.3	7.3±0.8	19.0	15.7±0.5	12.3±1.8
GOLD	3.7	3.0±0.1	3.6±0.3	7.5	5.5±0.2	6.8±0.7	16.3	8.5±0.5	21.4±1.3
GUAM	7.0	4.4±0.2	9.2±0.6	12.3	8.9±0.3	14.7±1.1	19.0	16.7±0.5	14.5±2.1
KERG	8.3	4.8±0.2	10.4±0.6	10.0	8.5±0.3	7.7±0.8	15.2	12.0±0.4	15.9±1.4
KIT3	7.7	3.8±0.2	10.9±0.5	8.1	6.0±0.2	8.3±0.7	13.7	7.9±0.4	17.8±1.0
KOKB	4.5	3.2±0.1	5.4±0.3	8.7	6.5±0.2	8.8±0.7	17.2	12.1±0.4	17.5±1.3
KOUR	6.1	3.9±0.2	6.8±0.5	10.8	9.2±0.3	7.9±1.0	22.2	17.0±0.6	17.1±2.2
KRAK	4.3	2.9±0.1	4.7±0.3	6.9	5.6±0.2	6.2±0.7	14.2	11.3±0.4	12.5±1.3
MAS1	5.5	4.0±0.1	4.8±0.5	8.7	6.9±0.3	8.5±0.9	14.8	9.7±0.5	18.9±1.3
ONSA	4.3	2.7±0.1	4.7±0.3	6.7	3.9±0.2	8.0±0.5	10.2	6.4±0.3	12.1±0.9
PIE1	3.2	2.1±0.1	3.9±0.3	6.3	4.2±0.2	6.6±0.5	11.0	7.3±0.3	12.3±0.9
QUIN	4.1	2.9±0.1	4.8±0.3	7.1	5.4±0.2	6.5±0.5	13.9	9.9±0.3	13.4±1.0
RCM5	3.8	3.1±0.1	3.7±0.4	6.5	5.4±0.2	5.4±0.4	13.6	11.1±0.4	11.9±1.3
SANT	5.9	5.0±0.2	4.0±0.5	9.4	8.0±0.3	6.5±0.8	15.8	12.6±0.5	13.9±1.5
SHAO	7.8	5.1±0.2	8.4±0.6	10.7	7.2±0.3	14.0±0.8	14.2	11.3±0.3	10.3±1.3
TIDB	5.0	3.2±0.1	5.6±0.3	7.9	4.7±0.2	10.0±0.5	13.4	8.7±0.3	14.6±0.9
YAR1	4.5	3.0±0.1	5.8±0.3	7.2	5.0±0.2	8.1±0.4	12.1	9.0±0.3	13.3±1.0
YELL	3.6	2.0±0.1	4.5±0.2	5.3	3.8±0.2	5.2±0.5	10.1	6.2±0.3	12.4±0.8
Mean	5.0	3.3±0.9	5.7±2.1	7.9	5.9±1.7	7.8±2.5	14.6	10.3±3.0	14.7±3.4

Noise amplitude is in mm. WRMS, Weighted rsms.
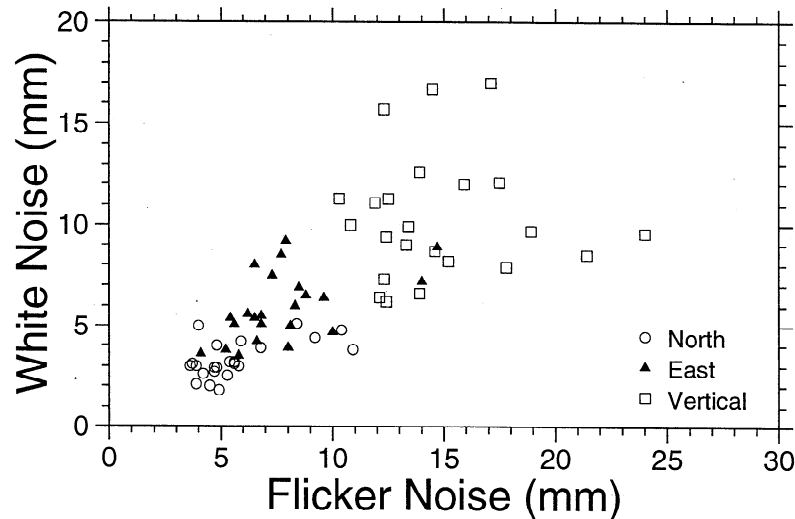
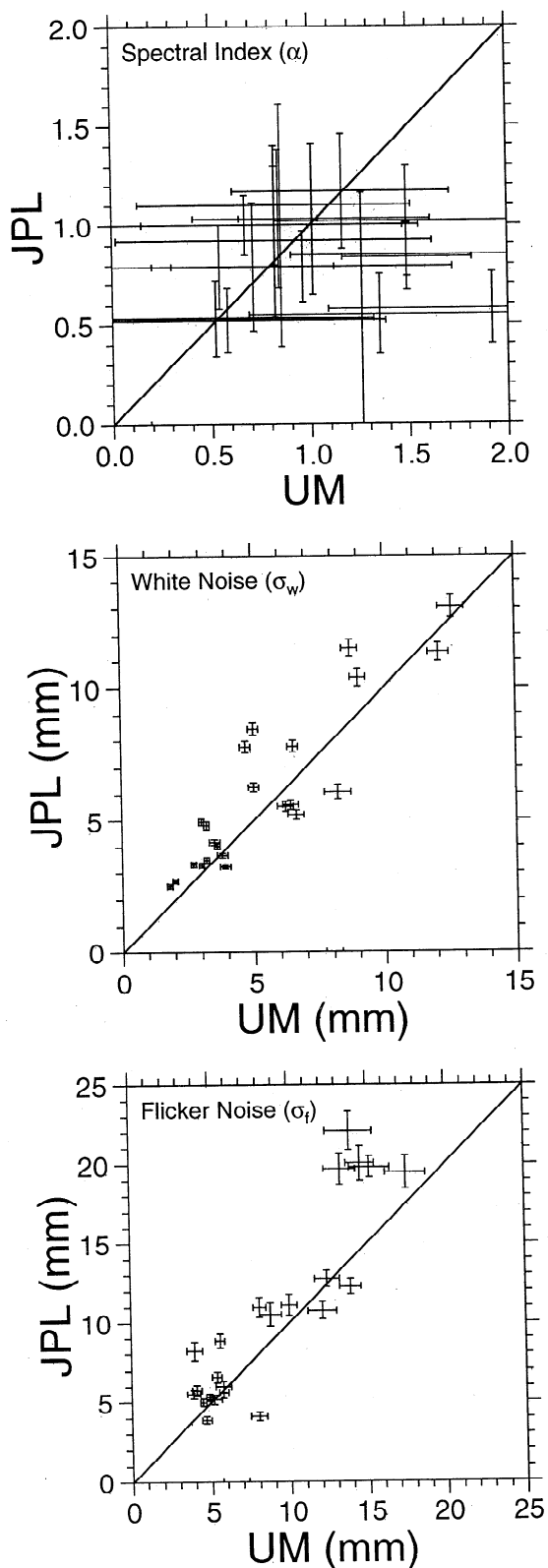**Figure 5.** White noise versus flicker noise amplitude for the 23 GPS time series.

The four tropical stations in Table 6 have WRMS values in the vertical component of 19.4 mm, while the 18 nontropical stations (excluding CMBB) have mean vertical WRMS ranging from 10 to 16 mm (mean = 13.2 mm). Eight other tropical stations in our database not used in this analysis and not affected by antenna changes have WRMS values ranging from 15 to 29 mm (mean = 18.2 mm).

Several explanations seem plausible. Perhaps the additional noise is related to tropospheric water vapor, which exhibits higher levels and higher variability in tropical regions [e.g., *Dixon and Kornreich Wolf*, 1990] and thus is more sensitive to mismodeling. Note that any atmospheric effects in our time series are residual, representing the effects of atmospheric delay unmodeled in the estimation process. Another possibility is that the additional white noise in the vertical component is related to environmental effects near the antenna that are more common in the humid tropics. High moisture on the antenna housing or antenna element might promote elevation angle-dependent phase errors. Elevation angle-dependent errors tend to affect the vertical component more than the horizontal components. For example, we have observed mold growing on one side of a plastic antenna cover in one tropical station within one year of installation.

Table 7. Velocity Error Estimates for White and White Plus Flicker Noise Models

ID	North W	North W+F	East W	East W+F	Vertical W	Vertical W+F
ALGO	0.1	1.1	0.2	0.9	0.4	3.1
BRMU	0.1	0.9	0.3	1.2	0.5	2.4
CASA	0.2	1.2	0.3	1.5	0.5	2.8
CMBB	0.3	1.4	0.5	2.4	1.1	5.7
FAIR	0.2	0.9	0.3	1.3	0.8	3.5
FORT	0.2	1.2	0.4	1.5	0.8	2.6
GOLD	0.2	0.8	0.3	1.5	0.7	4.6
GUAM	0.4	2.5	0.6	4.1	1.0	4.1
KERG	0.4	3.0	0.5	2.3	0.8	4.6
KIT3	0.4	3.0	0.5	2.4	0.8	5.0
KOKB	0.2	1.2	0.3	2.0	0.7	3.9
KOUR	0.3	1.5	0.5	1.8	1.0	3.8
KRAK	0.2	1.2	0.4	1.7	0.7	3.4
MAS1	0.4	1.4	0.6	2.4	1.0	5.2
ONSA	0.3	1.2	0.4	2.0	0.6	3.0
PIE1	0.1	0.8	0.3	1.4	0.5	2.7
QUIN	0.2	1.1	0.3	1.5	0.5	3.0
RCM5	0.2	1.1	0.4	1.6	0.8	3.5
SANT	0.3	0.9	0.4	1.5	0.7	3.1
SHAO	0.4	2.3	0.5	3.8	0.7	2.9
TIDB	0.2	1.3	0.3	2.2	0.5	3.3
YAR1	0.2	1.3	0.3	1.8	0.5	3.0
YELL	0.2	1.0	0.3	1.2	0.5	2.8

Velocity error estimates are in mm/yr.

Figure 6. Comparison of spectral index (α) and amplitude of white and flicker noise computed for 3 year time series (this study) and 6 year time series (M.*Heflin*, personal communication, 1997) for sites where both are available. The solid line has a slope of 1.00. One standard error bars are also shown.
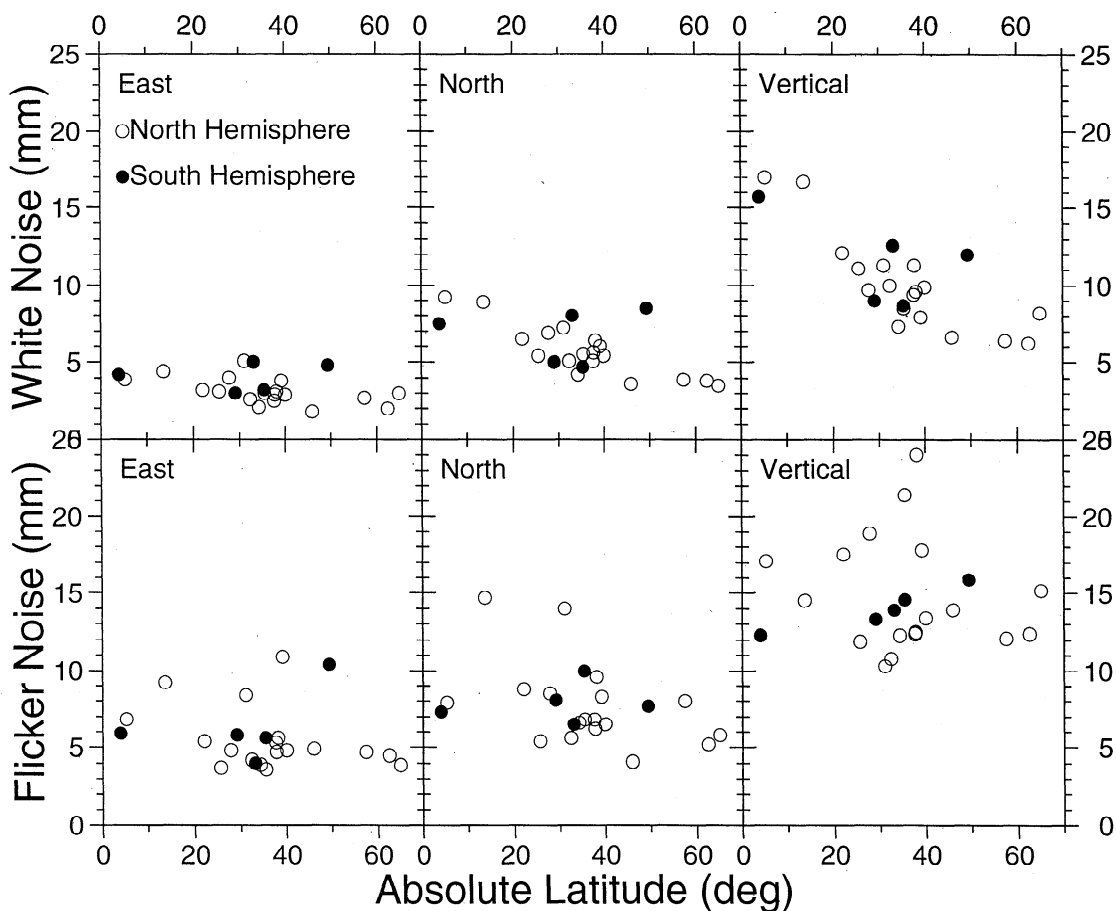
Figure 7. White and flicker noise (Table 6) as a function of absolute latitude. Error bars for these data are of the order of the symbol size and are omitted for clarity.

Inspection of Table 6 suggests another possible regional variation in noise. Stations in North America and western Europe tend to be less noisy than stations in other areas. While this might reflect tracking station density (influencing the quality of satellite ephemerides?), it could be an artifact of our small sample size or may simply reflect greater resources available to maintain and replace older equipment.

4.3. Effect of Time Correlated Noise on Velocity Error Estimates

The standard error of a rate (σ_r) estimated in a linear regression of evenly spaced measurements can be expressed for pure white noise as [Zhang et al., 1997]

$$\left(\sigma_r\right)_w \cong \frac{2\sqrt{3}\sigma_w}{N^{1/2}T} = \frac{2\sqrt{3}\sigma_w}{f_s^{1/2}T^{3/2}} \qquad N \gg 1 \qquad (18)$$

and for random walk noise as

$$\left(\sigma_r\right)_{rw} \cong \frac{\sigma_{rw}}{T^{1/2}} \qquad N \gg 1 \qquad (19)$$

where T is the time span, f_s is the sampling frequency, and σ_w and σ_{rw} are the standard deviations of white and random walk

noise. There is no exact analytical expression for flicker noise; its effect on rate uncertainty has been calculated numerically. For pure white noise the rate error depends on time span as $1/T^{3/2}$, while for random walk noise the rate error goes as $1/T^{1/2}$ and is not dependent on sampling frequency at all. For flicker noise the rate error depends on these parameters in an intermediate way. For example, the time span dependence is $\sigma_r \approx \sigma_f/T$. Figure 8a shows the effects of various combinations of white, flicker, and random walk noise on rate estimates based on linear regression for time series of different lengths using typical white and flicker noise values derived from this study. The rate uncertainties decrease more slowly for time series containing significant time-correlated noise, especially for time series that are long compared to the crossover period (the point where the contributions of white noise and time-correlated noise are equal). The velocity errors of GPS sites based on the model of white noise plus flicker noise are listed in Table 7. If only white noise is assumed, velocity errors are underestimated by factors of 5-11.

An approximate expression for total rate error, valid for evenly spaced measurements, can be obtained by summing the variances (σ^2) from (18) and (19) and adding an expression for the variance contribution from flicker noise:

$$\sigma_r \cong \left(\frac{12\sigma_w^2}{gT^3} + \frac{a\sigma_f^2}{g^bT^2} + \frac{\sigma_{rw}^2}{T}\right)^{1/2} \qquad (20)$$
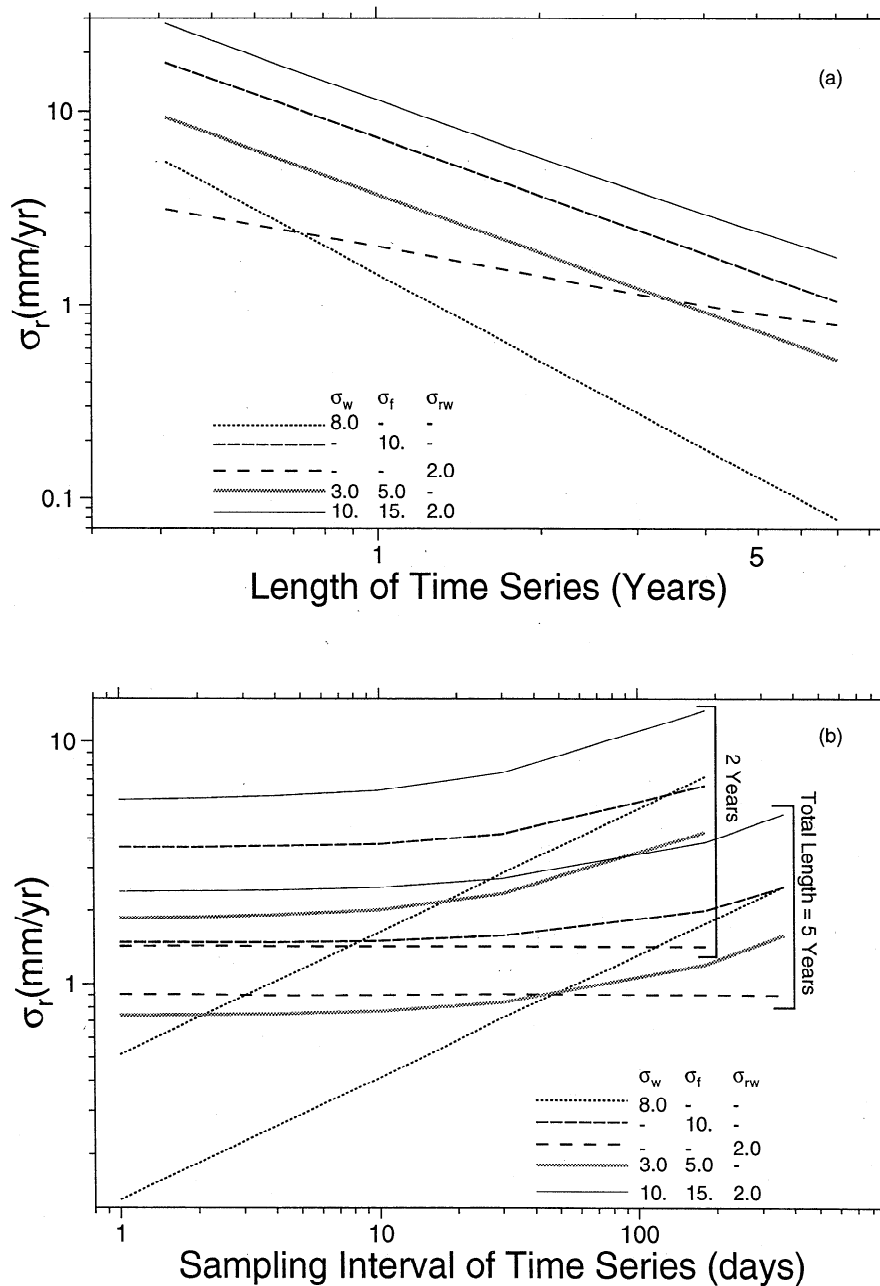
Figure 8. Velocity errors for time series with different lengths (Figure 8a; daily sampling) or sampling intervals (Figure 8b). In addition to time series of pure white noise, flicker noise, and random walk noise, the table also shows the "average best case" ($\sigma_w = \pm 3$ mm, $\sigma_f = \pm 5$ mm) and "average worst case" ($\sigma_w = \pm 10$ mm, $\sigma_f = \pm 15$ mm, $\sigma_{rw} = \pm 2$ mm/$\sqrt{}$yr) on the basis of Table 6 and *Langbein and Johnson* [1997].

where g is the number of measurements per year, T is the total time span in years, σ_w and σ_f are the magnitudes of white and flicker noise in mm, σ_{rw} is the random walk noise in mm/$\sqrt{}$yr, and a and b are empirical constants. By comparison with the numerical results shown in Figure 8, we obtain $a \approx 1.78$ and $b \approx 0.22$. For stations not analyzed in this report, an estimate of the total rate error can be made using (20), the regional average noise values compiled in Table 8, and values for random walk noise in the range 1-4 mm/$\sqrt{}$yr [*Langbein and Johnson*, 1997].

Assuming that monument noise can be characterized as a random walk, and assuming that a typical magnitude for this process is 2.0 mm/$\sqrt{}$yr [*Langbein and Johnson*, 1997], we can estimate

the time required before the velocity estimates become sensitive to this source noise, i.e., the crossover period. For time series with relatively high levels of white and flicker noise (e.g., 10 and 15 mm, respectively, in Figure 8a), more than 15 years is required. For lower levels of white and flicker noise (e.g., 3 and 5 mm, respectively, in Figure 8a) the velocity estimates are sensitive to random walk monument noise within about 4 years. For short baselines [e.g., *Dixon et al.*, 1997] or dense networks where common-mode error reduction can be exploited [*Wdowinski et al.*, 1997] the effects of monument noise may be manifested sooner than 4 years.

An informal test of the noise model can be performed by fit-

Table 8. Mean and Standard Deviation for White and Flicker Noise by Region

	White, mm			Flicker, mm		
	North	East	Vertical	North	East	Vertical
Tropical	3.9±0.5	8.0±1.3	15.4±2.3	6.8±1.7	9.7±3.4	15.4±2.4
North America, Western Europe[a]	2.6±0.4	4.6±0.8	8.6±1.9	4.4±0.6	6.3±1.1	13.5±2.9
Other	4.1±0.9	6.6±1.4	10.2±1.8	7.1±2.8	9.0±2.4	15.1±2.6

N, north; E, east; V, vertical.
[a]Omits CMBB.

ting the velocity data and modeled errors for sites on the stable interior of a plate to a rigid plate model. Assuming that the plate is perfectly rigid, the average velocity residual (observed velocity minus the velocity predicted by the best fit Euler vector) should approximately reflect the modeled noise, and the reduced chi-square statistic (chi-square per degree of freedom, a measure of goodness of fit) should be of order unity. *Mao* [1998] fit the velocity of 19 sites located on stable North America with at least 1.6 years of data to a rigid plate model, obtaining a reduced chi-square of 28.9 (white noise model) and 1.28 (white plus flicker noise model). With a slightly different subset of data (16 sites on the stable plate interior, all with time series 2.0 years or longer) we obtain a reduced chi-square of 0.80 with the white plus flicker noise model. These tests confirm our expectation that a pure white noise model underestimates total velocity error, and suggests that our new noise model, accounting for time correlated noise, accurately estimates total velocity error for the current coordinate velocity data set.

The effect of sampling interval is clear from Figure 8b and the form of (20). A high sampling rate reduces white noise and flicker noise, although it is less efficient for the latter, but has no effect in the case of random walk noise. Continuous measurements are nevertheless important, as they are the best way to measure, understand, and hopefully reduce time-correlated noise.

5. Conclusions

1. Spectral analysis of coordinate time series spanning 3 years from globally distributed GPS sites suggests that the noise characteristics of all three components can be modeled by a combination of white plus flicker noise.

2. Both white and flicker noise amplitudes increase in the order north, east, and vertical.

3. The white noise part of the vertical component is higher for tropical (±23° latitude) stations than mid-latitude and high-latitude stations.

4. Southern Hemisphere stations are not significantly noisier than Northern Hemisphere stations.

5. The velocity error in coordinate time series may be underestimated by factors of 5-11 if a pure white noise model is assumed.

6. Longer time series than those presented here will be required to accurately assess random walk noise in GPS coordinate time series.

References

Agnew, D.C., The time-domain behavior of power-law noises, *Geophys. Res. Lett.*, *19*, 333-336, 1992.

Bar-Sever, Y.E., P.M. Kroger, and J.A. Borjesson, Estimating horizontal gradients of tropospheric path delay with a single GPS receiver, *J. Geophys. Res.*, *103*, 5019-5035, 1998.

Brockwell, P. J., and R. A. Davis, Introduction to Time Series and Forecasting, 420pp., Springer-Verlag, New York, 1996.

Boucher, C., Z. Altamimi, M. Feissel, and P. Sillard, Results and analysis of the ITRF94, 191 pp., *Tech. Note 20, Int. Earth Rotation Serv.*, 1996.

Dixon, T.H., A. Mao, M. Bursik, M. Heflin, J. Langbein, R. Stein, and F. Webb, Continuous monitoring of surface deformation at Long Valley Caldera, California, with GPS, *J. Geophys. Res.*, *102*, 12,017-12,034, 1997.

Johnson, H.O., and D.C. Agnew, Monument motion and measurements of crustal velocities, *Geophys. Res. Lett.*, *22*, 2905-2908, 1995.

Johnson, H. O., and F. K. Wyatt, Geodetic network design for fault mechanics studies, *Manuscr. Geod.*, *19*, 309-323, 1994.

Koch, K.R., Maximum likelihood estimate of variance components, *Bull. Geod.*, *60*, 329-338, 1986.

Langbein, J., and H. Johnson, Correlated errors in geodetic time series: Implications for time-dependent deformation, *J. Geophys. Res.*, *102*, 591-604, 1997.

Langbein, J., F. Wyatt, H. Johnson, D. Hamann, and P. Zimmer, Improved stability of a deeply anchored geodetic monument for deformation monitoring, *Geophys. Res. Lett.*, *22*, 3533-3536, 1995.

Lomb, N.R., Least squares frequency analysis of unequally spaced data, *Astrophys. Space Sci.*, *39*, 447-462, 1976.

Mao, A., Geophysical applications of the Global Positioning System. Ph. D. dissertation, University of Miami, 149 pp., 1998.

Press, W.H., B.P. Flannery, S.A. Teukolsky, and W.T. Vetterling, *Numerical Recipes*, 818 pp., Cambridge Univ. Press, New York, 1992.

Scargle, J.D., Studies in astronomical time series analysis, II, Statistical aspects of spectral analysis of unevenly spaced points, *Astrophys. J.*, *263*, 835-853, 1982.

Wdowinski, S., Y. Bock, J. Zhang, P. Fang, and J. Genrich, Southern California Permanent GPS Geodetic Array: Spatial filtering of daily positions for estimating coseismic and postseismic displacements induced by the 1992 Landers earthquake, *J. Geophys. Res.*, *102*, 18,057-18,070, 1997.

Wessel, P., and W. H. F. Smith, New version of the Generic Mapping Tools released, *Eos Trans. AGU, 76 (33)*, 329-330, 1995.

Zhang, J., Y. Bock, H. Johnson, P. Fang, S. Williams, J. Genrich, S.

Wdowinski, and J. Behr, Southern California Permanent GPS Geodetic Array: Error analysis of daily position estimates and site velocities, *J. Geophys. Res., 102,* 18,035-18,055, 1997.

Zumberge, J. F., M. B. Heflin, D. C. Jefferson, M. M. Watkins, and F. H. Webb, Precise point positioning for the efficient and robust analysis of GPS data from large networks, *J. Geophys. Res., 102,* 5005-5017, 1997.

T. H. Dixon and C. G. A. Harrison, Marine Geology and Geophysics Division, Rosenstiel School of Marine and Atmospheric Science, University of Miami, 4600 Rickenbacker Causeway, Miami, FL 33149-1098 (tim@corsica.rsmas.miami. edu; charrison@rsmas.miami.edu)

A. Mao, Magellan Systems Corporation, 960 Overland Court, San Dimas, CA 91773.

Present-day motion of the Sierra Nevada block and some tectonic implications for the Basin and Range province, North American Cordillera

Timothy H. Dixon,[1] Meghan Miller,[2] Frederic Farina,[1] Hongzhi Wang[1] and Daniel Johnson[2]

Abstract. Global Positioning System (GPS) data from five sites on the stable interior of the Sierra Nevada block are inverted to describe its angular velocity relative to stable North America. The velocity data for the five sites fit the rigid block model with rms misfits of 0.3 mm/yr (north) and 0.8 mm/yr (east), smaller than independently estimated data uncertainty, indicating that the rigid block model is appropriate. The new Euler vector, 17.0°N, 137.3°W, rotation rate 0.28 degrees per million years, predicts that the block is translating to the northwest, nearly parallel to the plate motion direction, at 13-14 mm/yr, faster than previous estimates. Using the predicted Sierra Nevada block velocity as a kinematic boundary condition and GPS, VLBI and other data from the interior and margins of the Basin and Range, we estimate the velocities of some major boundary zone faults. For a transect approximately perpendicular to plate motion through northern Owens Valley, the eastern California shear zone (western boundary of the Basin and Range province) accommodates 11±1 mm/yr of right-lateral shear primarily on two faults, the Owens Valley-White Mountain (3±2 mm/yr) and Fish Lake Valley (8±2 mm/yr) fault zones, based on a viscoelastic coupling model that accounts for the effects of the 1872 Owens Valley earthquake and the rheology of the lower crust. Together these two faults, separated by less than 50 km on this transect, define a region of high surface velocity gradient on the eastern boundary of the Sierra Nevada block. The Wasatch Fault zone accommodates less than 3±1 mm/yr of east-west extension on the eastern boundary of the Basin and Range province. Remaining deformation within the Basin and Range interior is also probably less than 3 mm/yr.

1. Introduction

Plate boundaries within continents are often characterized by diffuse zones of deformation, quite distinct from the narrow plate boundaries that characterize oceanic lithosphere and define large rigid plates. However, at least some continental areas appear to behave like oceanic lithosphere in one important respect: deformation is occasionally concentrated in narrow fault zones that accommodate relative motion between rigid blocks. The Sierra Nevada block in the western United States is probably a good example of a rigid continental block [*Wright,* 1976]. Seismicity around its margins delineates an aseismic region east of the San Andreas fault and west of the Basin and Range extensional province (Figure 1). However, a rigorous test of the rigidity of this block has never been performed (nor, to our knowledge, for any other continental block or microplate). Perhaps the Sierra Nevada block is not rigid at all, and the absence of seismicity indicates a weak block undergoing diffuse aseismic deformation, or strain accumulation on a few locked faults cutting the block, previously assumed inactive or active at low strain rates (e.g., the Kern Canyon fault), to be released in future large earthquakes.

Space geodesy can rigorously test the concept of rigid continental blocks, just as it can measure the angular velocity and test the rigidity of larger plates [*Argus and Gordon,* 1996; *Dixon et al.,* 1996]. Since the motions of rigid blocks or plates on a sphere can be described by Euler (angular velocity) vectors [e.g., *Chase,* 1978; *Minster and Jordan,* 1978; *DeMets et al.,* 1990], we can test whether velocity data from sites on a continental block are well fit by a given Euler vector, and whether velocity predictions on the margins of the block based on this Euler vector are consistent with other observations. An accurate estimate of Sierra Nevada block motion also holds the key to understanding certain aspects of Pacific-North American plate interaction [e.g., *Atwater,* 1970; 1989; *Dixon et al.,* 1995; *Wells et al.,* 1998; *Hearn and Humphreys,* 1998].

Minster and Jordan [1987] first applied space geodetic data to estimate motion of the Sierra Nevada block, defining northwest motion of the block at a velocity of ~10±2 mm/yr. *Argus and Gordon* [1991] estimated an Euler vector for the block, defining counterclockwise rotation of the block about a pole located close to and southwest of the block, and northwest to north-northwest motion of the block at 9-11 mm/yr, depending on location. Both of these pioneering studies used very long baseline interferometry (VLBI) data from a few sites near the deforming eastern margin of the block. The small number of sites available at the time precluded a test of the rigid block hypothesis, while the site locations limited the accuracy of the relative motion estimates for the Sierra Nevada block, since they are not actually located on the stable block (Figure 1). New Global Positioning System (GPS) data from sites on the stable interior and margins of the block are now available, enabling us to perform a

---

[1] Rosenstiel School of Marine and Atmospheric Science, University of Miami, Miami, Florida.

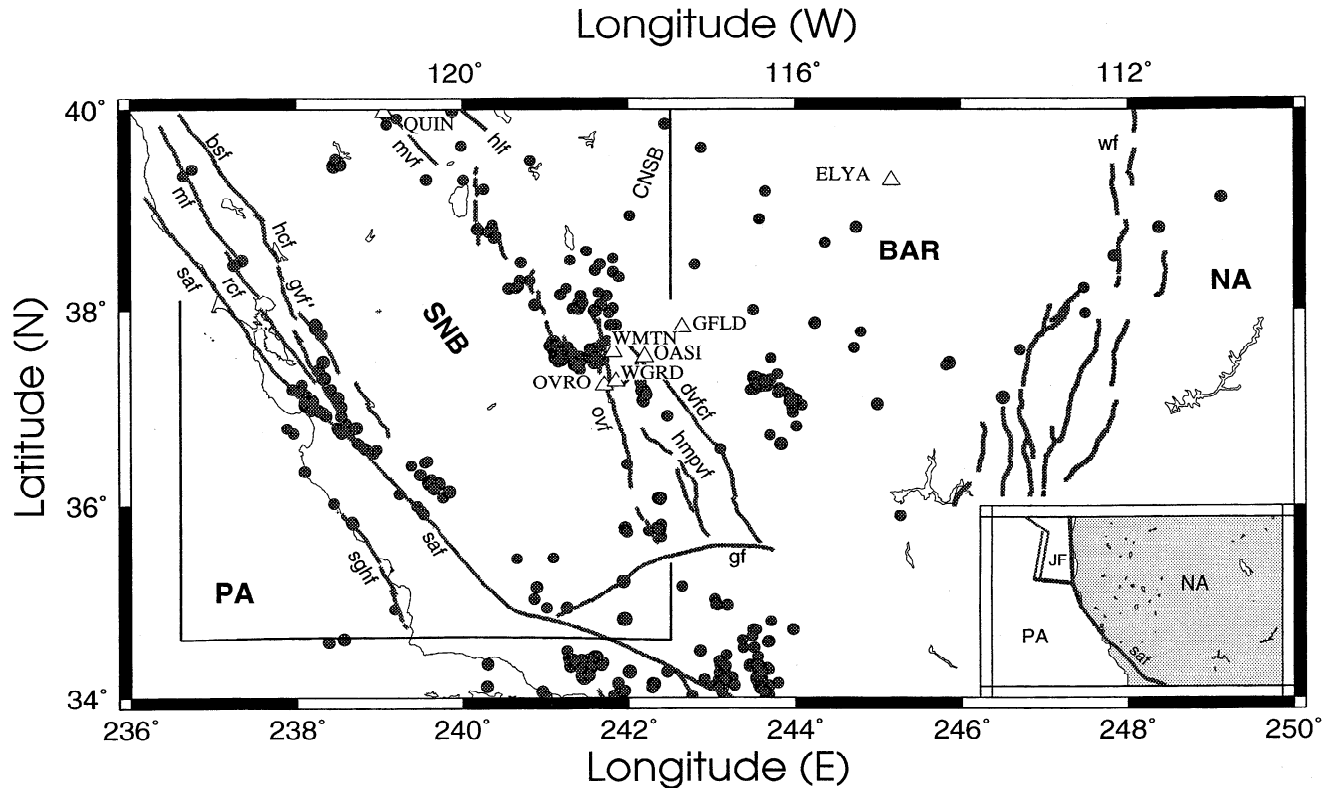[2] Department of Geology, Central Washington University, Ellensburg, Washington.

Figure 1. Regional neotectonic map for the western US, and (inset) major bounding plates: PA, Pacific plate, JF, Juan de Fuca plate, NA, stable North America. Active faults on margins of Sierra Nevada block (SNB) are from *Jennings and Saucedo* [1994]: bsf, Bartlett Springs fault; dvfcf, Death Valley-Furnace Creek fault zone; gf, Garlock fault; gvf, Green Valley fault; hcf, Hunting Creek fault; hlf, Honey Lake fault; hmpvf, Hunter Mountain-Panamint Valley fault zone; mf, Maacama fault zone; mvf, Mohawk Valley fault zone; rcf, Rogers Creek fault zone; ovf, Owens Valley fault zone; saf, San Andreas fault. CNSB, Central Nevada seismic belt. Faults in eastern Basin and Range (BAR) are from *Smith and Arabasz* [1991] and include active faults and Late Cenozoic faults that are possibly active; wf, Wasatch fault zone. Seismicity from the University of California, Berkeley catalog at http://quake.geo.berkeley.edu/cnss/catalog-search.html shows all events after 1960 with magnitude >4.5 and depth less than 30 km. Note paucity of events within SNB. Space geodetic sites within the seismically active eastern boundary of SNB and Basin and Range interior shown as open triangles with four letter identifiers. Sites on SNB are omitted for clarity here, but are shown in Figure 3 (location outlined by light solid line).

rigorous test of the rigid block hypothesis, and refine our understanding of Sierra Nevada motion and associated crustal deformation. These data, and the new interpretations they afford, are the focus of this paper.

2. Observations and Data Analysis

The data used in this study were obtained in several ways:

1. Annual campaigns were conducted in August-September between 1993 and 1998, although not all sites were occupied each year. Most sites were observed for 24 hours per day for 3-5 days, in campaigns in 1993, 1994, 1995 and 1998 (Figure 2). Where available, the resulting 5 year time series provide accurate site velocity data, as GPS velocity errors depend strongly on the total time span of observations [*Mao et al.*, 1999]. These sites are located on

the interior of the Sierra Nevada block, on its eastern margin, and in the interior of the Basin and Range province (Figures 1 and 3; Table 1);

2. Observations were made at semi-permanent, continuously recording stations in California, on or near the Sierra Nevada block, including Quincy (QUIN), part of the International GPS Service (IGS) network, operating for more than 5 years; Columbia (CMBB) in California, part of the Bay Area Regional Deformation (BARD) network, operating for about 5 years; ORVB, UCD1 and SUTB, also part of the BARD network, operating for about 2 years. Stations operating for less than 2 years (as of March 1999) are not considered in this report;

3. Observations were made at 16 semi-permanent, continuously recording stations widely distributed through eastern and central North America, operated by various agencies, used to define a stable regional reference frame for
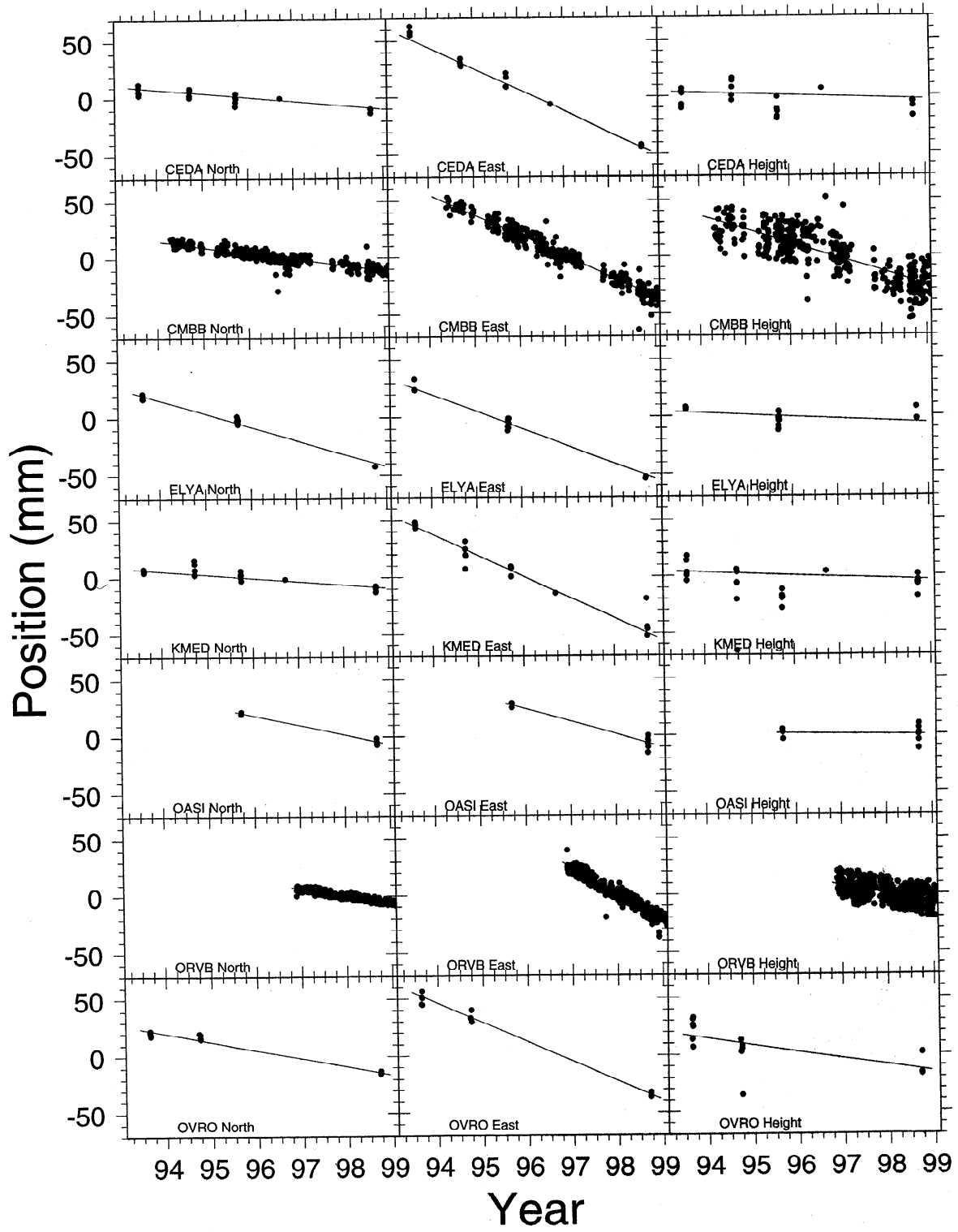
Figure 2. GPS positions (relative to ITRF-96) as a function of time, with an arbitrary constant removed. Error bars (Table 3) omitted for clarity. Slope of best fit line from weighted least squares gives velocities in Table 1.
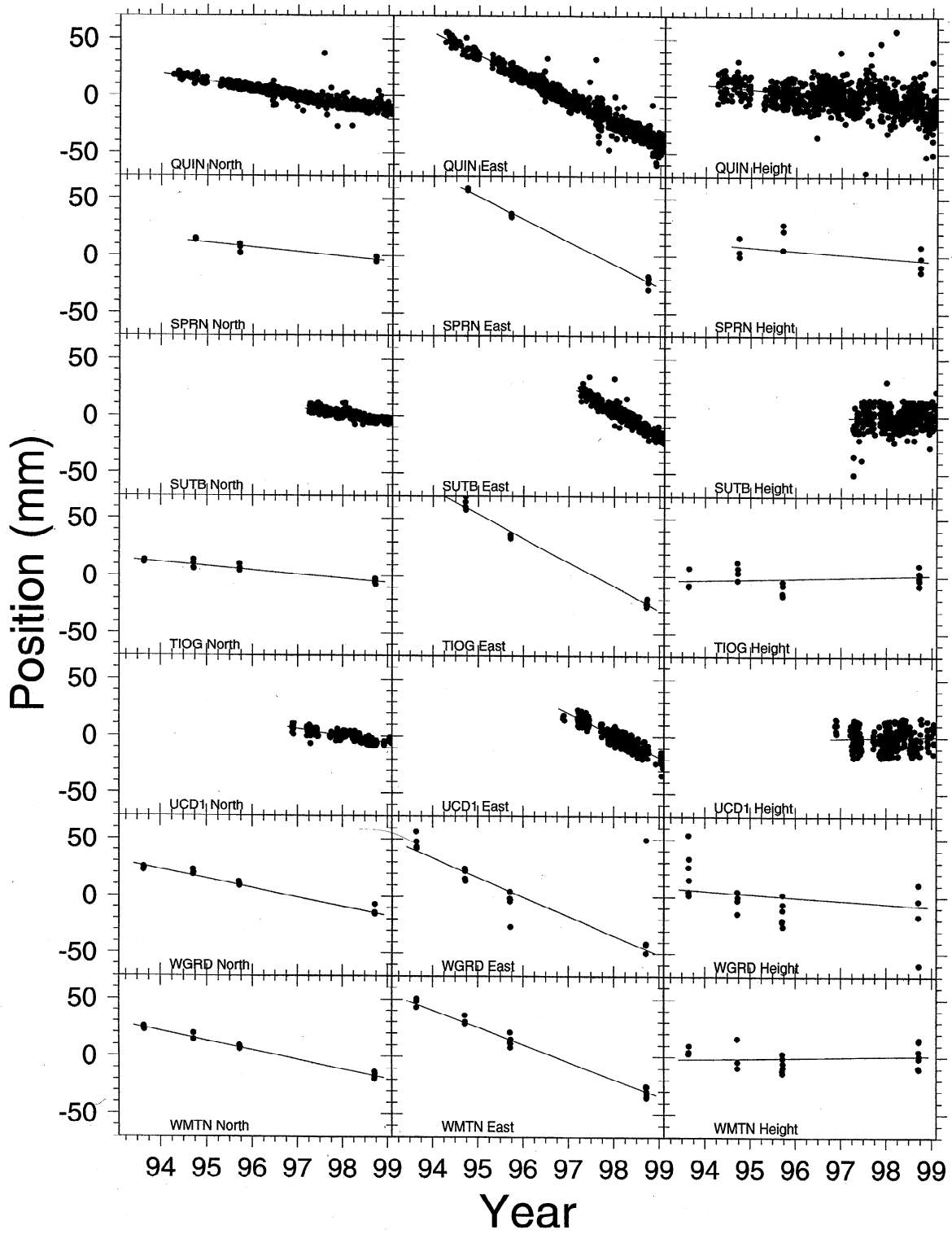
Figure 2. (continued)

Table 1. GPS Site Velocities Relative to ITRF-96

	Latitude, deg N	Longitude, deg W	Velocity, mm/yr		
			North	West	Vertical
CEDA (Cedar Creek)	35.75	118.59	-3.6 ± 0.9	19.3 ± 1.2	-1.4 ± 2.9
CMBB (Columbia)[a]	38.03	120.39	-5.1 ± 0.7	19.4 ± 1.4	-9.6 ± 3.1
GFLD (Goldfield)	37.82	117.36	-11.0 ± 1.6	10.8 ± 2.7	2.6 ± 5.8
ELYA (Ely)	39.29	114.84	-11.6 ± 0.8	14.8 ± 1.1	-2.5 ± 2.9
KMED (Kennedy Meadows)	36.02	118.14	-3.0 ± 0.6	18.5 ± 0.9	-1.5 ± 2.8
OASI (Oasis)	37.52	117.81	-8.5 ± 1.6	11.5 ± 2.7	-0.5 ± 5.8
OVRO (Owens Valley Radio Observatory)	37.23	118.29	-7.3 ± 1.0	16.9 ± 1.6	-5.8 ± 3.4
ORVB (Oroville)	39.55	121.50	-6.6 ± 1.1	21.9 ± 1.7	-7.2 ± 3.8
QUIN (Quincy)	39.97	120.94	-6.5 ± 0.6	18.8 ± 0.9	-4.0 ± 2.2
SPRN (Springville)	36.18	118.73	-3.9 ± 1.1	20.2 ± 1.8	-3.1 ± 3.7
SUTB (Sutter Buttes)	39.21	121.82	-5.9 ± 1.2	22.2 ± 2.0	-0.4 ± 4.8
TIOG (Tioga Pass)	37.93	119.25	-3.8 ± 0.5	21.7 ± 1.0	0.4 ± 2.7
UCD1 (UC Davis)[b]	38.54	121.75	-5.8 ± 1.4	17.5 ± 2.1	1.6 ± 5.5
WGRD (Westguard Pass)	37.27	118.15	-8.2 ± 0.8	16.9 ± 1.4	-2.8 ± 3.5
WMTN (White Mountain)	37.57	118.24	-8.3 ± 0.7	14.9 ± 0.9	-0.9 ± 2.9

[a] Vertical time series has unexplained offset.

[b] Vertical rate based on post-April, 1998 data because of antenna change.

the Sierra Nevada data. These stations provide time series that are longer than 3 years.

Data were analyzed at the University of Miami following *Dixon et al.* [1997]. Briefly, we used the GIPSY software developed at the Jet Propulsion Laboratory [JPL] and satellite ephemeris and clock files provided by JPL [*Zumberge et al.*, 1997]. These procedures resulted in site velocities defined in global reference frame ITRF-96 [*Sillard et al.*, 1998] (Table 1). Errors are estimated following *Mao et al.* [1999] and account for the influence of both white and colored noise (see section 2.1). A formal inversion procedure [*Ward*, 1990] is used to derive site velocities relative to stable North America and generate an Euler vector describing motion of the Sierra Nevada block relative to stable North America. The method is described

in detail by *Mao* [1998]. We first define best fitting ITRF-96 Euler vectors for eight Sierran stations (CEDA, CMBB, KMED, ORVB, SPRN, SUTB, TIOG, UCD1) or some subset, and the 16 stations on stable North America [*Dixon et al.*, 1996; *DeMets and Dixon*, 1999]. These two Euler vectors are then used to define a relative Euler vector describing rotation of the Sierra Nevada block with respect to North America. The 16 North American stations are sufficient to ensure a robust regional reference frame (stable North America), such that reference frame "noise" is much smaller than the velocity error of any individual Sierran station, allowing us to define the velocities of the Sierran sites relative to stable North America (Table 2) with high accuracy. Subsets of data from the Sierran sites can be used to test block rigidity and to assess the level of

Table 2. Site Velocities Relative to Stable North America

	North, mm/yr	West, mm/yr	Rate, mm/yr	Azimuth, deg clockwise from N
CEDA	9.7 ± 1.0	9.2 ± 1.3	13.4 ± 1.1	317 ± 5
CMBB	8.7 ± 0.8	9.0 ± 1.4	12.6 ± 1.2	314 ± 5
ELYA	0.6 ± 0.9	3.3 ± 1.2	3.4 ± 1.2	280 ± 14
GFLD	2.0 ± 1.6	0.0 ± 2.7	2.0 ± 1.6	359 ± 77
KMED	10.2 ± 0.7	8.2 ± 1.0	13.1 ± 0.9	321 ± 4
OASI	4.6 ± 1.6	0.9 ± 2.7	4.7 ± 1.7	349 ± 33
OVRO	5.9 ± 1.1	6.4 ± 1.7	8.7 ± 1.5	313 ± 9
ORVB	7.6 ± 1.2	11.4 ± 1.8	13.6 ± 1.6	304 ± 6
QUIN	7.1 ± 0.6	8.3 ± 0.8	11.0 ± 0.9	313 ± 4
SPRN	9.5 ± 0.6	10.0 ± 1.3	13.8 ± 1.6	313 ± 6
SUTB	8.3 ± 1.3	11.8 ± 2.0	14.4 ± 1.8	305 ± 6
TIOG	9.9 ± 0.5	11.2 ± 1.0	14.8 ± 1.3	311 ± 5
UCD1	8.4 ± 1.5	7.2 ± 2.1	11.1 ± 1.8	321 ± 10
WGRD	5.0 ± 0.9	6.4 ± 1.5	8.1 ± 1.3	308 ± 8
WMTN	4.9 ± 0.8	4.4 ± 1.0	6.5 ± 0.9	319 ± 8

possible "edge" effects from elastic strain accumulation. Similar procedures are used to define the velocities of sites within the Basin and Range province or on its deforming margins (GFLD, ELYA, OASI, OVRO, QUIN, WGRD and WMTN) relative to stable North America.

2.1. Uncertainties

Unless specifically stated, all uncertainties in the tables and text represent one standard error, while all error ellipses in figures represent two-dimensional 95% confidence regions (1.7 times the two-dimensional one standard error). Here we describe the procedures used to estimate these uncertainties.

GPS velocity errors may be estimated assuming that measurement noise is uncorrelated in time ("white"). If time-correlated ("colored") noise is present, the true velocity uncertainty will be underestimated if pure white noise is assumed [*Johnson and Agnew*, 1995]. Possible sources of colored noise in GPS include monument motion unrelated to the larger tectonic motions of interest [*Langbein and Johnson*, 1997], uncertainty in the satellite orbit parameters, and atmospheric and local environmental effects [*Mao et al.*, 1999]. *Zhang et al.* [1997] and *Mao et al.* [1999] demonstrate that GPS velocity errors may be underestimated by factors of 2-11 if pure white noise is assumed. Mao et al. present a simple model for estimating the GPS rate error (σ_r) for individual velocity components (north, east and vertical) for coordinate time series in the presence of combined white and colored noise:

$$\sigma_r^2 \cong \frac{12\sigma_w^2}{gT^3} + \frac{a\sigma_f^2}{g^bT^2} + \frac{\sigma_{rw}^2}{gT} \qquad (1)$$

where g is the number of measurements per year, T is the total time span of observations (2-5 years in this study), a and b are empirical constants (a=1.78 and b=0.22), σ_w and σ_f are the white and "flicker" noise magnitudes in mm, and σ_{rw} is "random walk" noise in mm/$\sqrt{\text{yr}}$. Flicker noise and random walk noise are different types of colored noise, distinguished by their time-dependence (Mao et al. give a complete discussion). Briefly, flicker ("pink") noise has spectral power that is inversely proportional to frequency, while random walk ("red") noise has spectral power that is inversely proportional to frequency squared. Monument noise has been characterized as a random walk process [*Langbein and Johnson*, 1997] and is likely to be more significant for sites in unconsolidated alluvium than for sites in bedrock. From (1) it can be seen that if random walk noise is small, velocity error depends strongly on the total time span of observations (T) and weakly on sampling frequency (g). Mao et al. suggest that white noise and flicker noise dominate the GPS noise spectrum for coordinate time series of the type used here, i.e., random walk noise is relatively small. Thus, our 5 year time series for Sierran stations set into bedrock and occupied in periodic campaigns (CEDA, KMED, SPRN and TIOG) should define accurate site velocities, even though they are sampled much less frequently than semi-permanent, continuously recording stations such as CMBB, ORVB, SUTB and UCD1. The importance of our noise model is that it allows the velocities from these diverse data sets

(campaign or continuous, with various time spans) to be correctly weighted in the inversion to derive Euler vectors.

Equation (1) is strictly valid only for evenly sampled position time series. Our campaign measurements yield very uneven sampling, typically several consecutive days every year or two (Figure 2). Numerical experiments suggest that approximating an unevenly sampled time series such as this by an equivalent evenly sampled time series yields rate error estimates that differ by less than 1 mm/yr from actual values (usually much less). We make the even sampling approximation in this study. As an example, for station CEDA, with a total of 19 observation days over 5 years (Figure 2), we set g equal to 3.8 samples per year.

Application of (1) also requires estimates for white, flicker, and random walk noise. These can vary from station to station, as they depend in part on local station characteristics. *Mao et al.* [1999] list noise values for a number of North American stations including QUIN and CMBB. For the remaining stations, we must estimate noise values using other criteria. Mao et al.'s data show a good correlation between the weighted root-mean-square (WRMS) scatter of an individual time series and corresponding magnitudes of white and flicker noise. These correlations can be used to estimate white and colored noise magnitudes for individual GPS time series, provided that sufficient samples (observation days) are available to ensure that WRMS is a reliable indicator of data quality. GFLD, OASI, and OVRO have anomalously low (optimistic) WRMS values, probably reflecting the small number of observations (Figure 2); their noise estimates are instead based on the average WRMS of all stations in the region with equivalent antenna type and sufficient observations to be representative, listed in the footnote to Table 3. Table 3 also lists the WRMS by component for stations analyzed in this report, and corresponding white and flicker noise estimates based on these correlations (relevant equations are given in footnotes to the table). Our estimates of velocity uncertainty are based on these values, equation (1), and the assumptions stated above.

2.2. Accuracy

One way to assess the accuracy of our derived velocities is to compare results to independent data. This also provides a means to assess the error estimates: if they are reasonable, our expectation is that most velocities reported for the same location should overlap within errors, depending on the confidence level quoted. OVRO and QUIN each have very long baseline interferometry (VLBI) and/or very long baseline array (VLBA) data available for comparison. Table 4 lists published velocities for these sites relative to stable North America, from the compilation of *Hearn and Humphreys* [1998], updated to reflect the latest VLBI/VLBA data, solution GLB 1102 [*Ma and Ryan*, 1998], and our own GPS data. The VLBI results listed are not independent, as they all rely on essentially the same data for the early part of their respective time series, but the manner in which stable North America is

Table 3. Uncertainties

	WRMS			White Noise			Flicker Noise		
	North	East	Vertical	North[a]	East[b]	Vertical[c]	North[d]	East[e]	Vertical[f]
CEDA	3.0	4.9	9.8	2.1	3.6	6.5	3.5	4.8	11.9
CMBB[g]	3.9	8.6	19.7	2.7	6.4	14.8	4.6	8.6	18.6
ELYA	2.5	4.3	8.5	1.8	3.1	5.4	3.0	4.1	11.1
GFLD[h]	3.1	5.6	11.0	2.2	4.1	7.5	3.6	5.5	12.7
KMED	2.1	3.9	9.7	1.6	2.8	6.4	2.5	3.7	11.2
OASI[h]	3.1	5.6	11.0	2.2	4.1	7.5	3.6	5.5	12.7
ORVB	3.0	5.8	10.9	2.1	4.3	7.4	3.5	5.7	12.7
OVRO[h]	3.1	5.6	11.0	2.2	4.1	7.5	3.6	5.5	12.7
QUIN	3.8	6.5	14.2	2.6	4.8	10.2	4.5	6.4	14.9
SPRN	2.8	5.5	9.9	2.0	4.0	6.6	3.3	5.4	12.0
SUTB	2.9	5.6	12.2	2.0	4.1	8.5	3.4	5.5	13.5
TIOG	3.1	6.1	9.3	2.2	4.5	6.1	3.7	6.0	11.6
UCD1[i]	3.6	6.1	11.0	2.5	4.5	7.5	4.2	6.0	12.7
WGRD	2.9	5.9	14.1	2.0	4.3	10.1	3.4	5.8	14.8
WMTN	2.6	3.9	10.8	1.9	2.8	7.3	3.1	3.7	12.6
NoAm[j]	3.8	4.9	12.8	2.6	4.6	8.6	4.4	6.3	13.5

All uncertainties given in millimeters. WRMS is weighted root-mean-square.

[a] White noise $(N) = 0.613[\text{WRMS}(N)] + 0.259$.

[b] White noise $(E) = 0.767[\text{WRMS}(E)] - 0.182$.

[c] White noise $(V) = 0.843[\text{WRMS}(V)] - 1.772$.

[d] Flicker noise $(N) = 1.139[\text{WRMS}(N)] + 0.117$.

[e] Flicker noise $(E) = 1.041[\text{WRMS}(E)] - 0.342$.

[f] Flicker noise $(V) = 0.668[\text{WRMS}(V)] + 5.394$.

[g] Vertical component time series at this site has unexplained offset associated with equipment change and may not give a reliable estimate of vertical velocity averaged over the entire time interval.

[h] Noise values for these stations are based on means of CEDA, KMED, ORVB, QUIN, SUTB, TIOG, and UCD1.

[i] Vertical noise values at UCD1 are based on time series after April 1997 to avoid antenna change effects.

[j] Mean value for North America [*Mao et al.*, 1999].

defined can differ significantly, so the comparisons are still useful. The various VLBI results for a given site often differ by much more than two standard deviations, implying that errors for some of these results may be underestimated. Our GPS estimate for QUIN should be well resolved, as it is based on a large number of data spanning 5 years (Figure 2). QUIN's GPS-based horizontal rate estimate (11 mm/yr) lies in the middle of the range of published VLBI values (9-13 mm/yr). The GPS rate, azimuth, and vertical estimates for QUIN all lie within one standard error of the most recent VLBI result, probably the most accurate estimate available at this site. Our GPS rate estimate for OVRO is based on far fewer data (Figure 2) and thus is less reliable, which is reflected in its larger velocity error (Tables 1, 2 and 4). OVRO's GPS-based rate estimate (9 mm/yr) lies at the low end of the range of available values (9-12 mm/yr). The GPS horizontal rate estimate lies within two standard errors of the recent VLBA result, probably the most accurate estimate available at this site, while the GPS azimuth and vertical estimates for OVRO both lie within one standard error of the VLBA result. The VLBI and VLBA results at OVRO, from

locations several hundred meters apart, themselves differ by 1 mm/yr in rate and 9° in azimuth, which is much larger than quoted errors (Table 4). This discrepancy may reflect underestimation of error or real variation reflecting local complexities in the velocity field, since the sites are located within a right step in the Owens Valley-White Mountain fault zone [*Dixon et al.*, 1995]. The weighted means of recent independent results in Table 4 probably best represent the velocities of OVRO and QUIN. Unless specifically noted, these mean values are used in the remainder of the paper. To avoid overweighting in calculation of the mean, VLBI/VLBA errors were increased by a factor of 2. At OVRO this procedure gives essentially the VLBA result owing to its very high precision, but at QUIN the weighted mean is intermediate between the GPS result and the most recent VLBI result.

3. Results

The GPS velocity data are listed in Tables 1 and 2, and displayed in Figures 2 and 3. Before using these data to assess the rigidity of the Sierra Nevada block or describe its

Table 4. Comparison of OVRO and QUIN Velocities Relative to Stable North America

	Rate, mm/yr	Azimuth, deg W of N	Up, mm/yr
	OVRO		
VLBI[a]	11 ± 1	332 ± 3	--
VLBI[b]	12.0 ± 0.3	316 ± 1	-2.7 ± 0.9
VLBI[c]	10.1 ± 0.5	322 ± 2	--
VLBI[d]	11.7 ± 0.2	323 ± 1	-2.4 ± 0.8
VLBA[d]	10.6 ± 0.1	314 ± 1	-5.9 ± 0.3
GPS[e]	8.7 ± 1.5	313 ± 9	-5.8 ± 3.4
Mean[f]	10.7 ± 0.7	316 ± 5	-5.5 ± 1.4
	QUIN		
VLBI[a]	11 ± 1	310 ± 5	--
VLBI[b]	12.8 ± 0.5	303 ± 2	-4.5 ± 3.6
VLBI[c]	8.9 ± 0.5	294 ± 2	--
VLBI[d]	12.3 ± 0.5	309 ± 2	0.4 ± 3.4
GPS[e]	11.0 ± 0.9	313 ± 4	-4.0 ± 2.2
Mean[f]	11.6 ± 0.9	311 ± 3	-3.6 ± 1.8

[a] *Argus and Gordon* [1991].

[b] *Ma et al.* [1994].

[c] *Dixon et al.* [1995].

[d] *Ma and Ryan* [1998].

[e] This study.

[f] Weighted mean and repeatability of recent independent data: GPS (this study) and VLBI/VLBA data of *Ma and Ryan* [1998], with VLBI/VLBA error scaled up by 2.

present-day motion, we first address the relation between measured GPS velocities and longer-term motions.

3.1. Short-Term Versus Long-Term Velocities

In the discussion below, we assume that the short-term, interseismic site velocities measured by GPS can be related to longer-term geologic motions (e.g., fault slip rates and block motions) that average over many seismic cycles, either directly or through simple mechanical models. There are at least two effects to consider. First, the crust and upper mantle have a postseismic response to stresses released in large earthquakes [*Pollitz and Sacks*, 1992; *Pollitz*, 1997; *Pollitz and Dixon*, 1998]. Time-dependent postseismic effects decrease with time after a major event, and may not be significant after many decades. Large earthquakes on the major faults bounding the Sierra Nevada occurred in 1857 and 1906 on the San Andreas fault, and in 1872 on the Owens Valley fault. The other major process is elastic strain accumulation on and near locked faults, which may reduce the relative velocity of sites across the fault compared to the long-term geologic slip rate. For simple elastic half-space models of strain accumulation [*Savage and Burford*, 1973; *Okada*, 1992], the critical distance is of order 50-100 km for the vertical strike-slip

faults of interest here, several times the 10-15 km thickness of the elastic, brittle upper crust. In this case, "far-field" sites (i.e., those farther than 50-100 km from the fault, which includes most of our Sierran sites), should experience small elastic strain effects, at or below the noise level of the observations (~1 mm/yr). If a simple elastic half-space model applies to the Sierras, our expectation is that most of the measured GPS velocities on the stable block interior should be broadly representative of longer-term motions, since our Sierran sites are located far from active faults and our measurements occurred long after major earthquakes on bounding faults.

However, for a more realistic layered rheology, with an elastic layer overlying viscoelastic material, present-day elastic strain effects due to locked faults may be influenced by past earthquakes, and these effects can extend far from the fault and persist long after the last earthquake, depending on earthquake history, fault depth, and crust and upper mantle rheology [*Savage and Lisowski*, 1998]. This is especially important for kinematic studies of continental blocks with space geodesy, since the smaller size of these blocks compared to larger plates means that it may be difficult to find sites whose velocities are uncontaminated by edge effects. The generally smaller size of continental blocks compared to plates also makes it difficult to obtain geographic "spread" in space geodetic site location, which is important for accurate Euler vector estimation, especially if the block boundaries need to be avoided. Together, these effects may limit accurate Euler vector estimates for continental blocks based on space geodesy, unless accurate site velocities can be defined for the interior of the block, appropriate models are available to "calibrate" the edge effects, and statistical tests are available to evaluate results. The present study takes a first step in addressing these issues.

One way to assess the influence of strain accumulation and earthquake history on the measured site velocities is to compare the Euler vector based on velocities at all the Sierran sites to an Euler vector based on a subset of sites on the block interior likely to be less affected by strain accumulation and earthquakes. If the fit of the velocity data to a rigid block model is significantly improved by elimination of suspect sites, this would suggest that the effects are important, and the resulting Euler vector based on interior sites would presumably be a more accurate representation of long-term Sierra Nevada block motion.

We use the reduced χ^2 statistic to assess the fit of the velocity data to a given rigid block model:

$$\chi^2 = \sum_{i=1}^{2N} \frac{(O_i - C_i)^2}{\sigma_i^2} \Big/ 2N - 3 \qquad (2)$$

where O_i is a velocity observation (north or east), C_i is the calculated velocity at the same site based on a given Euler vector, σ_i is the velocity error, N is the number of sites used in the inversion (5,7, or 8), and $2N-3$ is the number of degrees of freedom (number of sites, with two data points each, minus number of adjustable parameters). The minimum χ^2 indicates the best fit model. Values of reduced χ^2~1.0 indicate a good fit of data to model and suggest that error estimates are reasonable. Reduced
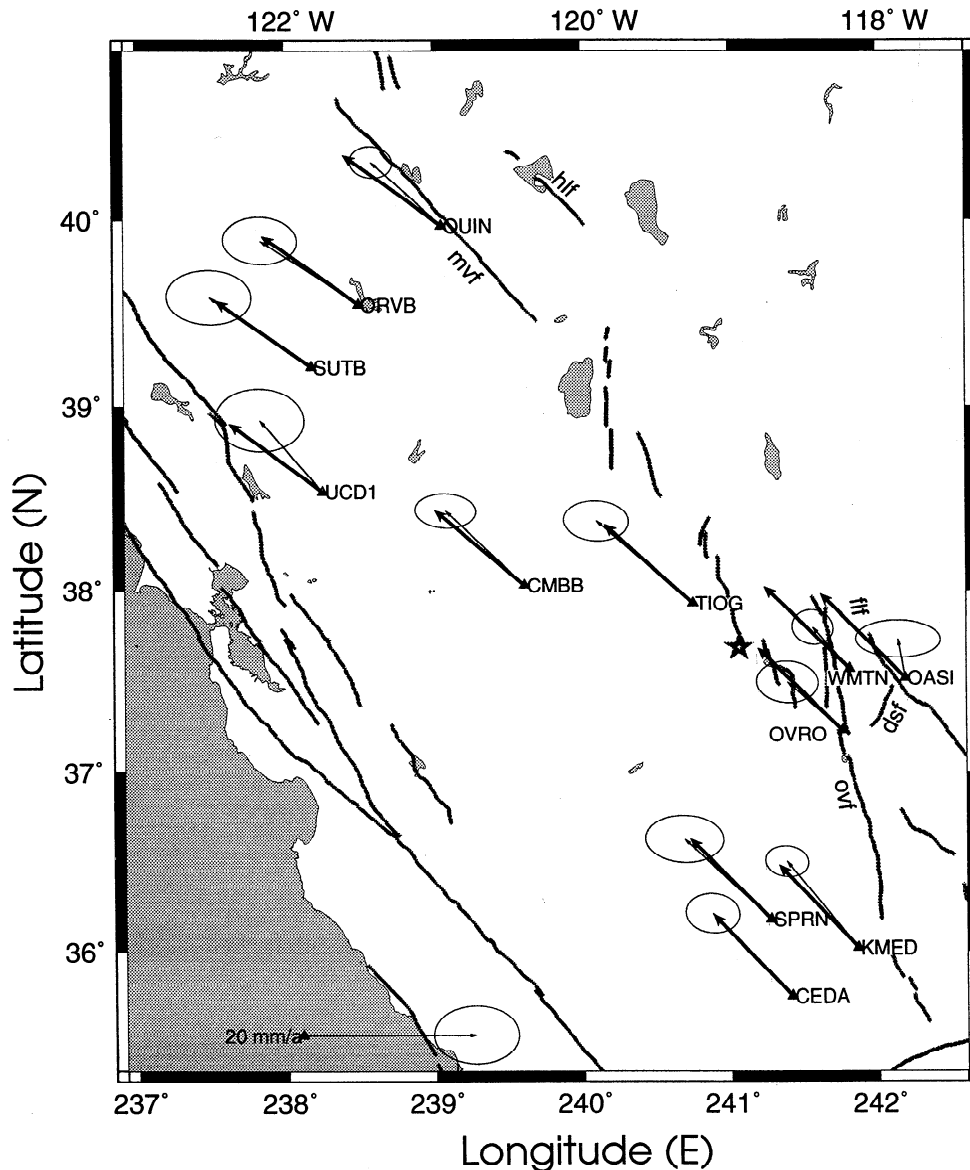
Figure 3. GPS site velocities (arrows) with respect to stable North America (Table 2) and their two-dimensional 95% confidence ellipses. Faults and fault names are same as Figure 1, except dsf, Deep Springs Fault; flf, Fish Lake Valley fault zone. Star shows the location of shallow pressure source at Long Valley Caldera [*Langbein et al.*, 1995b]. Arrows without ellipses show predicted velocities for sites on stable Sierra Nevada block using GPS-based Euler vector in Table 6 (5 station solution). Note that velocities of all sites on the stable block interior fit the predicted velocity within uncertainty ellipse, while sites on the block margin (QUIN, OVRO, WMTN and OASI) do not. WGRD omitted for clarity, ELYA and GFLD are off this map (see Figure 1 for location of these sites).

$\chi^2<1.0$ suggest that errors are overestimated, while reduced $\chi^2>1.0$ suggest either that errors are underestimated or that a given model poorly fits the data. These rules of thumb assume that errors are normally distributed and that sample size is sufficiently large to be statistically representative; neither criteria is particularly well satisfied here, so caution is warranted. Table 6 lists an Euler vector based on the velocities of all 8 sites located on the Sierra Nevada block, with reduced $\chi^2 = 0.44$, indicating that the data fit the rigid

block model quite well and that errors may be overestimated.

For comparison, we also list an Euler vector based on elimination of the three sites most likely to be affected by elastic strain accumulation: TIOG, because it is affected by deformation at Long Valley Caldera and is also close to the Sierra Nevada range front; KMED, because it lies only 18 km west of the Owens Valley fault zone; and UCD1, because it is the closest of the eight sites to the San

Andreas fault, and only ~45 km east of the Green Valley fault, part of the active Calaveras − Concord - Hunting Creek - Bartlett Springs fault system (Figures 1 and 3). An Euler vector describing Sierra Nevada block motion based on the remaining five sites on the stable Sierra Nevada block interior has reduced $\chi^2=0.23$, a factor of 2 improvement compared to the Euler vector based on all 8 sites including ones near the block margins. This suggests that elastic strain effects may be important, may be detectable in our data, and that the Euler vector based on the subset of GPS sites closer to the block interior gives a more reliable estimate of long-term block motion. It also suggests that errors may be overestimated. Reducing average velocity error by a factor of 2 for the five site solution gives reduced $\chi^2 \sim 1.0$. This may reflect the fact that the regressions used to estimate the errors (Table 3) are based on data from across North America, encompassing a wide range of climate zones, soil or bedrock locations, and monument styles. In contrast, most of the Sierran sites are located at high altitude in a dry environment (minimizing tropospheric noise) and set into glaciated bedrock (minimizing ground noise). Given the small number of data (10 versus 16), we cannot preclude the possibility that some of the improvement in fit between the 5 site and 8 site solution is due to chance. Note that the 5 station and 8 station Euler vectors are indistinguishable within uncertainties, suggesting that the magnitude of strain effects is near the error level of our data. This partly reflects the relatively long distance between known active faults and most of our sites (minimizing strain effects), and may also reflect the fact that the strain corrections for the San Andreas fault system and eastern California shear zone are opposite in sign and thus partly cancel.

3.2. Correcting for Elastic Strain Accumulation With a Coupling Model

Given the apparent improvement in fit when sites most likely to be affected by strain accumulation are eliminated, we also investigated strain effects in a more quantitative way, as follows. TIOG is omitted from the calculations, as it may be influenced by deformation at Long Valley Caldera which is time-varying through our measurement period. For the remaining 7 sites, we use the viscoelastic coupling model of *Savage and Lisowski* [1998], with an elastic layer overlying a Maxwell viscoelastic half-space. The elastic layer corresponds to the upper crust, and the viscoelastic half-space corresponds to the more ductile lower crust. The boundary between them, at depth H, corresponds to the lower limit of brittle faulting and the maximum depth of crustal earthquakes, typically 10-15 km. For this model the surface velocity v is

$$v = \sum_{n=1}^{\infty}(b_n/\pi)\left[arctan\{x/((2n-1)H)\} - arctan\{x/((2n+1)H)\}\right] \quad (3a)$$

$$b_{n+1} = b_1(\tau_0{}^n/n!)\sum_{k=0}^{n}n!/[k!(n-k)!]a_{k+1}(t/T)^{n-k} \quad (3b)$$

where x is the horizontal distance from the fault, t is the time since the last earthquake, T is the earthquake recurrence interval, and expressions for a_k are given in the appendix to *Savage and Lisowski*. The time constant τ_0 is related to the earthquake recurrence interval and relaxation time for the viscoelastic half-space, $\tau_0=\mu T/2\eta$, where μ is the rigidity of the half-space (set here to 3×10^{10}Pa), and η is the viscosity (set here to 2×10^{19} Pa-sec). These values for rigidity and viscosity are equivalent to a relaxation time (η/μ) of ~20 years, intermediate among the range of values found by other authors [e.g., *Thatcher*, 1983; *Li and Rice*, 1987]. Each fault segment is assumed to be long and vertical, and local strain effects at the end of fault segments are ignored. Each of the Sierran sites is assumed to be influenced by both the San Andreas fault system to the west and the eastern California shear zone to the east (Figure 1). The direction of velocity increment for these two fault systems is assumed to be parallel to plate motion. Strain effects from the San Andreas system are such that measured Sierran site velocities are mainly faster compared to the long-term average, while strain effects from the eastern California shear zone are such that measured Sierran site velocities are mainly slower than the long-term average. In and north of the San Francisco Bay area we explicitly include the effects of the San Andreas fault (sensu stricto), the Calaveras fault, the Hayward - Rogers Creek - Maacama fault system, and the Concord - Green Valley - Hunting Creek - Bartlett Springs fault system. Effects from the 1989 Loma Prieta earthquake are ignored, as are the effects of creeping sections of faults. For the three southernmost sites only (CEDA, KMED, and SPRN) we also include the effect of the Garlock fault.

We approximate the effects of the eastern California shear zone to the east by considering only the effect of the westernmost fault (i.e., the fault closest to our sites) in the strain accumulation model, and assuming that this fault carries approximately half of the total ~11 mm/yr of slip that needs to be accommodated. For example, south of 37° N latitude, we consider only the Owens Valley fault zone, whose slip rate is taken to be 6 mm/yr. North of 38° N latitude, the main bounding fault or faults for the Sierra Nevada block have not been determined. We assume that one of the main boundary faults follows the band of seismicity that, from south to north, begins near Mono Lake, California, continues northwest near the California-Nevada border to Lake Tahoe, and then continues with a small right step (i.e., Lake Tahoe may be a pull-apart basin) northwest along the Mohawk Valley fault zone [*Goter et al.*, 1994] (Figures 1 and 3). A single throughgoing fault with clear surface expression is not developed in this region, but *Thatcher et al.* [1999] observe a strong gradient in GPS site velocities near here. A change in northwest velocity of ~6-8 mm/yr occurs between the center of the Sierra Nevada block, moving at ~14 mm/yr northwest relative to North America (this study) and the region immediately west of the central Nevada seismic belt, moving at ~6-8 mm/yr northwest relative to North America [*Thatcher et al.*, 1999]. In addition to the Mohawk Valley fault zone, the Honey Lake fault zone (Figure 1) may accommodate part of this motion. *Wills and Borchardt* [1993] estimate a Holocene slip rate of 1.1-2.6 mm/yr for the Honey Lake fault zone

Current tectonics of northern Cascadia from a decade of GPS measurements

Stéphane Mazzotti,[1] Herb Dragert,[1,2] Joseph Henton,[3] Michael Schmidt,[1]
Roy Hyndman,[1,2] Thomas James,[1,2] Yuan Lu,[1] and Michael Craymer[3]

[1]   Global Positioning System (GPS) measurements to study regional deformation were initiated in northern Cascadia in the late 1980s and early 1990s. On the basis of a decade of GPS data, we derive a crustal velocity field for NW Washington-SW British Columbia. The permanent and campaign GPS velocities are defined with respect to North America in the ITRF2000 reference frame. Velocity uncertainties are estimated using a model of time series noise spectra. This new velocity field is the basis for interpretation of the tectonics of the northern Cascadia subduction system. GPS velocities are interpreted in terms of interseismic loading of the megathrust using different coupling models. Our data confirm that the upper part of the megathrust is nearly fully locked. An exponential model for the downdip transition zone gives slightly better agreement with the data compared to the common linear transition. The landward decrease of forearc strain loading is smaller than predicted by any of the current subduction interseismic models. This could be a consequence of a small (0–3 mm/yr) long-term motion of the southern Vancouver Island forearc, with respect to North America, or of a concentration of interseismic strain across the elastically weaker Cascadia volcanic arc. In northern Vancouver Island, our velocity field supports the existence of an independent Explorer microplate currently underthrusting underneath North America, at least up to Brooks Peninsula. Further north, GPS velocities indicate transient and/or permanent deformation of northernmost Vancouver Island related to the interaction with the Explorer microplate and possibly with the Queen Charlotte transform margin.   INDEX TERMS: 1206 Geodesy and Gravity: Crustal movements—interplate (8155); 1242 Geodesy and Gravity: Seismic deformations (7205); 1243 Geodesy and Gravity: Space geodetic surveys; 8123 Tectonophysics: Dynamics, seismotectonics; 8150 Tectonophysics: Plate boundary—general (3040); KEYWORDS: Cascadia, GPS, tectonics

1. Introduction

[2]   Global Positioning System (GPS) measurements to determine crustal strain rates were initiated in the northern Cascadia region (US Pacific Northwest and southwestern British Columbia, Canada) more than a decade ago, with the first campaign measurements in 1986 [*Kleusberg et al.*, 1988] and the establishment of permanent stations in 1991 [*Dragert et al.*, 1995; *Dragert and Hyndman*, 1995]. The permanent networks have since expanded to the current 16 stations of the SW British Columbia Western Canada Deformation Array (WCDA) [*Dragert et al.*, 2001] and 29 stations of the Pacific Northwest Geodetic Array

(PANGA) [*Khazaradze et al.*, 1999; *McCaffrey et al.*, 2000; *Miller et al.*, 2001; *Svarc et al.*, 2002] (Figure 1). In this article, we provide an analysis of a decade of permanent and campaign GPS data obtained for the Canadian portion of northern Cascadia. We processed and analyzed data for all of the continuous stations of the combined WCDA and PANGA networks to obtain an accurate and consistent regional deformation picture of the subduction margin. The velocities have been defined with respect to stable North America within the ITRF2000 realization of the International Terrestrial Reference Frame (ITRF) [*Altamimi et al.*, 2002]. The estimation of meaningful GPS velocity uncertainties is not straight forward, and we discuss several methods for using models of the time series noise spectrum.

[3]   Our new velocity field provides the basis for interpretation of the tectonics and kinematics of the northern end of the Cascadia subduction system and its transition to the Queen Charlotte transform margin. The primary signal in the GPS velocities comes from the interseismic loading of the Cascadia megathrust [e.g., *Savage and Lisowski*, 1991]. We compare the northern Cascadia GPS observations to the predictions of several different models of subduction fault

[1]Pacific Geoscience Centre, Geological Survey of Canada, Sidney, British Columbia, Canada.

[2]Also at School of Earth and Ocean Sciences, University of Victoria, Victoria, British Columbia, Canada.

[3]Gravity and Geodetic Networks Section, Geodetic Survey Division, Ottawa, Ontario, Canada.
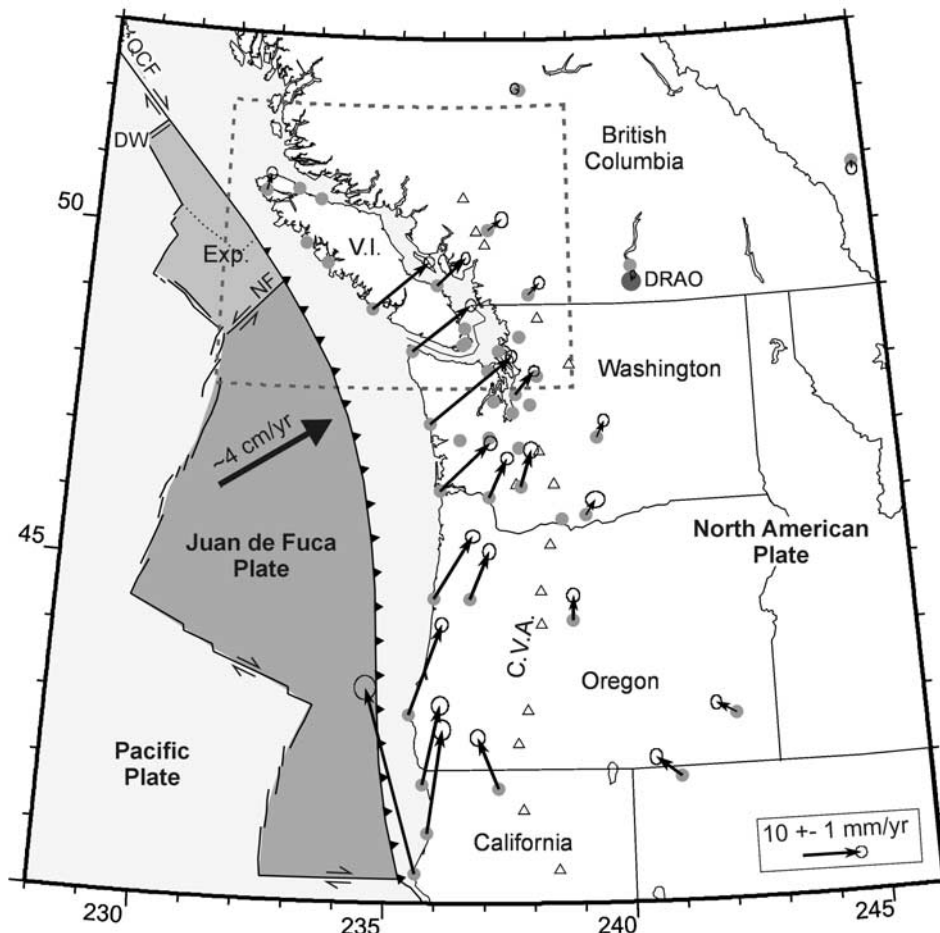
Figure 1. Cascadia permanent GPS network. Gray circles show permanent GPS stations. Reference station DRAO shown as large dark gray circle. Solid arrows show a subset of GPS velocity vectors with respect to stable North America in ITRF2000 (see text). Error ellipses are at 95% confidence level. Juan de Fuca/North America convergence is shown by large black arrow. Open triangles show Cascade Volcanic Arc (CVA) volcanoes. V.I., Vancouver Island; Exp., Explorer microplate; NF, Nootka Fault; DW, Dellwood-Tuzo Wilson Knolls; QCF, Queen Charlotte Fault. Dashed box outlines location of Figure 2.

locking [e.g., *Hyndman and Wang*, 1995; *Wang et al.*, 2003]. The second significant deformation source is the northerly migration and rotation of the Oregon block with respect to North America [*Wells et al.*, 1998; *McCaffrey et al.*, 2000, 2002; *Svarc et al.*, 2002], with a possible extension to NW Washington and Vancouver Island. Off northern Vancouver Island there is a transition from sub-duction to the Queen Charlotte transform fault, including two microplates or deformations zones, the Explorer Plate and the Winona Block [e.g., *Riddihough*, 1977; *Carbotte et al.*, 1989]. We examine the GPS velocity field to test the existence of an independent Explorer microplate currently underthrusting underneath North America up to Brooks Peninsula, and further to the north, the role of the Winona microplate [*Rohr and Furlong*, 1995; *Kreemer et al.*, 1998].

2. GPS Data and Analysis

2.1. Network Description

2.1.1. WCDA and PANGA Permanent Networks

[4] Continuous GPS data in southwestern British Colum-bia and the US Pacific Northwest analyzed at the Pacific Geoscience Centre (Geological Survey of Canada, PGC-GSC) are part of two networks: the Western Canada Deformation Array (WCDA [*Dragert et al.*, 1995]) and the Pacific Northwest Geodetic Array (PANGA [*Miller et al.*, 2001]). The WCDA encompasses 16 stations in SW British Columbia and PANGA 29 stations between northern California and northern Washington (Figure 1). In this study, we processed the two networks jointly to provide consistent results for tectonic interpretation of the Cascadia margin. Most of the GPS sites correspond to geodetic monuments, with a forced-centered antenna mounted on a concrete or steel pillar (see http://www.pgc.nrcan.gc.ca/geodyn/wcda/monument.html), or on a steel tripod anchored into bedrock (see http://www.geodesy.cwu.edu/). Exceptions to this rule are the sites from the US Coast Guard GPS network, which have antennas mounted on transmission towers or roofs and may be less stable. Stations are instrumented with dual frequency L1/L2 GPS receivers and antennas from various companies (Ashtech, Trimble, AOA). Most antennas have a ''choke ring'' design to reduce multipath noise and are equipped with a weather dome.

Table 1a. WCDA-PANGA Permanent Station Velocities

Station	Latitude °N	Longitude °E	V_n,[a] mm/yr	σ_n,[b] mm/yr	RMS,[c] mm	V_e,[a] mm/yr	σ_e,[b] mm/yr	RMS,[c] mm	V_u,[a] mm/yr	σ_u,[b] mm/yr	RMS,[c] mm	T,[d] years
ALBH	48.39	236.51	4.5	0.5	1.4	5.0	0.5	2.0	−0.1	1.0	4.4	6.6
BCOV	50.54	233.16	5.0	0.9	1.4	1.1	0.9	1.6	5.2	2.7	4.9	1.8
BLYN	48.02	237.07	3.8	2.8	3.5	5.5	4.8	6.0	−112.4	18.4	23.0	1.1
BURN	42.78	242.16	1.9	0.6	1.5	−3.4	0.5	1.2	−2.0	1.9	5.5	3.4
CABL	42.84	235.44	15.5	0.6	1.5	5.5	0.5	1.5	0.8	2.0	5.8	3.4
CHWK	49.16	237.99	2.0	0.5	1.2	2.0	0.5	1.2	1.7	1.4	4.4	3.7
CME1	40.44	235.60	31.8	1.1	2.9	−8.8	0.9	2.6	0.0	2.8	8.1	3.4
CORV	44.59	236.70	8.2	0.7	1.7	3.2	0.5	1.6	0.7	1.9	5.6	3.4
CPXF	46.84	237.74	4.9	0.9	1.2	4.9	0.8	1.2	1.0	3.0	4.4	1.4
DRAO	49.32	240.38	1.1	0.4	1.3	0.3	0.2	1.7	0.8	0.3	5.3	6.6
ELIZ	49.87	232.88	5.6	0.8	1.3	3.9	0.9	1.6	6.2	2.7	4.1	2.0
ESQM	48.43	236.57	3.7	0.7	2.0	2.3	0.7	2.0	1.4	1.8	6.8	2.4
FTS1	46.21	236.04	8.2	0.6	1.7	8.5	0.5	2.4	−0.9	1.6	4.9	6.3
GOBS	45.84	239.19	2.6	0.7	2.4	1.7	0.8	3.0	−1.6	1.7	5.8	3.4
GWEN	45.78	238.67	2.6	0.7	1.7	1.9	0.8	2.0	0.5	1.5	6.1	5.0
HOLB	50.64	231.87	2.8	0.5	2.3	0.7	0.5	2.3	2.2	1.4	5.7	6.6
JRO1	46.28	237.78	6.2	0.7	1.5	1.9	0.6	1.9	−0.6	1.5	5.6	5.0
KELS	46.12	237.10	6.6	0.5	1.4	3.0	0.5	1.2	1.2	1.6	4.4	4.6
LIND	47.00	239.46	2.8	0.5	1.4	1.3	0.5	1.3	1.3	1.6	5.1	3.7
LKCP	47.94	238.17	3.1	1.1	1.3	3.5	1.1	1.4	−1.1	5.9	7.4	1.1
NANO	49.30	235.91	4.7	0.5	1.6	4.8	0.4	1.5	1.7	1.1	4.8	6.6
NEAH	48.30	235.38	8.0	0.5	1.7	9.8	0.5	1.9	2.8	1.2	5.3	6.6
NEWP	44.59	235.94	10.7	0.5	1.3	6.5	0.6	1.8	1.4	1.8	5.2	3.4
NTKA	49.59	233.38	7.8	0.8	1.3	7.8	0.8	1.6	5.4	2.5	4.9	2.0
PABH	47.21	235.80	11.6	0.5	1.4	13.7	0.5	1.4	0.0	1.3	4.8	4.9
PGC4	48.65	236.55	4.8	0.7	1.5	4.3	0.8	2.0	2.8	1.7	4.4	2.9
PRDS	50.87	245.71	−1.4	0.5	1.5	0.0	0.5	1.5	0.8	1.4	5.1	4.9
PTHY	50.69	232.63	4.2	1.2	1.5	−0.4	1.3	1.8	2.8	4.8	6.8	1.3
PTSG	41.78	235.75	13.6	0.8	1.6	2.9	0.7	1.6	5.3	2.5	6.1	2.6
PUPU	47.50	237.99	4.9	1.3	1.5	2.2	1.0	1.2	5.4	5.1	6.4	1.1
REDM	44.26	238.85	4.2	0.6	1.4	0.2	0.5	1.4	0.1	1.6	4.6	3.4
RPT1	47.39	237.63	4.0	0.5	1.8	2.8	0.5	2.1	−1.4	1.2	5.3	6.4
SATS	46.97	236.46	8.1	0.6	1.8	5.9	0.6	2.1	1.6	1.5	5.8	5.1
SC00	46.95	239.28	2.6	1.0	1.3	0.6	1.0	1.5	−0.8	3.3	4.9	1.3
SEAT	47.65	237.69	4.0	0.5	1.4	3.2	0.5	1.9	−0.6	1.0	4.7	6.6
SEDR	48.52	237.78	2.8	0.5	1.2	2.5	0.5	1.5	−0.6	1.3	4.7	4.8
SHLD	41.87	240.98	3.4	0.7	1.4	−4.3	0.5	1.3	1.5	2.4	5.8	2.6
SMLD	49.57	240.36	1.4	0.6	1.1	0.3	0.5	1.0	0.4	1.6	3.5	2.2
TRND	41.05	235.85	17.7	0.9	1.9	2.4	0.7	1.7	1.0	2.7	6.4	2.5
TWHL	47.02	237.08	8.6	2.4	3.6	8.7	3.3	4.9	−0.6	6.6	9.8	1.4
UCLU	48.93	234.46	8.2	0.5	1.5	9.3	0.5	1.7	2.0	1.1	5.0	6.6
WHD1	48.31	237.30	5.0	0.8	3.1	4.0	0.7	3.3	−5.1	1.6	7.1	6.4
WILL	52.24	237.83	0.3	0.5	1.4	−0.6	0.4	1.2	2.0	0.9	3.9	6.6
WSLR	50.13	237.08	1.9	0.7	2.6	2.3	0.5	2.0	1.7	1.7	7.1	5.9
YBHB	41.73	237.29	8.8	0.7	1.9	−3.6	0.6	1.9	2.4	2.3	6.8	3.4

[a]Velocity in north, east, and up components.
[b]Modeled uncertainty on north, east, and up velocity components.
[c]Root-mean-square of daily scatter of position in north, east, and up components.
[d]Duration of position time series analyzed.

[5] We have processed the data from the permanent stations from January 1996 to August 2002, ensuring an almost 7-year time series for the few stations that were set up before 1996 (Table 1). The average time span of GPS time series in the continuous networks is 3.9 years with a minimum of 1.1 year and a maximum of 6.6 years.

2.1.2. Vancouver Island Campaign Networks

[6] Four geodetic networks on Vancouver Island comprise 67 sites that were surveyed twice by the Geodetic Survey Division (Natural Resources Canada) with campaign-style GPS occupations during the 1991–1994 and 1996–1999 periods (Figure 2). They usually provide lower accuracy velocities, compared to permanent stations, but allow a greater spatial resolution. Data acquisition method, equipment type, and other parameters (e.g., orbits, frame) vary significantly from one survey to another and from one

period to another. However, owing to the large time span (5–6 years) between occupations, the estimated velocities are both spatially coherent and consistent with the nearby permanent stations within the uncertainties.

[7] The Juan de Fuca, Port Alberni, and Central Vancouver Island networks were processed as part of the Ph.D. thesis of Joseph Henton at the University of Victoria and PGC-GSC (see *Henton* [2000] and *Henton et al.* [1999, 2000] for details). The Queen Charlotte Strait network was recently processed at PGC-GSC as part of this study. The Juan de Fuca network is composed of 15 sites in southern Vancouver Island, in the Gulf Islands, and Lower Mainland, BC. The sites were first surveyed in October 1991 and resurveyed in August 1996, with 2–6 occupations of 5–7 hours. The Port Alberni network consists of 21 sites located along a ~50 km wide SW-NE profile running from

Table 1b. Campaign GPS Site Velocities

Site	Latitude	Longitude	V_n,[a]	σ_n,[b]	V_e,[a]	σ_e,[b]	Net,[c]	T,[d] years
ATKI	49.34	236.75	4.0	1.3	4.6	1.5	JdF	4.8
BEEC	48.32	236.35	4.8	0.9	4.9	1.0	JdF	4.8
BONI	48.60	235.28	8.6	1.4	6.2	1.9	JdF	4.8
BOUN	49.08	237.00	4.0	1.2	2.5	1.5	JdF	4.8
CHEM	48.92	236.30	4.9	1.1	4.0	1.2	JdF	4.8
CONS	48.47	236.33	5.1	1.0	4.9	1.1	JdF	4.8
DISC	48.43	236.77	5.2	0.9	2.9	1.3	JdF	4.8
DOUG	48.49	236.65	4.5	0.8	4.6	1.0	JdF	4.8
GABR	49.20	236.18	4.1	3.1	3.2	1.1	JdF	4.8
JORD	48.47	235.90	5.2	1.0	5.2	1.1	JdF	4.8
LAZA	48.61	236.18	5.1	0.9	4.7	1.0	JdF	4.8
RENF	48.56	235.60	6.5	1.3	6.0	1.5	JdF	4.8
SATU	48.78	236.83	3.4	1.2	2.7	1.4	JdF	4.8
SHER	48.38	236.08	5.1	0.9	6.4	1.1	JdF	4.8
YOUB	48.90	235.74	5.9	1.1	4.7	1.3	JdF	4.8
ANDE	49.20	234.97	7.9	1.2	6.8	1.6	PAL	5.1
ARRO	49.22	235.41	6.2	1.2	5.9	1.6	PAL	5.1
FOUR	49.19	234.72	6.5	1.2	5.8	0.9	PAL	5.1
GREY	49.00	235.30	7.0	1.2	6.3	0.9	PAL	5.1
HAND	49.07	235.04	6.4	1.2	5.8	0.9	PAL	5.1
PATL	49.14	235.29	7.8	1.2	6.7	1.6	PAL	5.1
JOAN	49.42	235.08	5.8	1.2	4.7	1.6	PAL	5.1
MARK	49.36	235.27	5.9	1.2	4.0	1.6	PAL	5.1
OKAY	49.23	235.74	5.3	0.7	4.2	0.9	PAL	5.1
BALL	49.35	235.84	5.8	1.2	3.5	1.6	PAL	5.1
TOBY	49.49	235.34	6.1	1.2	4.4	0.9	PAL	5.1
FRED	48.99	234.49	9.2	1.2	8.6	0.9	PAL	5.1
PACH	48.87	234.96	7.5	1.2	7.4	0.9	PAL	5.1
RADA	49.08	234.16	7.2	1.2	8.0	1.6	PAL	5.1
BAMF	48.83	234.87	7.3	1.8	8.0	1.6	PAL	5.1
DAVI	49.60	235.68	5.7	1.2	3.7	0.9	PAL	5.1
SECH	49.60	236.12	4.7	1.2	2.5	0.9	PAL	5.1
SHEP	49.54	235.81	5.0	1.2	3.7	0.9	PAL	5.1
EARL	49.75	236.02	5.0	1.2	2.9	1.6	PAL	5.1
POCA	49.71	235.55	5.1	1.2	2.8	1.6	PAL	5.1
POWE	49.81	235.54	4.6	1.2	3.2	1.6	PAL	5.1
ALEX	49.74	234.51	5.2	1.2	5.2	1.2	CVI	5.1
BCHR	49.65	234.78	3.0	1.6	5.9	1.2	CVI	5.1
GLAC	49.55	234.64	4.0	1.6	6.3	1.2	CVI	5.1
OYST	49.82	234.60	3.7	0.8	3.9	0.8	CVI	5.1
ANAW	49.79	233.45	4.8	1.2	3.7	1.5	CVI	5.1
FILB	49.88	234.30	2.9	0.8	2.7	1.2	CVI	5.1
PIER	49.62	233.88	4.1	1.2	5.1	1.5	CVI	5.1
SENT	49.96	234.04	2.6	1.2	1.9	1.5	CVI	5.1
STRA	50.00	234.42	3.1	0.8	2.4	0.8	CVI	5.1
MOAK	50.10	233.94	2.9	1.2	4.2	1.2	CVI	5.1
ANNA	50.49	234.69	2.1	1.2	2.3	1.2	CVI	5.1
BREW	50.13	234.36	4.3	1.6	5.7	2.6	CVI	5.1
HART	50.03	234.60	2.8	0.8	3.9	0.8	CVI	5.1
HKUS	50.34	234.16	3.6	1.6	2.5	1.2	CVI	5.1
MENZ	50.23	234.50	3.7	1.6	2.1	1.5	CVI	5.1
NACH	49.95	235.00	4.3	1.2	2.4	1.2	CVI	5.1
WASH	49.75	234.70	3.6	1.2	3.0	1.2	CVI	5.1
ALIC	50.46	232.48	2.3	1.1	0.4	0.9	QCS	6.0
BULL	50.96	232.89	3.5	1.3	−0.3	1.2	QCS	6.0
CALV	51.54	232.05	−0.4	1.3	−1.7	1.2	QCS	6.0
COXI	50.81	231.40	2.2	1.3	0.5	1.2	QCS	6.0
HARD	50.70	232.62	0.8	1.4	0.5	1.1	QCS	6.0
JENS	50.65	231.74	1.7	1.3	−1.1	1.2	QCS	6.0
KING	51.85	232.23	1.0	1.3	−2.9	1.2	QCS	6.0
KLUC	50.57	232.84	3.3	1.3	2.1	1.7	QCS	6.0
KOPR	50.49	232.10	1.4	2.2	3.0	1.3	QCS	6.0
ROBI	51.19	232.40	1.4	0.5	−1.1	1.4	QCS	6.0
SCAR	50.65	231.99	0.8	1.2	1.2	0.9	QCS	6.0
SEYM	51.47	232.72	1.9	1.3	0.4	1.2	QCS	6.0
SHUS	50.78	232.19	2.7	1.3	−0.2	1.2	QCS	6.0
SPAT	50.68	231.67	3.9	1.3	0.3	1.2	QCS	6.0

[a]Velocity in north and east components.
[b]Uncertainty on north and east velocity components.
[c]Campaign network: JdF, Juan de Fuca; PAL, Port Alberni; CVI, Central Vancouver Island; QCS, Queen Charlotte Strait (see text).
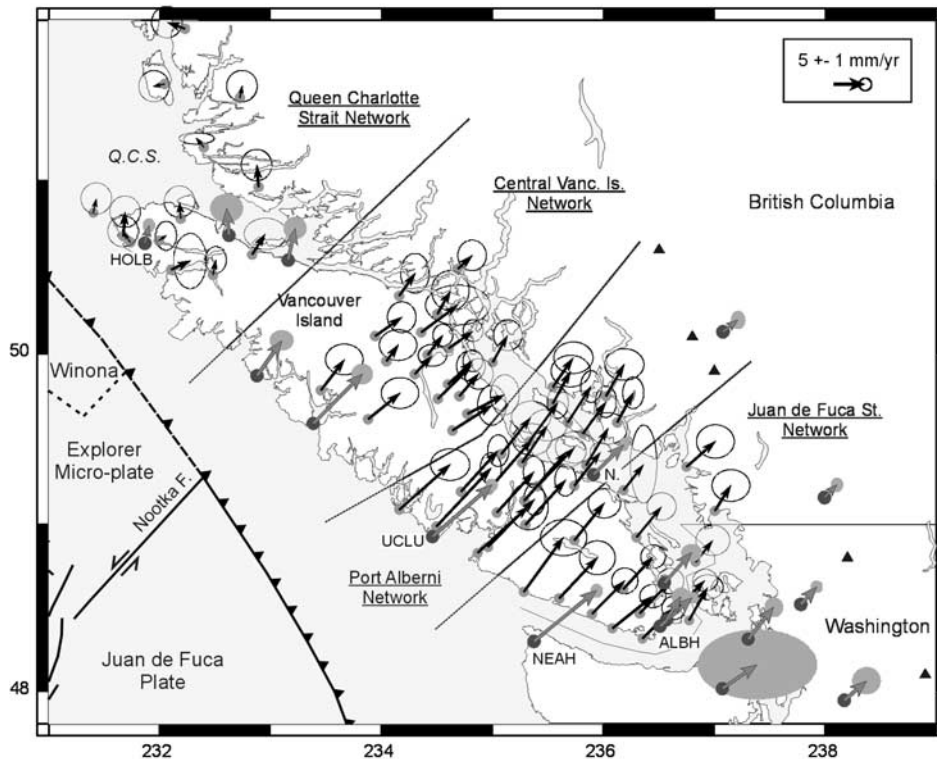[d]Time span between the first and second surveys.

Figure 2. Northern Cascadia continuous and campaign GPS velocities. Thin solid and large gray arrows show horizontal velocities at campaign and continuous GPS sites with respect to stable North America in ITRF2000. Error ellipses are at 95% confidence level. Campaign GPS networks (underlined labels) are separated by thin dashed lines. Q.C.S., Queen Charlotte Strait; Nootka F., Nootka Transform Fault.

the west coast of Vancouver Island to the mainland. It was surveyed in June 1994 with 2–5 occupations of ∼6.5 hours and in July 1999 with 2–4 occupations of 4–24 hours. The Central Vancouver Island network consists of 17 sites located between UCLU, NTKA, and the B.C. mainland. The sites were surveyed in July/August 1992 and September 1997 with 2–5 occupations of ∼5.5 hours and 4–24 hours, respectively. During the first occupation, the GPS data were affected by testing of antispoofing, leading to increased noise and possible biases in the 1992 network solution. The Queen Charlotte Strait network comprises 14 sites in northernmost Vancouver Island, across the strait on the mainland, and along the Inside Passage. The sites were occupied in July 1993 and in July/August 1999. The first survey was characterized by 2–10 occupations of only 1–4 hours each. For the second survey, sites were occupied 2–6 times for 22–24 hours.

2.2. Processing and Time Series Analysis

[8] The main GPS data processing features are described for the continuous station network. Minor differences in the processing of the campaign data are also described. We carried out the processing at PGC-GSC using the BERNESE 4.2 software [*Hugentobler et al.*, 2001] and the following techniques:

[9] 1. Daily positions are computed using an ionospheric-free, double-difference, phase solution, with station DRAO (Penticton, BC, Figure 1) held as a fixed reference station.

[10] 2. Precise satellite orbits and Earth rotation parameters from the International GPS Service (IGS) are used and

held fixed. SIO/SOPAC satellite orbits are used for the campaign data acquired prior to 1994.

[11] 3. Data are sampled at 30 s.

[12] 4. Ocean tide loading corrections are applied using the LOADSTP software [*Pagiatakis*, 1992], which incorporates the FES95.2 global ocean tide model [*Le Provost et al.*, 1998].

[13] 5. Ambiguities are resolved by constraining a regional ionospheric model ("quasi-ionosphere-free" strategy).

[14] 6. Tropospheric delay corrections are applied using Dry Niell mapping function [*Niell*, 1996] with 24 zenith delay estimates and 4 gradient parameter estimates per 24-hour session.

[15] 7. A priori coordinates of the stations are either defined as their ITRF97 epoch 1998.0 value, or as the value derived by a preliminary processing for stations that are not in the ITRF97 solution.

[16] 8. Changes in antenna models, antenna heights, and phase center corrections are accounted for using IGS phase center calibrations.

[17] We introduced minor differences during the processing of the campaign data, essentially to stabilize the results on some of the short occupation surveys and to ensure a strong tie to the continuous network solution. Depending on the time period, available nearby permanent stations were included in the campaign data analysis and constrained tightly to positions derived from the continuous network analysis (see *Henton* [2000] for details). For the Queen Charlotte Strait network, we used nearby station HOLB

(Holberg, northern Vancouver Island, see Figure 2) as the fixed reference, instead of the more distant DRAO. Tropospheric gradient estimation was turned off because the very short occupations during the first survey did not allow their separation from other parameters.

[18] For the continuous network, we inverted independently the north, east, and up components of the station time series (position u change with time t), using least mean squares regression to constrain the parametric relation:

$$u(t) = a + bt + c\cos(365.25t + \phi) + [k_1 t_1 + .. + k_i t_i]$$

where a is the intercept, b is the rate of change (velocity) assumed to be constant through time, c and ϕ are the amplitude and phase of a 365.25 day seasonal variation, and k_j is the amplitude of an instantaneous offset at time t_j associated with a change of antenna or dome, or with a large earthquake (e.g., the 2001 Nisqually earthquake).

[19] We obtained the best fit model for the regression parameters through an iterative technique. First, obvious large outliers were eliminated and offsets at all identified times of "disruptions" were estimated. Outlier rejection was then further refined by the removal of data points for which the residual difference from the initial parametric model exceeded three times the standard error of the model fit. Next, each offset estimate that had a magnitude smaller than three times its formal regression error was deemed to be not statistically significant and removed. This removal was done for one offset parameter at a time, with new regressions providing revised estimates for all remaining parameters. This process was repeated until only statistically significant offset estimates remain in the regression.

[20] The discovery of ∼2 weeks transient signal in the GPS time series associated with slow slip events [Dragert et al., 2001, 2002] adds an extra level of complication in the modeling of the GPS data to extract long-term rates (significant over several years). The slow slip deformation can be treated in one of two ways: (1) Offsets are introduced at the time of each slow slip event (assuming an instantaneous step) in order to estimate the average velocity of the GPS station between slip events; and (2) no offset is allowed for at the time of the slow slips. Under this scenario, slow-slip events are regarded as short-term perturbations with their own strain loading/release process and make no net contribution to the long-term deformation velocities over a few cycles. We used this second option to estimate the GPS long-term velocities. The assumption of a null deformation budget associated with slow slip events implies that long-term velocities estimated at GPS sites located in the region of the slow slip events and with short (less than 3–4 years) time series are susceptible to a significant bias (up to 1–2 mm/yr).

[21] For the campaign measurements, we estimated the long-term velocity at each site assuming a constant rate between the network surveys. The site velocity corresponds to the weighted best fit linear rate between the daily positions of the two occupations. Because the campaign networks rely on two surveys with a few days of data, seasonal signals and potential offsets could not be estimated. These limitations are considered in the uncertainty budget of the campaign data.

2.3. Estimation of Uncertainties

[22] Studies of the spectral component of GPS time series suggest the noise may be described using a frequency-dependent model with a spectral index between 0.5 and 2. [e.g., Zhang et al., 1997; Mao et al., 1999]. On the basis of the analysis of 3-year-long GPS data, Mao et al. [1999] derived an empirical model to describe the noise as function of white (σ_W), flicker (σ_F), and random walk (σ_R) components:

$$\sigma_M^2 \cong (12\sigma_W^2)/(gT^3) + (1.78\sigma_F^2)/(g^{0.22}T^2) + (\sigma_R^2)/(T)$$

where g and T are the number of observations per year and the time series length. They estimated the amplitude of the white and flicker noise at 23 global stations and concluded that uncertainties in GPS velocities might be underestimated by factors of 5–11 if pure white noise is assumed.

[23] These results have been adopted by many researchers to describe the uncertainties on GPS velocities (e.g., Dixon et al. [2000] for California, Miyazaki and Heki [2001] for Japan, Miller et al. [2001] for Cascadia, and Sella et al. [2002] for global). Variations, however, exist in the implementation of this error model. In particular, the random walk component is frequently neglected, on the basis that it should only become significant for long (4–5 years and more) time series. The amplitude of each noise component can be derived from geographical averages provided by Mao et al. [1999]. An alternative, and fairly common, approach consists in exploiting the correlation between these noise parameters and the weighted root-mean square (WRMS) of daily scatter of individual time series. Empirical scaling laws are then derived that provide the amplitude of the white and flicker noise component as a function of the WRMS [Dixon et al., 2000; Miller et al., 2001].

[24] With no colored noise assumption, the formal standard deviation on velocities derived from our continuous station time series are too optimistic (0.0–0.9 mm/yr in the horizontal components and 0.1–3.1 mm/yr in the vertical component) and do not show any significant decrease with the length of the time series. Thus we adopt the empirical error model defined by Mao et al. [1999], using the following simple first order scaling factors between the time series WRMS and the different noise components:

White noise $\sigma_W \cong 0.7$ WRMS

Flicker noise $\sigma_F \cong 1.0$ WRMS

Random walk $\sigma_R \cong 0.5$ WRMS

[25] We derived these scaling factors from a comparison of WRMS and noise amplitude for North America GPS studies [Mao et al., 1999; Dixon et al., 2000; Miller et al., 2001]. The first two expressions give a reasonable fit to Mao et al.'s data (within ∼0.5 mm/yr). The third expression gives mean σ_R values of 0.9, 1.0, and 3.0 mm/yr$^{1/2}$ in the north, east, and up components, respectively (range of 0.6–1.8, 0.5–3.0, and 1.8–11.0 mm/yr$^{1/2}$). These numbers are in reasonable agreement with the estimates of Langbein and Johnson [1997], based on 10 yearlong trilateration time series (σ_R range between 0.5 and 3 mm/yr$^{1/2}$).

Table 2. Uncertainty Scaling Factor[a]

	JdF	PAL	CVI
North	2.7	4.0	1.9
East	4.9	3.1	2.0

[a]JdF, Juan de Fuca network; PAL, Port Alberni network; CVI, central Vancouver Island network.

[26] Given these noise parameters, the estimated uncertainties for the permanent station velocities vary, in the horizontal components, between ~1–1.5 mm/yr for 1 year time series and ~0.5 mm/yr for 5 year and longer time series. The vertical component shows uncertainties that range between ~5 mm/yr and ~1.5 mm/yr for the same respective time spans (see Table 1).

[27] The formal standard error derived from the inversion of the position time series for the campaign data is also too optimistic (~0.4 mm/yr on average) to properly describe the uncertainties on velocities. The actual uncertainties on the campaign velocities should reflect sources of error inherent to campaign GPS and not easily detected because of the few observations. Four potential error sources are considered that lead to an error budget of ~1.2 mm/yr:

[28] 1. Slow slips events can lead to potential biases in the estimated position of as much as 3–5 mm for affected sites [*Dragert et al.*, 2001]. These nearly periodic events are superimposed on the long-term rate. Because of the small permanent GPS coverage prior to 1996, the spatial extent and amplitude of pre-1996 slow slip events is not well constrained [*Dragert et al.*, 2002], thus precluding a correction of pre-1996 campaign surveys. This possible position bias translates into a potential error of 0.5–1.0 mm/yr in the estimated velocity over a 5–6 years time series.

[29] 2. Continuous time series show that changes of antenna type, dome, or skirt, at the reference station can affect the estimation of position of other stations by up to 10 mm in the vertical component. The effect appears to be insignificant (~0.5 ± 0.5 mm) in the horizontal component.

[30] 3. As shown in permanent station analysis, a change of antenna at campaign sites can add a nonmodeled offset of up to 20–30 mm in the vertical component and a few mm in the horizontal. Over a 4–6 years period, this translates into an uncertainty on the horizontal velocity of ~0.5 mm/yr.

[31] 4. The main characteristic of campaign survey is the repeated set up of the GPS antenna over a marker. An overall uncertainty of ~1 mm in the horizontal components is estimated due to the set up variations and tripod deformation during the surveys. For two occupations over 4–6 years, this suggests an uncertainty of 0.3–0.5 mm/yr.

[32] Alternatively, the uncertainties in the campaign velocities can be estimated using the same method as for the permanent network solution: i.e., an error model including white, flicker, and random walk noise [*Mao et al.*, 1999], and WRMS of the daily scatter used to scale the different noise component amplitudes. However, time series with only 1 or 2 occupations during two surveys do not provide a significant estimate of the WRMS. Thus we estimated the uncertainties on the campaign velocities by directly scaling the formal standard errors with empirical constants (Table 2) such that the horizontal uncertainty averaged about 1.2 mm/yr for each network.

2.4. Adjustment to ITRF2000 and North America

[33] The analysis of the derived position time series allows high accuracy estimation of station velocities with respect to the reference station [cf. *Dragert et al.*, 2001]. However, this procedure has some disadvantages over the free-network adjustment strategy, mostly because our fixed reference-station strategy does not allow for a possible motion of the reference station DRAO within the analysis reference frame. Three issues arise when our rates are used for comparison with other studies or with various crustal deformation models:

[34] 1. Our reference station DRAO likely has a small velocity with respect to stable North America (up to 2 mm/yr roughly northeastward [e.g., *Miller et al.*, 2001]).

[35] 2. A slight network distortion is induced during the processing by fixing a reference station that has a large velocity (~17 mm/yr) in the ITRF reference frame (frame used for the definition of the GPS satellite orbits). This distortion increases linearly with the distance to the reference station, from ~0.1 mm/yr at 500 km to ~0.3 mm/yr at 1000 km in the horizontal components, and from ~0.6 mm/yr to ~1.2 mm/yr for similar distances in the vertical component.

[36] 3. The original velocities are not attached to any particular ITRF realization.

[37] To account for these biases, we derived an empirical procedure that allows mapping the original velocities into a given ITRF realization and a given stable North America reference. We map GPS velocities into the ITRF2000 realization [*Altamimi et al.*, 2002], which is the most recent and most robust realization of the ITRF. We use empirical transfer functions that describe the effect on the velocity of every station due to the motion of the reference station (DRAO). The network adjustment to ITRF2000 is estimated by solving for the velocity of DRAO that minimizes the difference in horizontal and vertical velocities for a subset of 14 common stations between our solution and the ITRF2000 solution. The best fit DRAO velocity agrees with the velocity from the ITRF2000 solution within 0.6 mm/yr (Table 3). The velocities for the continuous and campaign networks are then mapped into ITRF2000 by propagating the velocity of DRAO, and the associated uncertainties, to the other stations.

[38] There is a significant difference of ~2 mm/yr between the velocity of DRAO in ITRF2000 and in ITRF97 (Table 3). A similar difference is found for ALBH and WILL (the only well constrained Cascadia stations in ITRF97 solution). Because these three stations have long time series (~7 years) and are among the core ITRF sites, this difference probably reflects an actual variation in the ITRF realization, rather than fluctuation of these partic-

Table 3. DRAO Velocity in ITRF

	$V_n \pm \sigma_n$[c]	$V_e \pm \sigma_e$[c]	$V_u \pm \sigma_u$[c]
ITRF2000 adjustment[a]	−11.7 ± 0.3	−14.0 ± 0.1	0.8 ± 0.3
ITRF2000 solution[b]	−11.7 ± 0.5	−13.4 ± 0.3	1.2 ± 0.5
ITRF97 solution[b]	−13.2 ± 0.5	−12.6 ± 0.4	0.5 ± 0.6

[a]Adjustment of 14 permanent common stations and ITRF2000.
[b]Nominal ITRF2000 and ITRF97 solutions.
[c]Velocity and standard error (1σ) in north, east, and up components in mm/yr.

Table 4. Predicted Velocities for Different NA/ITRF Rotation Vectors

Location	Penticton		Holberg		Cape Mendocino	
	V_n	V_e	V_n	V_e	V_n	V_e
ITRF2000[a]	−12.8	−14.3	−15.2	−13.0	−14.2	−11.9
ITRF97[b]	−14.0	−12.2	−16.3	−10.8	−15.3	−9.5
ITRF96[c]	−13.7	−12.7	−16.0	−11.2	−15.0	−10.1

[a]After *Altamimi et al.* [2002].
[b]After *Svarc et al.* [2002].
[c]After *DeMets and Dixon* [1999]. North and east velocities in mm/yr.

ular stations. Our solution mapped in ITRF97 would thus be significantly different from our preferred ITRF2000 solution.

[39] Because the Queen Charlotte Strait campaign network was processed with respect to station HOLB, the adjustment of the velocities to ITRF2000 is done in a similar way as for the other networks, but using the ITRF2000 velocity of HOLB rather than that of DRAO.

[40] The continuous and campaign solutions, mapped into ITRF2000, are then transformed into solutions with respect to stable North America (NA) by removing the predicted velocity at each station associated with a given NA/ITRF2000 rotation vector. Various NA/ITRF rotation vectors exist that reflect the different realizations of the ITRF and the numerous solutions for North America scale GPS networks. Although they all agree to a first order, small differences arise that feed into the predicted motion of North American sites (Table 4). In order to be consistent with the choice of the ITRF2000 as a reference frame, we use the NA/ITRF2000 rotation vector as defined by *Altamimi et al.* [2002] for transformation to North America reference. This rotation vector is based on velocities of 16 stations in stable North America, directly derived from the ITRF2000 solution, and thus includes a combination of GPS, VLBI, and SLR rates.

[41] The NA/ITRF2000 vector used is $-5.04 \pm 1.14°$N, $276.86 \pm 1.95°$E, $-0.194 \pm 0.003°$/Myr (latitude, longitude, rotation rate positive counterclockwise). The uncertainties are formally propagated to the final velocities (uncertainties on this rotation vector correspond to uncertainties on velocities at sites in Cascadia of $\sim$0.1–0.3 mm/yr). The final horizontal velocity field for northern Cascadia is shown on Figure 2.

2.5. Consistency Between the Campaign and Permanent Solutions

[42] The consistency between the solutions for the different campaign networks and the permanent networks can be estimated by comparing the velocities of nearby campaign and permanent sites. The combined campaign-continuous velocity field shows good agreement between the elements of this combination, both in magnitude and direction of the velocity vectors (Figure 2). However, there are suggestions of small systematic differences among the survey networks:

[43] Of the four campaign networks, the Juan de Fuca network shows the best agreement with the permanent solution. This is likely due to the fact that it is the only campaign network constrained by surrounding permanent stations during both surveys.

[44] There is an indication for a small (5–10°) counter-clockwise rotation of velocities for inland sites of the Port Alberni network, compared to the Juan de Fuca and to the UCLU and NANO velocities.

[45] The internal scatter in the solution for the Central Vancouver Island network is slightly larger than that for the two other campaign networks on southern Vancouver Island. This larger scatter may be related to the testing of antispoofing on GPS signal during the 1992 survey.

[46] For the Queen Charlotte Strait network, where both ALBH and DRAO stations were processed and analyzed in the campaign-style mode, the campaign velocities derived for those two stations agree with the permanent solution at the 95% confidence level, with differences of 1.1 and 0.5 mm/yr, respectively. These comparisons indicate that there is an overall agreement between the campaign solutions and the continuous solution. In most cases, this agreement is better than 1 mm/yr, with some discrepancies up to 2–3 mm/yr.

3. Southern to Central Vancouver Island: Subduction Regime

3.1. Tectonic Setting

[47] The increase in geodetic coverage of the Cascadia margin has led, over the last few years, to an increase in studies of forearc deformation and its relationship to the subduction interseismic loading. Early work was mostly based on locally limited leveling and trilateration-triangulation measurements [e.g., *Reilinger and Adams*, 1982; *Savage et al.*, 1991; *Dragert et al.*, 1994]. In contrast, more recent studies include tens of campaign and permanent GPS sites over the whole Cascadia margin [*McCaffrey et al.*, 2000; *Miller et al.*, 2001; *Svarc et al.*, 2002]. The most recent efforts involve establishing hundreds of campaign sites from Oregon to southern British Columbia [*McCaffrey et al.*, 2002].

[48] Owing to these geodetic studies and to extensive seismicity and tectonic studies [e.g., *Riddihough*, 1984; *Walcott*, 1993; *Wells et al.*, 1998], the main aspects of the present-day Cascadia tectonics and dynamics are well constrained: The subduction thrust is currently fully or close to fully locked, leading to margin-normal shortening and uplift of the forearc [e.g., *Dragert and Hyndman*, 1995; *Miller et al.*, 2001]; The Oregon part of the forearc is migrating northward at 5–10 mm/yr, with little internal permanent deformation [*Wells et al.*, 1998; *McCaffrey et al.*, 2000; *Svarc et al.*, 2002]; Superimposed on the subduction transient signal, the Puget Sound-southern Georgia Strait region of the forearc is affected by permanent north-south shortening [*Khazaradze et al.*, 1999; *Mazzotti et al.*, 2002].

[49] The details of this tectonic picture are still being discussed and improvements in the spatial coverage and the resolution of the GPS data should help address issues such as (1) the distribution of interseismic coupling (extent of locked zone, time variation, coupling ratio), (2) the characteristics and spatial pattern of slow slip events, (3) the distribution of permanent deformation in the northern Cascadia forearc (e.g., rotation vector versus distributed strain), and (4) the relationship of forearc steady N-S deformation to the transient megathrust earthquake cycle.

Table 5. Time Variation of Juan de Fuca/North America Convergence

Model [a]	Rotation Vector			Predicted Velocity (48°N, 234°E)				
	Latitude °N	Longitude °E	ω,[b] deg/Myr	V_n, mm/yr	V_e, mm/yr	V, mm/yr	Azimuth, °N
3 Ma (NUVEL-1A)	22.40	247.19	−0.831	19.5	38.3	42.9	63.0
1.9 Ma (W&D)	29.16	246.25	−0.984	20.3	33.7	39.3	59.0
0.8 Ma (W&D)	32.76	243.68	−1.241	19.5	35.1	40.1	60.9
0.4 Ma (W&D)	35.28	243.63	−1.504	22.8	35.4	42.1	57.2
0.0 Ma (extrapolated)	37.80	243.60	−1.750	25.6	32.9	41.7	52.0

[a]NUVEL-1A [*DeMets et al.*, 1994]; W&D, combination of Juan de Fuca/Pacific [*Wilson*, 1993] and Pacific/North America [*DeMets and Dixon*, 1999].
[b]Rotation rate (positive counterclockwise).

[50] The interpretation for SW British Columbia and NW Washington of our GPS velocity field addresses some of these issues using recent developments on plate convergence and the earthquake cycle. Our starting point is that the deformation observed by GPS in SW British Columbia is mostly controlled by the interseismic loading of the margin. The consequences of small continuous forearc deformation are discussed later in section 3.4. Two models of interseismic coupling are considered; both use the concept of dislocation in an elastic half-space:

[51] Model 1 is a standard 3-D model, where the locked and transition zones are defined on the basis of thermal and geodetic constraints [*Hyndman and Wang*, 1995]. The transition zone has approximately the same width as the locked zone and is defined by a linear downdip decrease of the coupling [*Flück et al.*, 1997].

[52] Model 2 is a more recent 3-D model, where the extent of the transition zone was revisited on the basis of modeled viscoelastic behavior of the subduction system after megathrust earthquakes [*Wang et al.*, 2002]. The transition zone is twice larger than for model 1 and is defined by an exponential downdip decrease of the coupling.

[53] Another source of variations in the modeling and interpretation of the GPS deformation field is the subduction velocity between the Juan de Fuca plate and the Cascadia forearc. There are several models that describe the relative plate motion in the region, involving the Juan de Fuca (JF), Pacific (PA), and North America (NA) plates, and the Oregon forearc sliver. Because we are primarily interested in deformation in northern Cascadia (i.e., north of the Puget Sound deformation zone), the migration of the Oregon forearc is not considered. The global relative plate motion model NUVEL-1A [*DeMets et al.*, 1994] provides a JF/NA rotation vector that is averaged over the last 3 Myr. A recent study combining GPS and geologic evidence concluded that the current PA/NA motion is faster than predicted by NUVEL-1A [*DeMets and Dixon*, 1999]. Additionally, *Wilson* [1993] found a series of significant changes in the JF/PA rotation vector during the last 3 Myr. To test the impact of these variations on the subduction velocity, three JF/NA rotation vectors were derived from *Wilson* [1993] (1.9, 0.8, and 0.4 Ma, Table 5). A hypothetical rotation vector at 0 Ma was extrapolated from the 1.9–0.4 Ma pattern of change.

[54] In spite of the clear northwestward migration of the rotation pole, the associated increase in the rotation rate translates into very small variations of the predicted subduction rate at 48 °N. The subduction direction is affected by a small counterclockwise rotation of ~10° between 3

and 0 Ma (Table 5). The most recent JF/NA rotation vector (0.4 Ma) was used in the standard interseismic model discussed below.

3.2. Interseismic Loading and Horizontal GPS Velocities

[55] The velocity fields predicted by both interseismic loading models (linear and exponential) explain the first order pattern of the GPS horizontal velocities: northeastward motion and landward decreasing rates from 15– 10 mm/yr along the west coast to 3–5 mm/yr inland. The goodness of fit of the models is estimated using a reduced chi square estimator:

$$\chi_N^2 = \left\{ \Sigma_N \Sigma_2 (V_G - V_M)^2 / \sigma_G^2 \right\} / df$$

where V_G and V_M are the GPS and modeled horizontal velocities at each station, σ_G is the uncertainty on the GPS velocity, and *df* is the number of degrees of freedom in the system (i.e., number of observations minus number of unknowns, in this case the length of the transition zone is assumed to be the only unknown). The χ_N^2 is a measure of how well a given model explains the variance in the data set within the uncertainties on the data. Hence $\chi_N^2 \gg 1$ implies a poor fit and/or an underestimation of the data uncertainty.

[56] The χ_N^2 for both models estimated for the continuous and campaign stations are shown in Table 6. Model 2 (exponential decrease) shows a small but systematic ~25% improvement of fit compared to model 1 (linear decrease). The χ_N^2 for the permanent stations is significantly larger than 1, indicating either a poor fit of both models and/or an underestimation of the GPS uncertainties by a factor of ~2.5.

Table 6. The χ_N^2 of Model Misfit

	All[a]	Continuous[b]	Campaign[c]
Model 1 (linear)	3.6	8.2	2.5
Model 2 (expo.)	2.6	6.3	1.8
Model 2b (0 Ma)[d]	2.1	4.8	1.4
Model 3 NE[e]	3.0	10.4	1.3
Model 3 NW[e]	4.7	13.3	2.7

[a]Campaign and permanent stations in northern Cascadia.
[b]Subset of permanent stations including ALBH, CHWK, DRAO, ESQM, NANO, NEAH, NTKA, PGC4, SEDR, SMLD, UCLU, WHD1, WSLR.
[c]Stations from the campaign networks.
[d]Similar to model 2 with 0 Ma rotation vector (Table 5).
[e]Similar to model 2 with imposed Vancouver Island forearc motion (see section 3.4).
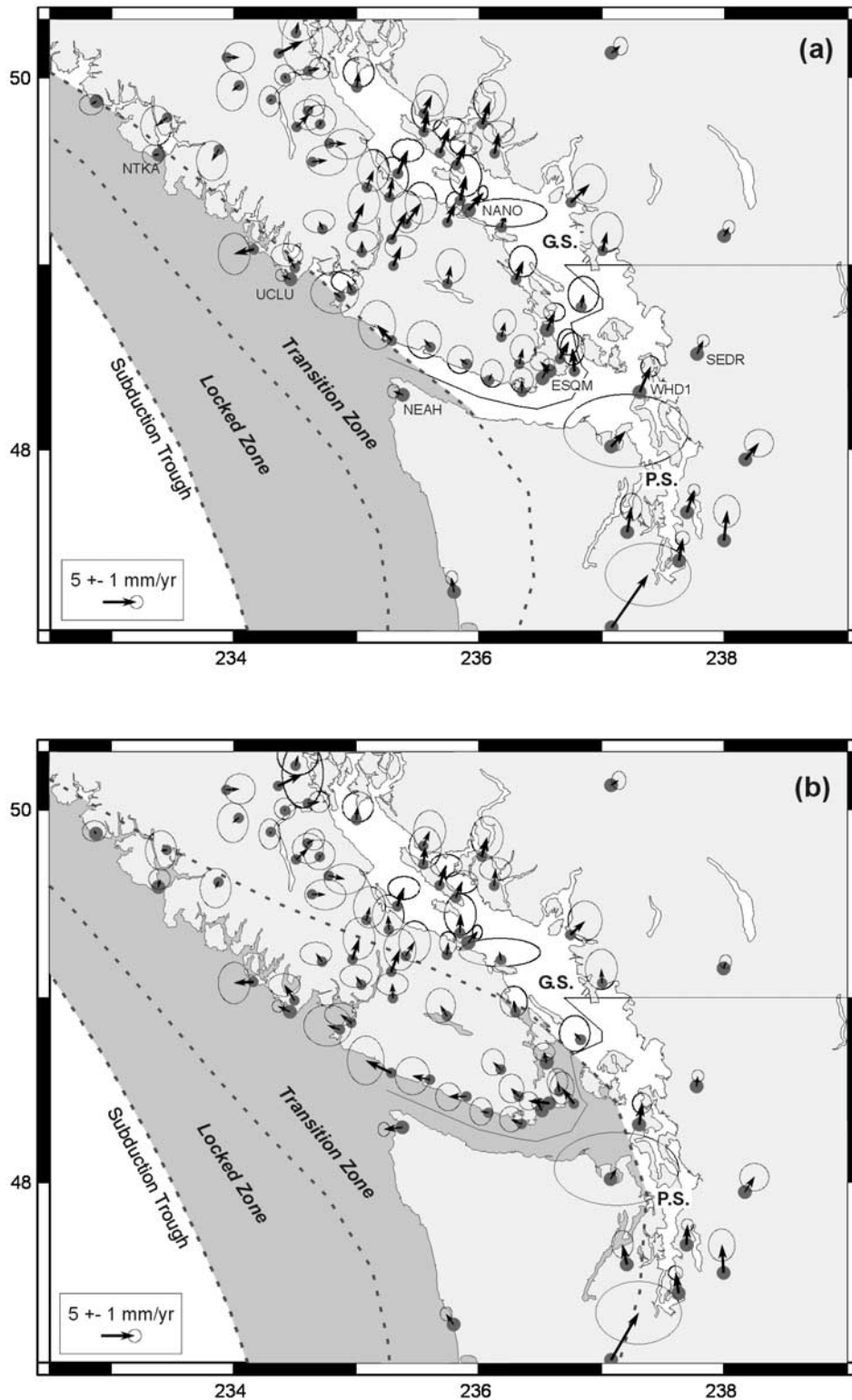
Figure 3. Residual GPS velocities. Solid arrows show residual horizontal velocities (after correction for modeled subduction interseismic deformation) with respect to stable North America in ITRF2000. Error ellipses are at 95% confidence level. Light gray shading indicates locked and transition zones of the subduction thrust. G.S., Georgia Strait; P.S., Puget Sound. (a) Residual velocities for model 1, short linear downdip transition zone; (b) model 2, wide exponential downdip transition zone (see text).
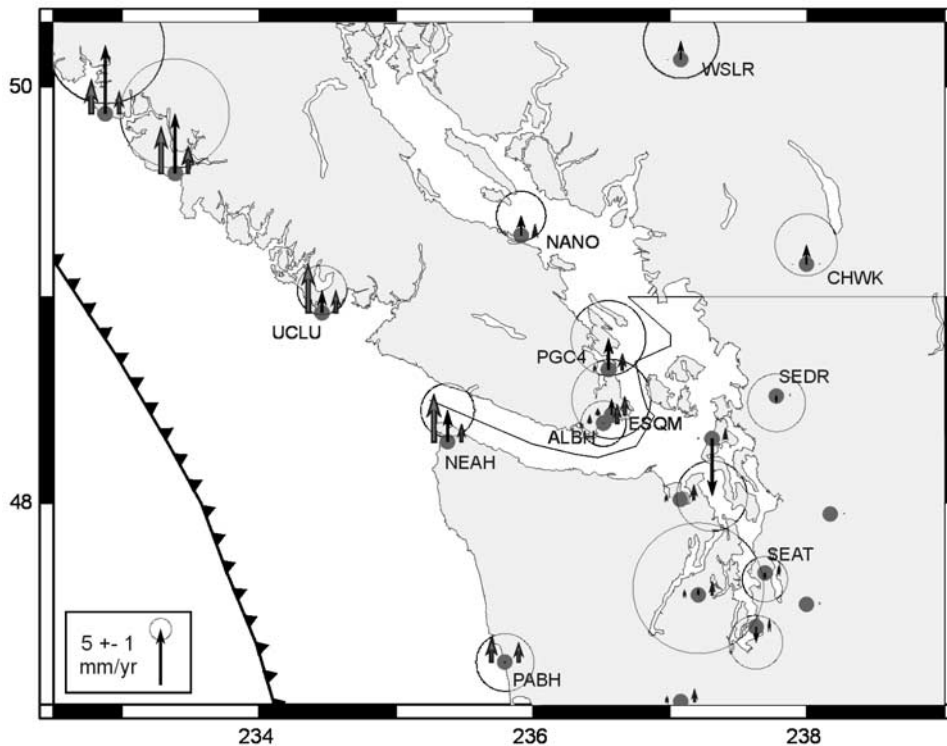
Figure 4. GPS and model vertical velocities. Solid arrows show vertical GPS velocities (north, up; south, down) for permanent stations with respect to stable North America in ITRF2000. Error ellipses are at 95% confidence level. Gray shaded arrows left and right of solid arrows show vertical velocity predicted at GPS site by models 1 and 2, respectively.

[57] The residual velocity vectors (Figure 3) show some locally coherent geographical patterns. For both models, inland sites in southern central Vancouver Island show a consistent northeastward residual velocity of 1–2 mm/yr. This suggests a smaller tapering out of the subduction loading (e.g., wider locked and/or transition zone). For model (2), sites on the west coast of southern Vancouver Island show a northeastward residual velocity of 1–2 mm/yr (Figure 3b), reflecting a ∼10° difference in azimuth between the GPS velocities and the predicted displacements. This residual pattern can be reduced by introducing the 0 Ma JF/NA rotation vector to control the subduction direction and rate (see Table 5). The χ_N^2 for this alternative model 2b shows an improvement of fit of ∼20% compared to model 2 and ∼40% compared to model 1. The change in subduction direction does not significantly affect the fit for the central Vancouver Island stations (sites farther away from locked fault).

[58] Although the fit to the permanent GPS stations was improved by the introduction of the 0 Ma rotation vector, the χ_N^2 is still significantly larger than 1. One implication is that the GPS uncertainties are too small and should be scaled by ∼2.2. Alternatively, a closer look at the residual velocities and the contribution of each station to the total χ_N^2 indicates that, out of the 13 sites, 5 have significantly larger residuals: SEDR and WHD1 (likely affected by permanent margin-parallel deformation), NANO, ESQM (only 2.4 yr of data), and NEAH. Removing these stations from the subset leads to a more reasonable $\chi_N^2 \approx 2.2$.

[59] This analysis of the GPS misfit suggests that the subduction loading model can be slightly improved by a more northward subduction direction (by 5–10°) and by a slower landward decrease of the interseismic loading, especially along the Port Alberni corridor. The reduced strain gradient along the Port Alberni corridor could be due to systematic variations in the rheology of the inner arc or to long-term forearc motion, as discussed in sections 3.3 and 3.4, respectively.

3.3. Vertical Deformation

[60] Because early campaign surveys consisted in a few 5–7 hour-long occupations, we do not consider the vertical results of the campaign networks. The main conclusion from the analysis of the vertical velocity at permanent stations is that most of the rates are not significant at the 95% confidence level (Figure 4 and Table 1). The vertical velocities are small, between −2 and 2 mm/yr for the long time series (3 years or more) and the associated uncertainties are large, 1–1.5 mm/yr at 1σ. Hence the χ_N^2 for the vertical solution is identical ($\chi_N^2 \approx 1.4$) for any model considered, even for a no-subduction model.

[61] Nevertheless, there are significant differences between model 1 and model 2 that can be compared to the GPS vertical pattern. In particular, the GPS velocities suggest that the landward tilting of the forearc is not as large as the subduction loading models predict (Figure 4). Vertical velocities across southern Vancouver Island show an even uplift at ∼2 mm/yr, with a very small tilt (0.3–1.0 mm/yr) between the west coast and the mainland. This regional small to insignificant landward tilt favors model 2, which shows a much smaller tilt than model 1. Combined with the analysis of the horizontal GPS residuals, this vertical pattern

supports the conclusion that the landward decrease of the subduction-loading signal is slower than predicted by model 2, especially for the central Vancouver Island section.

[62] On average GPS vertical velocities in southern Vancouver Island are 1.3 ± 1.5 mm/yr larger than model 2 predictions (Figure 4). This higher uplift rate and the lack of landward tilt discussed previously might be associated with current postglacial rebound (PGR) signal. PGR corrections vary significantly depending on the model used [e.g., *James et al.*, 2000]. The most recent study [*Clague and James*, 2002] suggests that PGR uplift rates for northern Cascadia could range between 0.5 and 0.8 mm/yr, with a small seaward tilt across Vancouver Island of $0.1-0.2$ mm/yr. These PGR corrections could account for part of the discrepancy between our GPS velocities and the interseismic loading model.

[63] It should be noted that these conclusions from the GPS residuals, and their implications on the subduction interseismic loading, are based on second order features of both the GPS data and the subduction model. To a first order the GPS velocities can be well explained by the simple uniform elastic half-space loading models. Although it may be possible to extract important information from the small misfits, rather than trying to force a perfect match between the GPS velocities and the models, the limitations of these simple models and the need for more complex models should be considered. For example, variations in elastic properties of the medium can induce significant perturbations in the predicted deformation field [cf. *Cattin et al.*, 1999]. Recent analysis of releveling data across central Vancouver Island and the adjoining inner coastal margin to the east has identified a broad region of uplift coincident with the Cascade volcanic belt [*Wolynec et al.*, 2003]. It is conceivable that this region of high heat flow [*Lewis et al.*, 1992] has resulted in a weaker crustal zone, which accommodates an anomalous proportion of regional interseismic loading. This can account for the reduced horizontal strain gradient and the more uniform uplift of the coastal margin to the west of the volcanic belt.

3.4. Long-Term Deformation of the Forearc

[64] Our analysis of the northern Cascadia GPS velocities assumed that the forearc is not affected by significant long-term deformation. In this section, we test the hypothesis of a small permanent motion of the forearc and the potential implications for the subduction interseismic coupling. We use two possible models of motion of the Vancouver Island-northernmost Washington (VI) forearc with respect to North America (NA):

[65] 1. The VI/NA motion is $1-5$ mm/yr northeastward. This model would correspond to the hypothesis of a separate Washington block rotating clockwise with respect to North America, at a rate slower than the Oregon block [*McCaffrey et al.*, 2002].

[66] 2. The VI/NA motion is $1-5$ mm/yr northwestward. This is supported by the small consistent residual velocities in southern Vancouver Island, which show a NW motion of $1-2$ mm/yr (Figure 3b), and by evidence for NW-SE horizontal compression in this region [*Mulder*, 1995; *Currie et al.*, 2001].
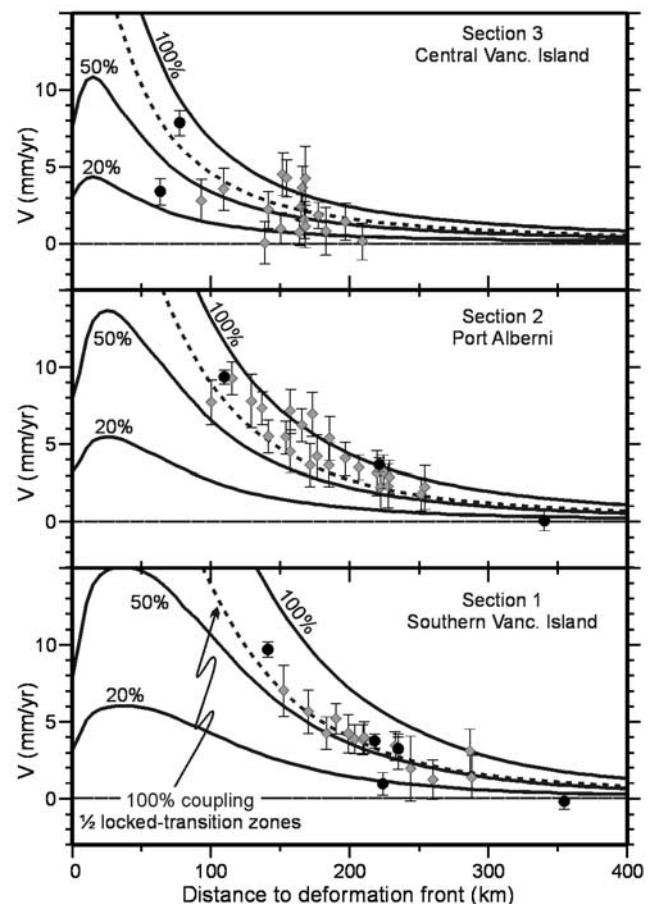

Figure 5. Northeastward moving forearc hypothesis. Margin-normal sections of GPS velocities with respect to southern Vancouver Island-northernmost Washington forearc move 3 mm/yr NE (with respect to North America, see text). Solid circles and shaded squares represent continuous and campaign GPS velocities projected along three N045°E sections. Labeled curves show velocity predicted by subduction-loading model 2 for 100%, 50%, and 20% coupling. Dashed curves show velocity predicted by model 2 for 100% coupling and locked and transition zones reduced to half size.

[67] In both cases, we derive a revised set of GPS velocities (with respect to the VI forearc) that we model using the interseismic loading model 2 (see section 3.2) with a modified subduction velocity accounting for the forearc motion (JF/VI = JF/NA - VI/NA).

[68] Because the plate convergence is almost normal to the subduction trench direction and subparallel to the GPS velocity field, a small northeastward motion of the forearc could easily be mistaken for subduction interseismic loading signal. The impact of a 3 mm/yr NE velocity of the forearc is shown on three margin-normal cross sections (Figure 5). GPS velocities with respect to the forearc decrease from $7-9$ mm/yr along the coast to ~ 0 mm/yr in the Strait of Georgia. Although the convergence rate is reduced by the forearc motion (from 42 mm/yr to 39 mm/yr), these velocities require a low megathrust coupling ($\sim 50\%$, Figure 5). Alternatively, full coupling along significantly smaller
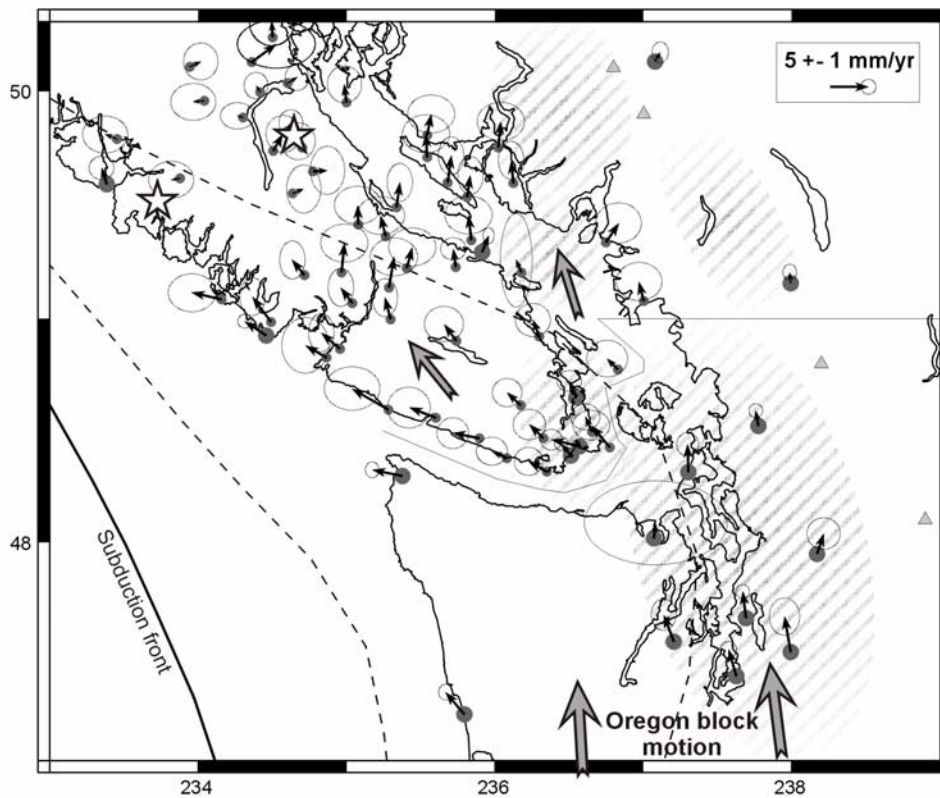
Figure 6. Northwestward moving forearc hypothesis. Residual GPS velocities, with respect to North America, are after correction for interseismic subduction signal but not for imposed 3 mm/yr NW motion of the southern Vancouver Island forearc (see text). Large open stars show $M{\sim}7$ 1918 (east) and 1946 (west) Vancouver Island earthquakes. Zones of active crustal seismicity are highlighted by light gray shading.

locked and transition zones (width reduction of ~50%, Figure 5) can also be used to match the revised GPS data.

[69] For the whole GPS network, the fit of this partial coupling model is similar to that of the original full coupling (see model 3 NE versus model 2, Table 6). However, the permanent stations show a χ_N^2 roughly double compared to the original model. This significant degradation of the model adjustment is mostly associated with the three stations DRAO, NEAH, and UCLU. Without these stations, the adjustment ($\chi_N^2 = 4.2$) becomes similar to that of model 2.

[70] A 3 mm/yr northwestward motion of the forearc with respect to North America implies a clockwise rotation of the JF/VI convergence of ~4°, with very little change of the subduction rate. GPS velocities with respect to the forearc also show a more easterly direction that is matched by the interseismic subduction model in southern Vancouver Island-northernmost Washington. In central Vancouver Island the direction of the model-predicted velocities remain more margin normal because of the smaller inland extent of the locked zone (Figure 6). Along the west coast, the residual GPS velocities (corrected for the transient subduction signal but not for the imposed forearc motion) show a northwestward motion of 2−3 mm/yr, with respect to North America, that rotates to a more northerly direction around the Strait of Georgia (Figure 6).

[71] The χ_N^2 estimates for this northwestward moving forearc model are ~80% larger than those for the standard

model with no forearc motion (see model 3 NW versus model 2, Table 6). As for the NE motion model, the large misfit is essentially due to three permanent stations (DRAO, NANO, and WSLR). Without these three stations, the misfit is only increased by ~20%.

[72] Although these tests of potential forearc motion are crude, they indicate that there may be a small northward (NW to NE) permanent motion of the Vancouver Island-northernmost Washington forearc. The χ_N^2 estimates for the moving forearc models suggest that a roughly similar quality of fit can be obtained for a moving forearc model compared to our original stable forearc approach. However, in both models some of the permanent stations are associated with a large deterioration of the model adjustment. The most significant increase of the misfit are found for five of the most robust permanent station velocities derived from ~6 yearlong time series. This suggest that the potential relative motion of the northern Cascadia forearc is not likely to occur as a simple rigid block motion, as we modeled it, and that instead, additional unmodeled processes or local tectonic complications probably occur.

[73] Two main arguments suggest that, if the Vancouver Island-northern Washington forearc is moving with respect to North America, the motion could not be more than a few millimeters per year:

[74] 1. A larger NE motion would require low interseismic coupling and/or narrow locked and transition zones. Although it is not clearly ruled out, we consider that partial
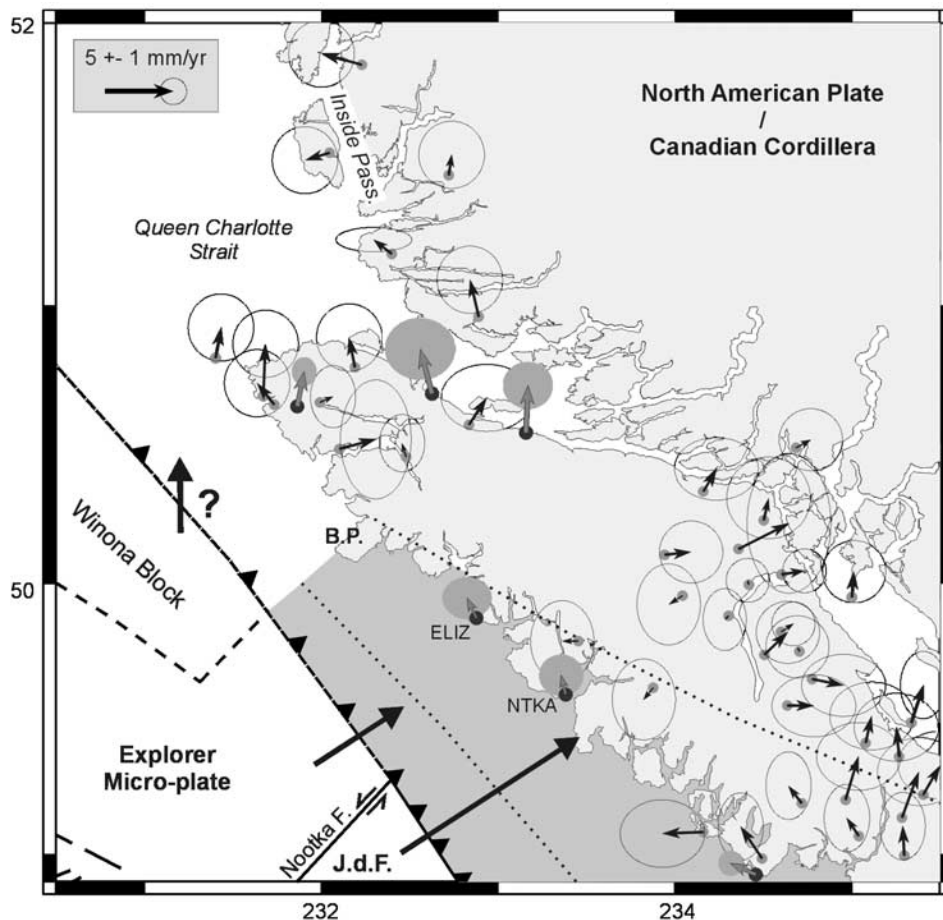
Figure 7. Northern Vancouver Island residual velocities. Thin solid and large gray arrows show horizontal residual velocities (after correction for subduction interseismic transient) at campaign and continuous GPS sites with respect to stable North America. Error ellipses at 95% confidence level. Light gray shading indicates locked and transition zones of the subduction thrust southeast of Brooks Peninsula (B.P.) Dotted lines show the landward limits of the locked and transition zones. Large solid arrows show convergence between North America plate and Juan de Fuca (J.d.F.), Explorer microplate, and hypothetical Winona Block.

coupling is unlikely along the northern Cascadia megathrust. Analysis of geodetic data along many subduction zones generally suggest that strong to nearly full coupling of the seismogenic zone is a fairly common feature [*Mazzotti et al.*, 2000; *Fletcher et al.*, 2001; *Yoshioka et al.*, 2001; *McCaffrey*, 2002]. The downdip extent of the locked and transition zones is well constrained by thermal modeling of the subducting slab [*Hyndman and Wang*, 1995]. The thermal models allow for small variations in the transition isotherm ($\sim 350°C$) of a few tens kilometers, but a reduction of 50% would produce a large mismatch between the model and heat flow data [*Hyndman and Wang*, 1993; *Oleskevich et al.*, 1999].

[75] 2. A roughly northward migration of the northern Cascadia forearc has to be accommodated by permanent deformation at the northeastern end of the moving block (central Vancouver Island, Strait of Georgia, and Coast Mountains). The background seismicity level in this region (rate of M $\geq$ 5 earthquake $\sim 1/35$ year) and the occurrence of two large $M \sim 7$ earthquakes in the last 100 years could be associated with small crustal deformation [cf. *Hyndman and Weichert*, 1983]. By comparison, part of the Oregon

block motion is accommodated in the Puget Sound area (3−4 mm/yr [*Mazzotti et al.*, 2002]), producing significant seismicity (rate of M $\geq$ 7 $\sim 1/400$ year [*Hyndman et al.*, 2003]) and Holocene faulting [e.g., *Atwater and Moore*, 1992; *Johnson et al.*, 1994].

4. Northern Vancouver Island: Subduction-Transform Fault Transition

4.1. Tectonic Setting

[76] The northernmost Cascadia region corresponds to a transition between the subduction of the Juan de Fuca slab to the south and the Pacific-North America transform motion to the north. This transition region is located between two triple junctions that mark the limits of the Explorer (EX) microplate (Figures 1 and 7): The Nootka T-T-F junction between the Cascadia subduction trench, the Explorer underthrusting trough, and the Nootka transform; and the Dellwood T-R-F junction between the Explorer underthrusting trough, the Dellwood-Tuzo Wilson Knolls spreading system, and the Queen Charlotte transform fault.

[77] The current understanding of relative motion between the Explorer microplate and the neighboring plates varies significantly from one boundary to the other. Along the southeastern edge, the JF/EX motion is accommodated along the Nootka Fault [*Hyndman et al.*, 1979]. Seismicity and seafloor reflection profiles indicate a broad zone of shear, rather than a single fault, that accommodates a few cm/yr of left-lateral strike-slip motion [*Hyndman and Weichert*, 1983]. The western edge of the Explorer microplate is bounded by a system of spreading ridges and transform faults that accommodate the EX/PA motion. Earthquake distribution and focal mechanisms correspond to a broad zone of distributed right-lateral shear that cut through the eastern side of the ridge-transform system within the Explorer microplate [*Wahlström and Rogers*, 1992; *Braunmiller and Nábělek*, 2002]. To the northeast, the nature of the present EX/NA relative motion is poorly constrained. There are no clear interplate earthquakes along this boundary. From offshore tectonic data, the Winona block appears to be tectonically and kinematically independent from the Explorer microplate [*Davis and Riddihough*, 1982], whereas earthquake slip vectors suggest the opposite [*Ristau et al.*, 2002; *Braunmiller and Nábělek*, 2002].

[78] Plate reconstruction models suggest that the Explorer microplate separated from the Juan de Fuca plate ∼3.5 Ma [*Riddihough*, 1977]. At this time, the Nootka Fault became active (at about its present location) and the T-R-F triple junction jumped northward from Brooks Peninsula to its present position. The location of the northern edge of the subducted slab follows a NE-SW line (Figure 7) constrained by plate reconstruction models [*Riddihough*, 1977], heat flow data, magnetic, and gravity anomalies [*Lewis et al.*, 1997], and seismic velocity receiver functions [*Cassidy et al.*, 1998].

[79] Two end-member models of the current EX/NA plate tectonics have been proposed:

[80] 1. The Explorer region forms an independent microplate underthrusting underneath northern Vancouver Island at a rate slower than the JF/NA motion off southern Vancouver Island. This option is supported by plate motion models based on magnetic anomalies and earthquake slip vectors [*Riddihough*, 1984; *Riddihough and Hyndman*, 1989; *Ristau et al.*, 2002; *Braunmiller and Nábělek*, 2002].

[81] 2. The Explorer region does not correspond to an independent plate anymore. In this model, the full PA/NA motion is accommodated along the Queen Charlotte Fault, which is propagating southwestward along the Explorer/Pacific boundary to join the northern segment of the Juan de Fuca Ridge [*Bahr and Chase*, 1974; *Rohr and Furlong*, 1995]. No significant motion is accommodated along the former EX/NA boundary. This hypothesis is supported by seafloor morphology [*Rohr and Furlong*, 1995] and current distribution of earthquakes in the eastern Explorer region [e.g., *Kreemer et al.*, 1998].

[82] In the first model, the interaction between the Explorer microplate and the North American plate should produce megathrust transient and/or permanent deformation signal in northern Vancouver Island. In the second model, all plate boundary deformation is accommodated offshore along the former Explorer spreading system, with very little to no elastic or permanent deformation expected in northern Vancouver Island.

4.2. Application to the Current GPS Velocities

[83] The distribution of continuous and campaign GPS sites in northern Vancouver Island is sparser than for the central and southern parts of the island. The measured displacement rates are also smaller, leading to higher uncertainties in the GPS data interpretation. Nevertheless, these data help discriminate between the two end-member models of EX/NA interaction.

[84] The NTKA and ELIZ permanent stations are located on the southern and northern sides of the Nootka Fault zone, respectively. Both stations are moving northeastward, similar to stations to the south, indicating that this motion is most likely related to strain accumulation along the locked subduction thrust (Figure 2). The velocity of NTKA can be accounted for by using the interseismic loading model 2 discussed in sections 3.1 and 3.2, with a JF/NA convergence velocity of 45 mm/yr toward N056° E (as predicted by the 0.4 Ma JF/NA rotation vector). The velocity of ELIZ roughly constrains the convergence rate between the Explorer and North America plates. Using an extension of model 2 north of the Nootka Fault (Figure 7), ELIZ velocity can be accounted for by an EX/NA convergence of about half the JF/NA rate in about the same direction. Because this conclusion relies on one GPS station with only 2 yrs of data, and because it is strongly dependent on the subduction model assumptions (e.g., type of transition zone decay), a more precise assessment of the EX/NA relative motion is not yet possible. However, the velocity pattern of the ELIZ and NTKA stations clearly indicates that the southern part of the Explorer plate is currently subducting underneath northern Vancouver Island (up to Brooks Peninsula), with strain accumulation along the subduction thrust. Assuming a fully locked subduction thrust on both sides of the Nootka Fault, the difference in subduction rate implies a left-lateral strike-slip rate along the Nootka Fault of ∼20 mm/yr, similar to the rates estimated from plate motion models (25–35 mm/yr) [*Riddihough*, 1984; *Hyndman et al.*, 1979] and seismic moment release rate (10–30 mm/yr) [*Hyndman and Weichert*, 1983].

[85] Velocities of the campaign and continuous sites at the northern end of Vancouver Island and around the Queen Charlotte Strait are not significantly affected by the subduction-loading signal from the southern Explorer segment (Nootka Fault to Brooks Peninsula). Although the campaign velocities for the Queen Charlotte Strait network are not as spatially coherent as for the other networks, a systematic pattern of displacement can be observed (Figure 7). Most sites, including the three permanent stations, are moving roughly northward at ∼2–4 mm/yr. This velocity field can be accounted for in two ways:

[86] 1. Assuming there is no current subduction underneath northernmost Vancouver Island, the GPS velocities would represent a nontransient signal indicating a small steady extension (northward motion) of northernmost Vancouver Island with respect to the southern part of the island. This extension is not supported by any earthquake or active fault data, but it could be connected to either the mid Neogene extension phase evidenced by volcanics (as late as Pliocene age [*Lewis et al.*, 1997]), or to the left-lateral

margin shear to the north in the Queen Charlotte Islands region [*Mazzotti et al.*, 2003].

[87] 2. Assuming active subduction underneath northernmost Vancouver Island, an ad hoc model of Winona/NA relative motion can be derived that would explain most of the GPS velocities as transient deformation due to the very oblique underthrusting of the Winona Block along a locked fault. Although this model does not account for the eastern GPS velocities (Queen Charlotte Strait-Inside Passage area), the residuals compared to the model predictions are very small (~2 mm/yr, Figure 7) and insignificant at the 95% level of confidence.

[88] Thus GPS data on northern Vancouver Island show that there is deformation, transient and/or permanent, along this part of the margin, consistent with the existence of an independent Explorer microplate and arguing against the hypothesis of the western Explorer region being attached to North America. This result is consistent with offshore earthquakes slip vectors that require a kinematically independent Explorer plate between Pacific and North America [*Ristau et al.*, 2002; *Braunmiller and Nábělek*, 2002]. However, GPS velocities are inconsistent with the EX/NA relative motion model proposed by *Braunmiller and Nábělek* [2002], which implies a southeastward subduction of the Explorer plate.

5. Conclusions

[89] On the basis of the analysis of 45 permanent GPS stations in the Cascadia Pacific Northwest and 67 campaign GPS measurements in the northern part of Cascadia, we have derived a consistent velocity field with respect to North America for NW Washington-SW British Columbia. There is good agreement between the continuous and campaign data. Horizontal GPS velocities range from 1–2 mm/yr for inland sites to over 10 mm/yr for coastal sites; the horizontal strain is well defined except at the most landward sites. In the vertical component, a pattern of general coastal uplift (~2 mm/yr) can be resolved. We estimate the velocity uncertainties using a model of time series noise spectrum [*Mao et al.*, 1999]. The modeled uncertainties for permanent stations are 0.5–1.0 mm/yr horizontal and 1.5–5 mm/yr vertical, depending mainly on the duration of the time series. For the campaign sites, the modeled uncertainties are ~1.5 mm/yr horizontal. Uncertainties for the vertical component are currently too large to be useful.

[90] The combined permanent campaign GPS velocities provide the basis for interpretation of the tectonics and kinematics of the northern Cascadia subduction system. The first order component of these velocities results from the interseismic loading of the Cascadia megathrust, and confirms that the upper part of the megathrust is fully, or nearly fully locked. An exponential transition zone downdip of the locked zone gives slightly better agreement with the data compared to the commonly used linear transition to free slip. However, the observed horizontal GPS velocities fall off landward more slowly than either model. This disagreement could be a consequence of a small (0–3 mm/yr) roughly northward long-term motion of the southern Vancouver Island forearc with respect to North America. Alternatively, it could be related to the existence of a weak crustal zone coincident with the volcanic belt,

which may perturb the distribution of strain across the coastal margin.

[91] The goodness of fit of the tectonic models with the GPS velocities is estimated using a reduced χ^2 estimator. The best fit model (no forearc motion and exponential transition zone) shows a χ^2 improvement of about 25–50% compared to the alternative models. For the permanent station, the reduced χ^2 is relatively high (~4–13). This could indicate that the modeled uncertainties for the permanent station velocities are underestimated by a factor of 2–3. However, for all models the high χ^2 is due to large residuals at 2–4 stations, which vary from one model to another. Thus we suggest that the relatively large χ^2 mostly reflects the limitation of our simple elastic loading-rigid forearc models. The significant residuals at robust permanent station may indicate that the northern Cascadia forearc does not behave as a rigid elastic block and that local tectonic complications occur.

[92] In northern Vancouver Island, our GPS velocity field is consistent with the existence of an independent Explorer microplate currently underthrusting beneath North America, at least up to Brooks Peninsula. Further to the north, GPS velocities gradually rotate from nearly orthogonal to the margin toward the direction of the Pacific-North America relative motion. The vectors are consistent with an independent oblique underthrusting Winona Block, but also may be explained by permanent deformation within northern Vancouver Island, at the transition between the major subduction and transform systems.

References

Altamimi, Z., P. Sillard, and C. Boucher, ITRF2000: A new release of the International Terrestrial Reference Frame for earth science applications, *J. Geophys. Res.*, *107*(B10), 2214, doi:10.1029/2001JB000561, 2002.

Atwater, B. F., and A. L. Moore, A tsunami about 100 years ago in Puget Sound, Washington, *Science*, *258*, 1614–1617, 1992.

Bahr, S. M., and R. L. Chase, Geology of the northern end of the Juan de Fuca Ridge and sea-floor spreading, *Can. J. Earth Sci.*, *11*, 1384–1406, 1974.

Braunmiller, J., and J. Nábělek, Seismotectonics of the Explorer region, *J. Geophys. Res.*, *107*(B10), 2208, doi:10.1029/2001JB000220, 2002.

Carbotte, S. M., J. M. Dixon, E. Farrar, E. E. Davis, and R. P. Riddihough, Geological and geophysical characteristics of the Tuzo Wilson seamounts: Implications for the plate geometry in the vicinity of the Pacific-North America-Explorer triple junction, *Can. J. Earth Sci.*, *26*, 2365–2384, 1989.

Cassidy, J. F., R. M. Ellis, C. Karavas, and G. C. Rogers, The northern limit of the subducted Juan de Fuca plate system, *J. Geophys. Res.*, *103*, 26,949–26,961, 1998.

Cattin, R., P. Briolle, H. Lyon-Caen, P. Bernard, and P. Pinettes, Effect of superficial layers on coseismic displacement for a dip-slip fault and geophysical implications, *Geophys. J. Int.*, *137*, 149–158, 1999.

Clague, J. J., and T. S. James, History and isostatic effects of the last ice sheet in southern British Columbia, *Quat. Sci. Rev.*, *21*, 71–87, 2002.

Currie, C. A., J. F. Cassidy, and R. D. Hyndman, A regional study of shear wave splitting above the Cascadia subduction zone: Margin-parallel crustal stress, *Geophys. Res. Lett.*, *28*, 659–662, 2001.

Davis, E. E., and R. P. Riddihough, The Winona Basin: Structure and tectonics, *Can. J. Earth Sci.*, *19*, 767–788, 1982.

DeMets, C., and T. H. Dixon, New kinematic models for the Pacific-North America motion from 3 Ma to present: I. Evidence for steady motion and biases in the NUVEL-1A model, *Geophys. Res. Lett.*, *26*, 1921–1924, 1999.

DeMets, C., R. G. Gordon, D. F. Argus, and S. Stein, Effects of recent revisions to the geomagnetic reversal time scale on estimates of current plate motions, *Geophys. Res. Lett.*, *21*, 2191–2194, 1994.

Dixon, T. H., M. M. Miller, F. Farina, H. Wang, and D. Johnson, Present-day motion of the Sierra Nevada block and some tectonic implications for the Basin and Range province: North American Cordillera, *Tectonics*, *19*, 1–24, 2000.

Dragert, H., and R. D. Hyndman, Continuous GPS monitoring of elastic strain in the northern Cascadia subduction zone, *Geophys. Res. Lett.*, *22*, 755–758, 1995.

Dragert, H., R. D. Hyndman, G. C. Rogers, and K. Wang, Current deformation and the width of the seismogenic zone of the northern Cascadia subduction thrust, *J. Geophys. Res.*, *99*, 653–668, 1994.

Dragert, H., X. Chen, and J. Kouba, GPS monitoring of crustal strain in southwest British Columbia with the Western Canada Deformation Array, *Geomatica*, *49*, 301–313, 1995.

Dragert, H., K. Wang, and T. S. James, A silent slip event on the deeper Cascadia subduction interface, *Science*, *292*, 1525–1528, 2001.

Dragert, H., S. Mazzotti, and K. Wang, Aseismic slip on the Northern Cascadia subduction zone: Impacts on seismic hazard estimates, *Eos Trans. AGU*, *83*(47), Fall Meet. Suppl., Abstract S21C-01, 2002.

Fletcher, H. J., J. Beavan, J. T. Freymueller, and L. Gilbert, High interseismic coupling of the Alaska subduction zone SW of the Kodiak Island inferred from GPS data, *Geophys. Res. Lett.*, *28*, 443–446, 2001.

Flück, P., R. D. Hyndman, and K. Wang, Three-dimensional dislocation model for great earthquakes of the Cascadia subduction zone, *J. Geophys. Res.*, *102*, 20,539–20,550, 1997.

Henton, J. A., GPS studies of crustal deformation in the northern Cascadia subduction zone, Ph.D. thesis, 169 pp., Univ. of Victoria, Victoria, B. C., Canada, 2000.

Henton, J. A., H. Dragert, R. D. Hyndman, and K. Wang, Geodetic monitoring of crustal deformation and strain on Vancouver Island, *Eos Trans. AGU*, *80*(46), Fall Meet. Suppl., Abstract G52A-09, 1999.

Henton, J. A., H. Dragert, R. McCaffrey, K. Wang, and R. D. Hyndman, North Cascadia margin deformation from GPS measurements, *Eos Trans. AGU*, *81*(48), Fall Meet. Suppl., Abstract G11A-14, 2000.

Hugentobler, U., S. Schaer, and P. Fridez (Eds.), Documentation of the Bernese GPS software version 4. 2, 511 pp., Astron. Inst., Univ. of Berne, Berne, 2001.

Hyndman, R. D., and K. Wang, The rupture zone of Cascadia great earthquakes from current deformation and thermal regime, *J. Geophys. Res.*, *100*, 22,133–22,154, 1995.

Hyndman, R. D., and D. H. Weichert, Seismicity and rates of relative motion on the plate boundaries of western North America, *Geophys. J. R. Astron. Soc.*, *72*, 59–82, 1983.

Hyndman, R. D., R. P. Riddihough, and R. Herzer, The Nootka Fault zone—A new plate boundary off western Canada, *Geophys. J. R. Astron. Soc.*, *58*, 667–683, 1979.

Hyndman, R. D., S. Mazzotti, D. Weichert, and G. C. Rogers, Large earthquake rate of occurrence in Puget Sound-S. Georgia Strait predicted from geodetic and geological deformation rates, *J. Geophys.*, *108*, 2033, doi:10.1029/2001JB001710, 2003.

James, T. S., J. J. Clague, K. Wang, and I. Hutchinson, Postglacial rebound at the northern Cascadia subduction zone, *Quat. Sci. Rev.*, *19*, 1527–1541, 2000.

Johnson, S. Y., C. J. Potter, and J. M. Armentrout, Origin and evolution of the Seattle fault and Seattle basin, *Geology*, *22*, 71–74, 1994.

Khazaradze, G., A. Qamar, and H. Dragert, Tectonic deformation in western Washington from continuous GPS measurements, *Geophys. Res. Lett.*, *26*, 3153–3158, 1999.

Kleusberg, A., Y. Georgiadou, and H. Dragert, Establishment of crustal deformation networks using GPS: A case study, *CISM J. ACSGC*, *42*, 341–351, 1988.

Kreemer, C., R. Govers, K. P. Furlong, and W. E. Holt, Plate boundary deformation between the Pacific and North America in the Explorer region, *Tectonophysics*, *293*, 225–238, 1998.

Langbein, J., and H. Johnson, Correlated errors in geodetic time series: Implications for time-dependant deformation, *J. Geophys. Res.*, *102*, 591–604, 1997.

Le Provost, C., F. H. Lyard, J. M. Molines, M. L. Genco, and F. Rabilloud, A hydrodynamic ocean tide model improved by assim-ilating a satellite altimeter-derived data set, *J. Geophys. Res.*, *100*, 5513–5529, 1998.

Lewis, T. J., W. H. Bentowski, and R. D. Hyndman, Crustal temperature near the Lithoprobe southern Canadian Cordillera transect, *Can. J. Earth Sci.*, *29*, 1197–1214, 1992.

Lewis, T. J., C. Lowe, and T. S. Hamilton, Continental signature of a ridge-trench-triple junction: Northern Vancouver Island, *J. Geophys. Res.*, *102*, 7767–7781, 1997.

Mao, A., C. G. A. Harrison, and T. H. Dixon, Noise in GPS coordinate time series, *J. Geophys. Res.*, *104*, 2797–2816, 1999.

Mazzotti, S., X. Le Pichon, P. Henry, and S. Miyazaki, Full interseismic locking of the Nankai and Japan-west Kuril subduction zones: An analysis of uniform elastic strain accumulation in Japan constrained by permanent GPS, *J. Geophys. Res.*, *105*, 13,159–13,177, 2000.

Mazzotti, S., H. Dragert, R. D. Hyndman, M. M. Miller, and J. A. Henton, GPS deformation in a region of high crustal seismicity: N. Cascadia forearc, *Earth Planet. Sci. Lett.*, *198*, 41–48, 2002.

Mazzotti, S., R. D. Hyndman, P. Flück, A. J. Smith, and M. Schmidt, Distribution of the Pacific/North America motion in the Queen Charlotte Islands-S. Alaska plate boundary zone, *Geophys. Res. Lett.*, *30*(14), 1762, doi:10.1029/2003GL017586, 2003.

McCaffrey, R., Crustal block rotation and plate coupling, in *Plate Boundary Zone*, *Geodyn. Ser.*, vol. 30, edited by S. Stein and J. T. Freymueller, pp. 101–122, AGU, Washington, D. C., 2002.

McCaffrey, R., C. K. Johnson, P. C. Zwick, M. D. Long, C. Godfinger, J. L. Nabeleck, and C. Smith, Rotation and plate locking along the southern Cascadia subduction zone, *Geophys. Res. Lett.*, *27*, 3117–3120, 2000.

McCaffrey, R., A. Qamar, C. Williams, Z. Ning, P. Wallenberger, and R. W. King, Geodetic constraints on fault coupling on the Cascadia subduction zone, *Eos Trans. AGU*, *83*(47), Fall Meet. Suppl., Abstract S21C-06, 2002.

Miller, M. M., D. J. Johnson, C. M. Rubins, H. Dragert, K. Wang, A. Qamar, and C. Goldfinger, GPS-determination of along-strike variation in Cascadia margin kinematics: Implication for relative plate motion, subduction zone coupling, and permanent deformation, *Tectonics*, *20*, 161–176, 2001.

Miyazaki, S., and K. Heki, Crustal velocity field of southwest Japan: Subduction and arc-arc collision, *J. Geophys. Res.*, *106*, 4305–4326, 2001.

Mulder, T., Small earthquakes in southwestern British Columbia (1975–1991), M.Sc. thesis, 117 pp., Univ. of Victoria, Victoria, B. C., Canada, 1995.

Niell, A. E., Global mapping functions for the atmosphere delay at radio wavelengths, *J. Geophys. Res.*, *101*, 3227–3246, 1996.

Oleskevich, D. A., R. D. Hyndman, and K. Wang, The updip and downdip limits to great subduction earthquakes; thermal and structural models of Cascadia, south Alaska, SW Japan, and Chile, *J. Geophys. Res.*, *104*, 14,965–14,991, 1999.

Pagiatakis, S. D., Program LOADSDP for the calculation of ocean load effect, *Manusc. Geod.*, *17*, 315–320, 1992.

Reilinger, R., and J. Adams, Geodetic evidence for active landward tilting of the Oregon and Washington coastal ranges, *Geophys. Res. Lett.*, *9*, 401–403, 1982.

Riddihough, R. P., A model of recent plate interactions off Canada's west coast, *Can. J. Earth Sci.*, *14*, 384–396, 1977.

Riddihough, R. P., Recent movements of the Juan de Fuca plate system, *J. Geophys. Res.*, *89*, 6980–6994, 1984.

Riddihough, R. P., and R. D. Hyndman, Queen Charlotte Islands margin, in *The Geology of North America*, vol. N, *The Eastern Pacific Ocean and Hawaii*, edited by E. L. Winterer et al., pp. 403–411, Geol. Soc. of Am., Boulder, Colo., 1989.

Ristau, J., G. Rogers, and J. Cassidy, Slip direction and moment magnitude for earthquakes off Canada's west coast, *Eos Trans. AGU*, *83*(47), Fall Meet. Suppl., Abstract S71C-1113, 2002.

Rogers, G. C., and H. S. Hasegawa, A second look at the British Columbia earthquake of June 23, 1946, *Bull. Seismol. Soc. Am.*, *68*, 653–675, 1978.

Rohr, K. M. M., and K. P. Furlong, Ephemeral plate tectonics at the Queen Charlotte triple junction, *Geology*, *23*, 1035–1038, 1995.

Savage, J. C., and M. Lisowski, Strain measurements and potential for a great subduction earthquake off the coast of Washington, *Science*, *252*, 101–103, 1991.

Savage, J. C., M. Lisowski, and W. H. Prescott, Strain accumulation in western Washington, *J. Geophys. Res.*, *96*, 14,493–14,507, 1991.

Sella, G. F., T. H. Dixon, and A. Mao, REVEL: A model for Recent plate velocities from space geodesy, *J. Geophys. Res.*, *107*(B4), 2081, doi:10.1029/2000JB000033, 2002.

Svarc, J. L., J. C. Savage, W. H. Prescott, and M. H. Murray, Strain accumulation and rotation in western Oregon and southwestern Washington, *J. Geophys. Res.*, *107*(B5), 2087, doi:10.1029/2001JB000625, 2002.

Wahlström, R., and G. C. Rogers, Relocation of earthquakes west of Vancouver Island, British Columbia, 1965–1983, *Can. J. Earth Sci.*, *29*, 953–961, 1992.

Walcott, D., Neogene tectonics and kinematics of western North America, *Tectonics*, *12*, 326–333, 1993.

Wang, K., R. Wells, S. Mazzotti, R. D. Hyndman, and T. Sagiya, A revised dislocation model of interseismic deformation of the Cascadia subduction zone, *J. Geophys. Res.*, *108*(B1), 2026, doi:10.1029/2001JB001227, 2003.

Wells, R. E., C. S. Weaver, and R. J. Blakely, Forearc migration in Cascadia and its neotectonic significance, *Geology*, *26*, 759–762, 1998.

Wessel, P., and W. H. F. Smith, New version of the Generic Mapping Tools released, *Eos Trans. AGU*, *76*, 329, 1995.

Wilson, D. S., Confidence intervals for motion and deformation of the Juan de Fuca plate, *J. Geophys. Res.*, *98*, 16,053–16,071, 1993.

Wolynec, L., H. Dragert, A. Lambert, M. Schmidt, and A. Mainville, Improving model constraints for vertical deformation across the northern Cascadia margin, paper presented at Annual CGU Meeting, Can. Geophys. Union, Banff, Alberta, 2003.

Yoshioka, S., K. Wang, and S. Mazzotti, Locking state of the northern Cascadia megathrust fault inferred from inversion of GPS velocities, *Eos Trans. AGU*, *82*(47), Fall Meet. Suppl., Abstract G41A-0189, 2001.

Zhang, J., Y. Bock, H. Johnson, P. Fang, S. Williams, J. Genrich, S. Wdowinski, and J. Behr, southern California permanent GPS geodetic array: Error analysis of daily position estimates and site velocities, *J. Geophys. Res.*, *102*, 18,035–18,055, 1997.

————————————

M. Craymer and J. Henton, Gravity and Geodetic Networks Section, Geodetic Survey Division, 615 Booth Street, Ottawa, Ontario, Canada K1A 0E9. (mcraymer@nrcan.gc.ca; jhenton@nrcan.gc.ca)

H. Dragert, R. Hyndman, T. James, Y. Lu, S. Mazzotti, and M. Schmidt, Pacific Geoscience Centre, Geological Survey of Canada, 9860 West Saanich Road, Sidney, British Columbia, Canada V8L 4B2. (dragert@pgc.nrcan.gc.ca; rhyndman@nrcan.gc.ca; james@pgc.nrcan.gc.ca; lu@pgc.nrcan.gc.ca; smazzotti@nrcan.gc.ca; mschmidt@nrcan.gc.ca)

From McCaffrey et al., Plate coupling, block rotations and crustal deformation in the Pacific Northwest, submitted *to Geophys. J. Int*., June, 2006.

[Data are survey mode and continuous from ~350 sites, 1991-2004.]

To obtain the site velocities from the field data, we follow the procedure described by McClusky *et al*. (2000). First we use the GAMIT software (King & Bock 2002) to combine the phase observations from the field receivers deployed each day with observations from 5-10 continuous stations to estimate site positions together with atmospheric, orbital, and Earth orientation parameters. We then use the GLOBK software (Herring 2002) to combine these estimates (and their covariance matrices) with estimates obtained from a similar analysis at the Scripps Orbit and Permanent Array Center (SOPAC) (Bock *et al*. 1997) of observations from up to 400 continuous GPS stations, including all PANGA sites available at the time. In a third step, we aggregate the daily estimates over periods of 10-30 days to reduce the computational burden and to assess better the long-term statistics of the observations. Finally, we combine the ~monthly averaged estimates and their full covariance matrices to estimate a long term average velocity. The velocity solution includes all sites for which the semi-major axis of the 95% confidence ellipse is less than 5 mm/yr, corresponding to a one-sigma east or north uncertainty of about 2 mm/yr.

The errors in site positions and velocities estimated from GPS observations are a combination of random ("white") and correlated ("red") noise that depends on the satellite and tracking network (both weaker in earlier years); the instrumentation and signal-scattering environment at each site; atmospheric conditions, monument stability, and deficiencies in our models for the orbital motions of the satellites, and for site motions due to Earth and ocean tides, and atmospheric and hydrological loading. With the long time series available for continuous observations, it is possible to reduce the random noise to a negligible level and to evaluate the character of the correlated noise (e.g., Williams *et al*. 2004). For the survey-mode measurements in the PNW, random noise usually dominates. To account for site-dependent noise apparent in the raw (phase) observations, GAMIT estimates an elevation-dependent noise model for each observing session. To account for longer-term errors, we examined the time series of both the daily and ~monthly site positions, removing outliers and re-weighting the data when high scatter or systematic trends were apparent. In particular, to avoid overweighting the data from permanent stations or field receivers operated every day during a survey, we added quadratically 1.5 mm to the uncertainties of the ~monthly position estimates for all sites. To account for monument instability and other errors with correlation times of months to years, we included 0.5 $mm/yr^{1/2}$ of random walk noise for all sites, and 2-3 $mm/yr^{1/2}$ for 17 (mostly continuous) sites for which the times series exhibited significant systematic signatures. Figure 3 shows histograms of the weighted rms (wrms) and normalized rms (nrms) for all times series with five or more observations. For both the north and east components, 70% of the wrms scatters are less than 2 mm. The nrms histograms are approximately normal but with a mean at 0.6. Although the error model used for the time series does not include the random-walk component (we added this only in the velocity solution), a value less than 1.0 is still a reasonable target since we expect the scatter in the time series to underestimate the true uncertainties in the velocity estimates, which will have a significant contribution from correlated errors.

The best test of our noise model is the distribution of the errors in the velocities themselves. To assess these we examine the velocities for 94 stations in the slowly deforming region of central and eastern Oregon, Washington, and British Columbia after removing a simple model (Fig. 4a). We computed the magnitude and its uncertainty for each velocity and compared a cumulative histogram of the ratio of these values with that expected from a (2-d) chi-square distribution assuming that the north and east residuals are normally distributed with unit variance (Fig. 4b). The histogram shows that our assumed noise model matches the expected distribution of normalized residuals reasonably well: the excess of values to the left of the curve between 50% and 85% indicates indicates that some of the uncertainties are too large; the deficiency above the 95% level reflects the removal of too many outliers. The north component of the residual velocities has an nrms of 1.01, and the east 0.91. For most of the test region, the residuals are randomly distributed, but there are systematic, mostly north-south residuals discernible at the level of 0.5-1.0 mm/yr for groups of stations in the NW, NE, and SE parts of the region (Fig. 4a). The histogram, component nrms values, and the visible contribution of a N-S model error all suggest that our error model is slightly pessimistic.
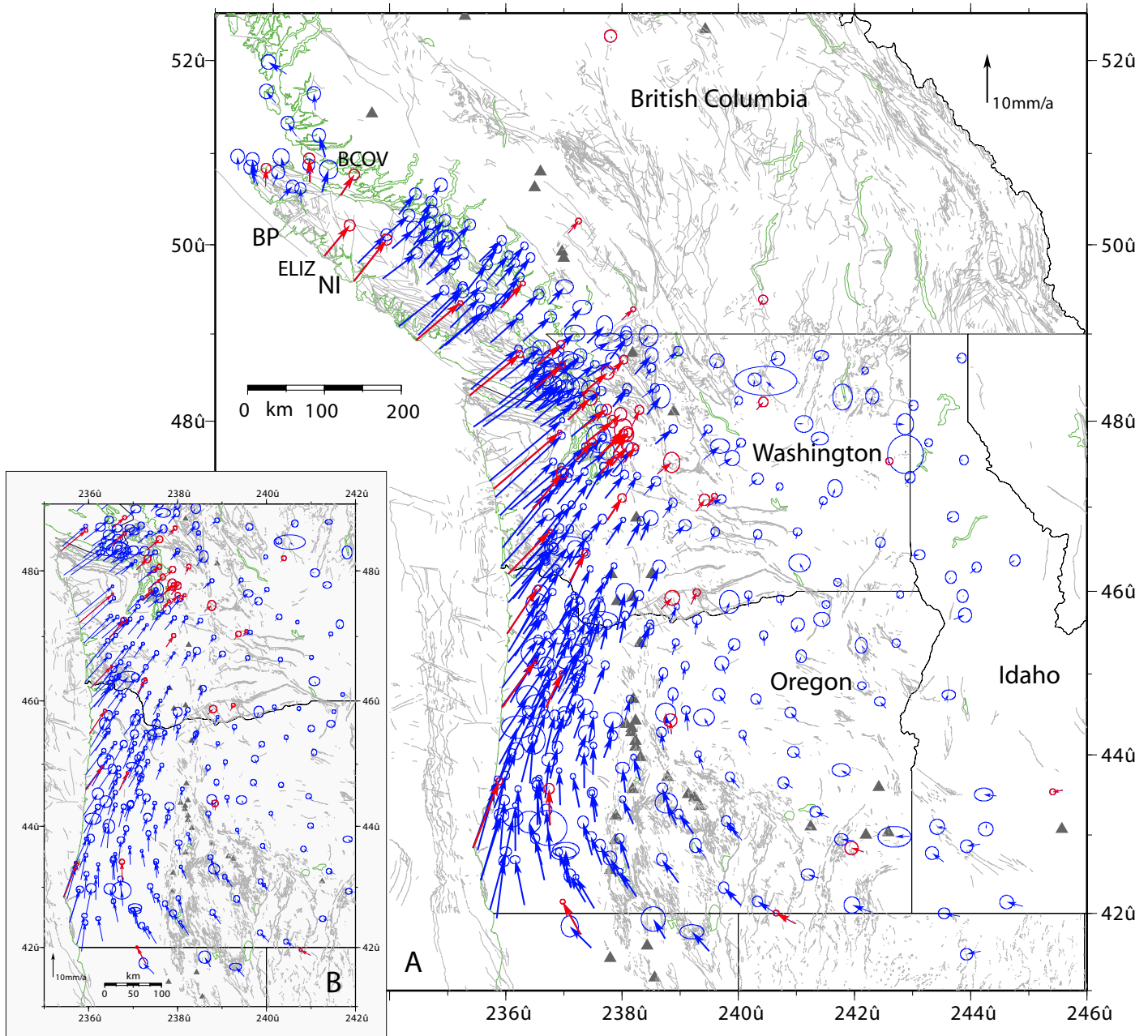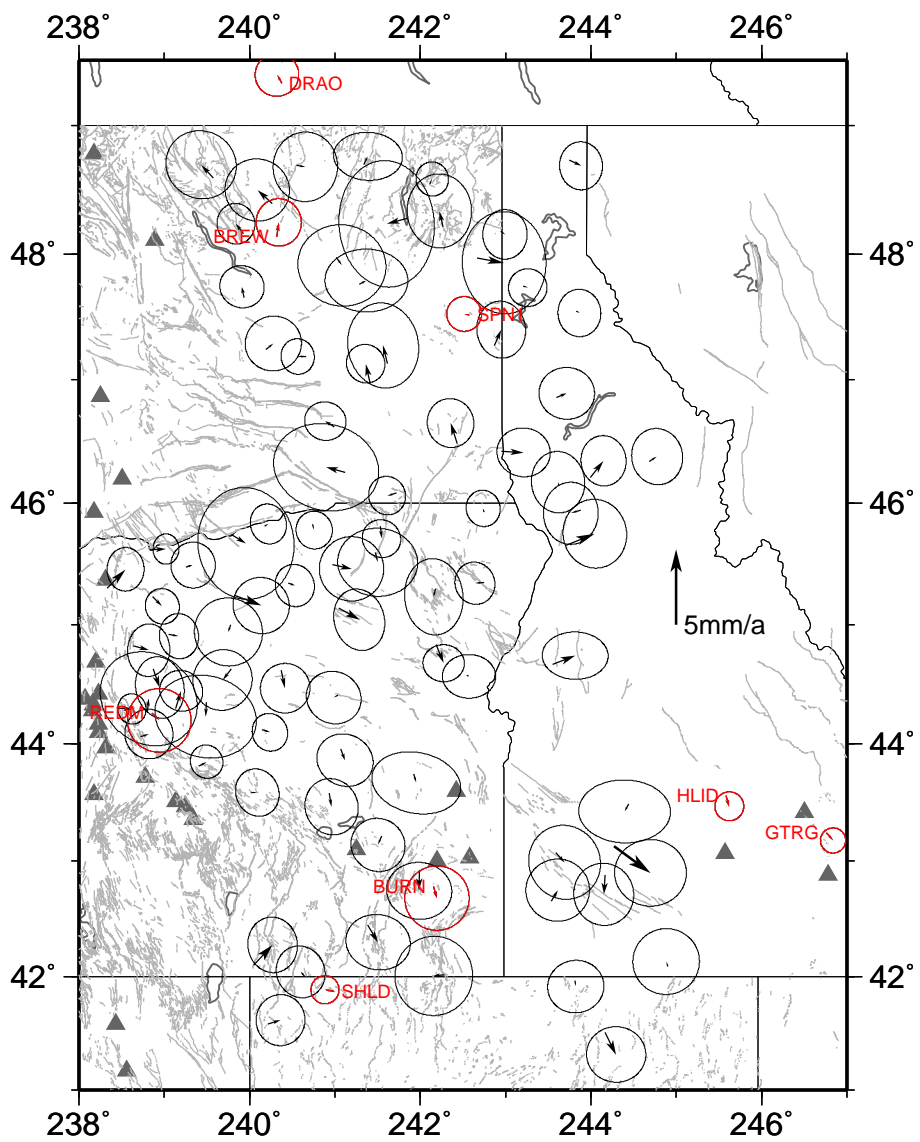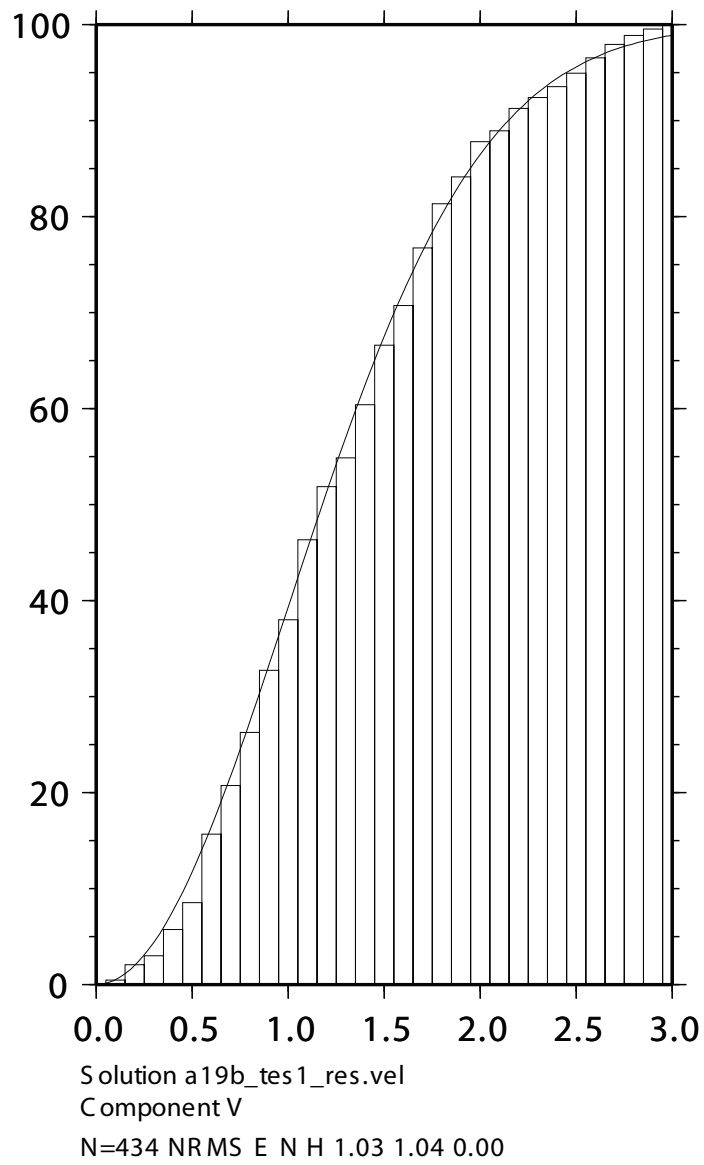
Fig. 2

Solution a19b_tes1_res.vel
Component V

N=434 NRMS E N H 1.03 1.04 0.00

Fig 3